

WL-TR-97-2003

**HIGH TEMPERATURE LUBRICATION OF  
ROLLING CONTACTS WITH LUBRICANTS  
DELIVERED FROM THE VAPOR PHASE  
AND AS OIL-MISTS**

Nelson H. Forster  
Lubrication Branch  
Fuels and Lubrication Division



January 1997

Final Report for January 1994 - December 1996

APPROVED FOR PUBLIC RELEASE; DISTRIBUTION IS UNLIMITED

AERO PROPULSION AND POWER DIRECTORATE  
WRIGHT LABORATORY  
AIR FORCE Materiel COMMAND  
WRIGHT-PATTERSON AIR FORCE BASE OH 45433-7251

19970625 043

DTIC QUALITY INSPECTED 3

## NOTICE

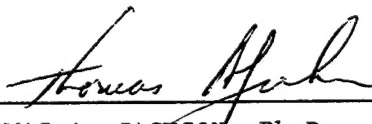
When government drawings, specifications, or other data are used for any purpose other than in connection with a definitely government-related procurement, the United States Government incurs no responsibility or any obligation whatsoever. The fact that the government may have formulated or in any way supplied the said drawings, specifications, or other data is not to be regarded by implication, or otherwise in any manner construed, as licensing the holder or any other person or corporation, or as conveying any rights or permission to manufacture, use, or sell any patented invention that may in any way be related thereto.

This report has been reviewed by the Office of Public Affairs (ASD/PA) and is releasable to the National Technical Information Service (NTIS). At NTIS, it will be available to the general public, including foreign nations.

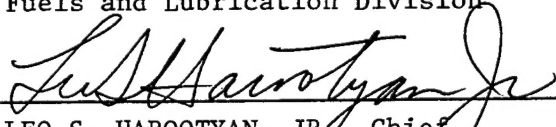
This technical report has been reviewed and is approved for publication.



NELSON H. FORSTER, Ph.D.  
Project Engineer  
Lubrication Branch  
Fuels and Lubrication Division



THOMAS A. JACKSON, Ph.D.  
Chief  
Lubrication Branch  
Fuels and Lubrication Division



LEO S. HAROOTYAN, JR., Chief  
Fuels and Lubrication Division  
Aero Propulsion and Power Directorate

If your address has changed, if you wish to be removed from our mailing list, or if the addressee is no longer employed by your organization, please notify WL/POSL, Wright-Patterson AFB OH 45433-7103 to help us maintain a current mailing list.

Copies of this report should not be returned unless return is required by security considerations, contractual obligations, or notice on a specific document.

REPORT DOCUMENTATION PAGE			Form Approved OMB No. 0704-0188	
Public reporting burden for this collection of information is estimated to average 1 hour per response, including the time for reviewing instructions, searching existing data sources, gathering and maintaining the data needed, and completing and reviewing the collection of information. Send comments regarding this burden estimate or any other aspect of this collection of information, including suggestions for reducing this burden, to Washington Headquarters Services, Directorate for Information Operations and Reports, 1215 Jefferson Davis Highway, Suite 1204, Arlington, VA 22202-4302, and to the Office of Management and Budget, Paperwork Reduction Project (0704-0188), Washington, DC 20503.				
1. AGENCY USE ONLY (Leave blank)		2. REPORT DATE January 1997		3. REPORT TYPE AND DATES COVERED Final, January 1994 - December 1996
4. TITLE AND SUBTITLE High Temperature Lubrication of Rolling Contacts with Lubricants Delivered from the Vapor Phase and as Oil-Mists			5. FUNDING NUMBERS PE: 62203F, 61102F PROJ: 3048, 2308 TASK: 06, BW WU: 19, 80	
6. AUTHOR(S)  Nelson H. Forster, Ph.D, 937-255-4347				
7. PERFORMING ORGANIZATION NAME(S) AND ADDRESS(ES) Aero Propulsion and Power Directorate Wright Laboratory Air Force Materiel Command Wright-Patterson AFB OH 45433-7251			8. PERFORMING ORGANIZATION REPORT NUMBER  WL-TR-97-2003	
9. SPONSORING/MONITORING AGENCY NAME(S) AND ADDRESS(ES) Aero Propulsion and Power Directorate Wright Laboratory Air Force Materiel Command Wright-Patterson AFB OH 45433-7251 POC: Nelson H. Forster, 937-255-4347			10. SPONSORING/MONITORING AGENCY REPORT NUMBER  WL-TR-97-2003	
11. SUPPLEMENTARY NOTES				
12a. DISTRIBUTION AVAILABILITY STATEMENT  Approved for Public Release; Distribution is Unlimited			12b. DISTRIBUTION CODE	
13. ABSTRACT (Maximum 200 words) Several classes of synthetic lubricants were investigated as vapor phase lubricants, using a ball-on-rod tester. In general, lubricants containing phosphorus demonstrated the best high temperature performance with sustained operation at temperatures above 600° C in an air environment. After testing, bearing surfaces were analyzed using FTIR, Raman spectroscopy, SEM, EDS, and AES. Condensed phosphates and graphite were identified on surfaces lubricated with a tertiary-butyl phenyl phosphate (TBPP) lubricant and also with a cyclophosphazene lubricant. Abrasive iron oxides, with significantly less graphite, were identified on surfaces lubricated with a polyphenylether lubricant. The difference in deposition films is attributed to the phosphate structure formed by the organophosphorus lubricants. Additionally, AES depth profiles indicate that mass diffusion is involved in the formation of vapor deposition films for several of the lubricants tested. Subsurface stress gradients and chemical surface reactions participate in the diffusion process. Candidate lubricants were also evaluated in full-scale bearings at gas turbine engine conditions. The TBPP lubricant, T15 bearing steel, silicon nitride rolling elements, C-C composite bearing cages, and oil-mist delivery provided the best performance; demonstrating sustained operation at temperatures up to 450 deg C, stress loads up to 1.8 GPa, and bearing speeds of 1.3 MDN. These conditions represent the limitations of the bearing tester, not the technology itself.				
14. SUBJECT TERMS  Vapor lubrication, high temperature lubrication, high temperature bearings			15. NUMBER OF PAGES 263	
			16. PRICE CODE	
17. SECURITY CLASSIFICATION OF REPORT  Unclassified	18. SECURITY CLASSIFICATION OF THIS PAGE  Unclassified	19. SECURITY CLASSIFICATION OF ABSTRACT  Unclassified	20. LIMITATION OF ABSTRACT  U	

## TABLE OF CONTENTS

List of Figures .....	vi
List of Tables .....	xii
Nomenclature .....	xiv
Preface.....	xvi
CHAPTER	
1. INTRODUCTION.....	1
2. MATERIAL EVALUATION.....	6
2.1 Lubricant Selection.....	7
2.2 Bearing Material Selection.....	11
2.3 Test Apparatus and Procedure.....	14
2.4 Factorial Design.....	20
2.5 Factorial Analyses.....	22
2.6 Post-Test Examination.....	30
2.7 Discussion.....	38
3. SYSTEM PERFORMANCE EVALUATION.....	42
3.1 Test Apparatus and Procedure.....	43
3.2 Lubricant Properties and Selection.....	44
3.3 Bearing Temperature Tests.....	50
3.4 Vapor Temperature Tests.....	60
3.5 Solid Lubricant Coating Tests.....	63
3.6 Lubricant Concentration Tests.....	70
3.7 Discussion.....	74



4.	SURFACE ANALYSES.....	79
4.1	Experimental Procedure.....	80
4.2	$\mu$ -FTIR Results.....	83
4.3	Raman Spectroscopy Results.....	98
4.4	AES Results.....	105
4.5	SEM/EDS Results.....	142
4.6	Discussion.....	127
5.	DIFFUSION ANALYSES.....	134
5.1	Theory and Governing Equations.....	135
5.2	Boundary and Initial Conditions.....	142
5.3	Experimental Procedure.....	145
5.4	Analytical Approach.....	148
5.5	Experimental Results.....	152
5.6	Analytical Results.....	161
5.7	Discussion.....	171
6.	HIGH SPEED BEARING TESTS.....	177
6.1	Test Apparatus and Procedure.....	178
6.2	Lubricant Delivery.....	181
6.3	Bearing Geometry and Material Properties...	182
6.4	Vapor Delivery Tests.....	187
6.5	TBPP/TBP Bearing Temperature Tests.....	190
6.6	TBPP/TBP Load Tests.....	193
6.7	TBPP Load Tests without TDC.....	195
6.8	TBPP Load Tests with TDC.....	197
6.9	X-1P Load Tests.....	200
6.10	Bearing Cage Results.....	202
6.11	Test Summary.....	204
6.12	Discussion.....	206
7.	CONCLUSIONS.....	209

8.	FUTURE WORK.....	218
9.	REFERENCES.....	219

#### APPENDICES

A.	Hertzian Stress Calculations.....	228
B.	Nonlinear Regression Calculations.....	231
C.	Diffusion Calculations.....	233

## LIST OF FIGURES

1. The molecular structure of tricresyl phosphate (TCP)...	10
2. The molecular structure of the primary component in the tertiary-butyl phenyl phosphate (TBPP) lubricant.....	10
3. The molecular structure of molecules found in the cyclophosphazine candidate lubricant (X-1P).....	10
4. Cross section of the high temperature ball-on-rod tester.....	17
5. Vapor phase lubrication system.....	19
6. Ninety percent confidence bands for the mean response of the friction coefficient.....	27
7. Ninety percent confidence bands for the mean response of the bearing wear rate.....	28
8. Ninety percent confidence bands for them mean response of bearing life.....	29
9. Optical micrograph of the wear track developed after 96 hours of testing with a T15 rod and TBPP vapor delivered at 1.17 ml/hr.....	33
10. Profilometry trace of the wear track developed after 96 hours of testing with a T15 rod and TBPP vapor delivered at 1.17 ml/hr.....	34
11. Wear track developed with a T15 rod and a 2 cSt polyalphaolefin lubricant (PAO) vapor delivered at 3.40 ml/hr.....	35
12. Wear track developed after 96 hours of testing with X-1P delivered at 1.17 ml/hr.....	36

13.	Wear track developed after 96 hours of testing with a T15 rod and the PAO fluid blended with 15 percent TBPP (PAO/TBPP) delivered at 3.40 ml/hr.....	37
14.	Molecular structure of tributyl phosphate (TBP).....	47
15.	Molecular structure of a five-ring polyphenyl ether (5P4E) .....	47
16.	Temperature-viscosity graph of the TBPP fluid blended with 33 percent TBP (TBPP/TBP) compared to a 4 cSt polyol ester aircraft engine lubricant.....	48
17.	Bearing temperature test with the PAO/TBPP lubricant.....	53
18.	Bearing temperature test with the TBPP lubricant.....	54
19.	Bearing temperature test with the TBPP/TBP lubricant.....	55
20.	Bearing temperature test with the X-1P lubricant.....	56
21.	Bearing temperature test with the 5P4E lubricant.....	57
22.	Bearing temperature test with a linear perfluoroalkylether (Z) lubricant.....	58
23.	Vapor temperature test with the TBPP lubricant.....	61
24.	Vapor temperature test with the X-1P lubricant.....	62
25.	Five cold-start tests with a solid lubricant applied to the bearing samples.....	65
26.	Five cold-start tests without the solid lubricant coating.....	66
27.	Optical micrograph of the bearing track formed after the cold-start tests with the initial application of a solid lubricant coating.....	67

28.	Optical micrograph of the bearing track formed after the cold-start tests without the initial application of a solid lubricant coating.....	68
29.	Scanning electron microscopy (SEM) image of a surface pit formed on the uncoated rod during the cold-start tests.....	69
30.	The effect of lubricant flow rate on the bearing friction coefficient.....	72
31.	The effect of lubricant flow rate on the bearing wear rate.....	73
32.	Fourier transform infrared (FTIR) spectrum of a rod specimen lubricated with TBPP vapor outside of the wear track, 4000 $\text{cm}^{-1}$ to 2000 $\text{cm}^{-1}$ .....	87
33.	FTIR spectrum of a rod specimen lubricated with TBPP vapor outside of the bearing track, 2000 $\text{cm}^{-1}$ to 700 $\text{cm}^{-1}$ .....	88
34.	FTIR spectrum of iron phosphate produced by the reaction of phosphoric acid on an iron surface.....	89
35.	FTIR spectrum of a rod specimen lubricated with TBPP vapor inside the wear track.....	90
36.	FTIR spectrum of the TBPP lubricant prior to test....	91
37.	FTIR spectrum of a T15 ball lubricated with TBPP vapor.....	92
38.	FTIR spectrum of rod after the bearing temperature test with TBPP vapor.....	93
39.	FTIR spectrum of a $\text{Si}_3\text{N}_4$ ball lubricated with TBPP vapor.....	94

40.	FTIR spectrum of the rod after the bearing temperature test with PAO/TBPP vapor.....	95
41.	FTIR spectrum of the rod after the bearing temperature test with X-1P vapor.....	96
42.	FTIR spectrum of the rod after the bearing temperature test with 5P4E vapor.....	97
43.	Raman spectrum of the rod outside the bearing track after the bearing temperature test with TBPP vapor..	100
44.	Raman spectrum of the rod inside the bearing track after the bearing temperature test with TBPP vapor..	101
45.	Raman spectrum of the rod inside the bearing track after the bearing temperature test with PAO/TBPP vapor.....	102
46.	Raman spectrum of the rod after the bearing temperature test with X-1P vapor.....	103
47.	Raman spectrum of the rod after the bearing temperature test with 5P4E vapor.....	104
48.	Auger depth profile of a TBPP deposition film formed in the bearing track.....	109
49.	Auger depth profile of an unused T15 rod.....	110
50.	Auger spectrum formed in the bearing track separate of a corrosion pit.....	111
51.	Auger spectrum of the region associated with corrosion pitting.....	112
52.	Auger depth profile of the region associated with corrosion pitting.....	113
53.	Sectioned rod mounted in epoxy after polishing.....	116

54.	SEM image of a corrosion pit penetrating into the subsurface.....	117
55.	Boundary of the corrosion pit with the normal T15 steel.....	118
56.	Energy dispersive spectroscopy (EDS) spectrum of region "A" in Fig. 55.....	119
57.	EDS spectrum of region "B" in Fig. 55.....	120
58.	EDS spectrum of region "C" in Fig. 55.....	121
59.	EDS spectrum of region "D" in Fig. 55.....	122
60.	EDS spectrum of region "E" in Fig. 55.....	123
61.	EDS spectrum of region "F" in Fig. 55.....	124
62.	EDS spectrum of region "G" in Fig. 55.....	125
63.	Structures of typical condensed phosphate crystals..	132
64.	Structures of typical condensed phosphate glasses...	133
65.	Boltzman-Matano method for calculating the diffusion coefficient.....	140
66.	Wear at the bearing surface and it's relationship to the Matano interface.....	144
67.	Auger electron spectroscopy (AES) depth profiles for TBPP deposition films at 370°C obtained in the bearing track..	155
68.	AES depth profile of 5P4E deposition film inside of the bearing track .....	156
69.	AES depth profiles for the TBPP lubricant at 430°C..	157
70.	AES depth profile at 430°C .....	158

71.	Bearing specimens from Sample Set 14 approximately 30 minutes after liquid N <sub>2</sub> quench .....	159
72.	Cooling rate of the bearing specimens with liquid N <sub>2</sub> quench .....	160
73.	Comparison of regression fits for Dt with the experimental AES data.....	167
74.	Concentration gradient for iron, concentration gradient for carbon, and sum of the concentration gradients	169
75.	Flux relative to the fixed-end coordinate system ...	170
76.	Cross section of the High Speed Bearing Tester.....	180
77.	Full scale bearing test with TBPP vapor.....	188
78.	AISI 4340 cage used in the vapor delivery test.....	189
79.	Full scale bearing temperature test with TBPP/TBP oil-mist lubrication.....	192
80.	Full scale bearing load test with TBPP/TBP oil-mist lubrication.....	194
81.	Full scale bearing load test with TBPP oil-mist lubrication and uncoated races.....	196
82.	Full scale bearing load test with TBPP oil-mist lubrication and TDC coated races.....	199
83.	Full scale bearing load test with X-1P oil-mist lubrication.....	201
84.	Uncoated T15 bearing races, Si <sub>3</sub> N <sub>4</sub> rolling elements, and the C-C composite cage after test with TBPP oil-mist lubrication.....	203



## LIST OF TABLES

1. Chemical Composition (wt%) of Candidate Bearing Materials.....	13
2. Test Conditions for the Material Evaluation.....	18
3. Test Matrix and Results for the Material Evaluation .....	24
4. Analysis of Variance Results for the Friction Coefficient.....	25
5. Analysis of Variance Results for the Wear Rate.....	25
6. Analysis of Variance Results for the Bearing Life.....	26
7. Physical Properties of the Test Lubricants Compared to a 4 cSt Polyol Ester Lubricant.....	49
8. Thermogravimetric Analysis Data .....	59
9. Maximum Bearing Temperature for Sustained Operation....	59
10. Samples Selected for Surface Analyses.....	82
11. Auger Elemental Analysis of a TBPP Deposition Film...107	
12. Auger Elemental Analysis of a TBPP Corrosion Pit.....108	
13. Composition of a Sectioned Wear Track.....126	
14. Additional Samples Generated for AES Depth Analysis.....147	
15. Regression Results for Dt in the Bearing Track .....	165
16. Results of Darken's Analysis for $0 \leq K = D_C/D_{Fe} \leq 1.0$ .....	166

17. Test Bearing Geometry.....	185
18. Bearing Material Properties at 500°C.....	186
19. Summary of the High Speed Bearing Test Results.....	205

## NOMENCLATURE

$\nu$	=	Kinematic viscosity (cSt)
$A$	=	Empirical constant for Walther's equation
$B$	=	Empirical constant for Walther's equation
$T_K$	=	Absolute temperature (K)
$C$	=	Concentration gradient (At %)
$t$	=	Time (s)
$x$	=	Distance relative to the Matano interface (nm)
$D$	=	Diffusion coefficient (nm <sup>2</sup> /s)
$Fe$	=	Subscript for the iron surface
$C$	=	Subscript for the carbon surface
$+\infty$	=	Superscript for the concentration at $x = +\infty$
$-\infty$	=	Superscript for the concentration at $x = -\infty$
$m$	=	Subscript for the specific location of the Matano analyses
$C_T$	=	Total concentration

$D^*$	=	Self-diffusion coefficient
$\Delta w/\Delta t$	=	The averaged wear rate (nm/s)
$dw/dt$	=	The instantaneous wear rate (nm/s)
$d$	=	Distance from the bearing surface to the Matano interface (nm)
$o$	=	Subscript for the Arrhenius equation
$R$	=	Universal gas constant (kJ/mol)
$E$	=	Activation energy (kJ/mol.K)
$Q$	=	Total bearing power loss (W)
$M$	=	Bearing torque (N-m)
$\omega$	=	Shaft speed (rad/s)
$N$	=	Shaft speed (rpm)
$T$	=	Initial static bearing temperature ( $^{\circ}\text{C}$ )
$\Delta T$	=	Temperature rise above $T$ ( $^{\circ}\text{C}$ )
$L$	=	Applied thrust load (N)
$\theta$	=	Circumferential direction of the cage
$z$	=	Axial direction of the cage
$r$	=	Radial direction of the cage

## PREFACE

This technical report was prepared by the Lubrication Branch, Fuels and Lubrication Division, Aero Propulsion and Power Directorate, Wright Laboratory, Air Force Materiel Command, Wright-Patterson Air Force Base, Ohio 43433-7103. The work herein was accomplished under Program Element 62203F, Project 3048, Task 304806, Work Unit 30480619 and Program Element 61102F, Project 2308, Task 2308BW80, during the period January 1994 to December 1996 with Dr. Nelson H. Forster as project engineer and principal investigator. Special acknowledgment is given to the following individuals for significant contributions during the course of the research: Dr. E. Earl Graham, Cleveland State University, Cleveland, OH, for many interesting discussions on the subject of vapor lubrication; Messrs. Hitesh K. Trivedi, David T. Gerardi, and John T. Murry, UES, Inc., Dayton, OH, for test support; Mrs. Cheryl M. McCormick, WL/POSL, Wright Patterson AFB, OH, for help in

preparing the manuscript; Dr. Hugh C. DeLong, Chemistry and Life Sciences Division, Air Force Office of Scientific Research, Bolling AFB, DC, for a research grant sponsoring the surface and diffusion analyses; Dr. Andre' J. Sommers, Miami University, Oxford, OH, for  $\mu$ -FTIR and Raman spectroscopy data; Messrs. Tom N. Wittberg and Jim R. Hoenigman, University of Dayton, Dayton, OH, for AES data; Mr. Christopher J. Klenke, WL/POSL, Wright Patterson AFB, OH, for SEM and EDS data; Mr. John Woodhouse, UES, Inc. Dayton, OH, for SEM and EDS data; Messrs. Arvind M. N. Rao and Douglas G. Placek, FMC Corp., Princeton, NJ, for supplying the TBPP lubricant; And Dr. Ted Morgan, Dow Chemical Co., Midland, MI, for supplying the X-1P lubricant.

## CHAPTER 1

### INTRODUCTION

The development of high speed rolling element bearings operating beyond the temperature limits of synthetic liquid lubricants has been a research objective for more than four decades. The primary application motivating this research has been the gas turbine engine. During this time, the majority of the research has focused on solid lubricants delivered as airborne powders (1-4), or as films transferred from the sliding surfaces of bearing cages (5-8). Both of these methods provide adequate lubrication for lightly loaded, low speed applications. However, both methods have demonstrated limited success at conditions required for gas turbines; i.e., bearings speeds of 1.0 to 2.5 MDN ( $\text{MDN} = 10^{-6} \times \text{shaft diameter in mm} \times \text{shaft rpm}$ ) and bearing stress loads of 1 to 2 GPa. Bearing wear, cage fracture, and seizure due to thermal growth, are the common modes of failure in high speed, solid lubricated rolling element bearings.

The origins of vapor lubrication can also be traced back to the early period of high temperature lubrication research. In the mid-1950's, Coit, et al. (9) lubricated 206 (30mm bore) and 209 (45mm bore) ball bearings with vapor produced from JP-4 jet fuel blended with 0.67 wt % triisopropyl phosphite. Several tests were conducted on 209 bearings with an applied radial load of 2670 N, 371°C bearing temperature, and 0.32 MDN bearing speed, with good results. Bearing temperatures, as high as 538°C, were also obtained in the 209 bearing tests, when JP-4 was replaced with polyalkylene glycol. In the 206 bearing tests, bearing speeds up to 0.62 MDN were obtained with lightly loaded bearings. Cage wear and fracture were the common modes of failure at 0.62 MDN.

Although the research performed by Coit, et al., was reasonably successful, it was not until the 1980's that vapor phase lubrication received a sustained level of effort, which today exists in three distinct forms: vapor phase deposition (VPD), where organic vapors are intentionally reacted with a hot bearing surface to form the lubricating film (10-20); vapor phase condensation (VPC), where vapors are condensed on a bearing surface to essentially maintain liquid lubrication



(20,21); and gaseous lubrication, where light-weight hydrocarbon gases are deposited on a hot catalytic nickel surface (22,23). The concept of VPD lubrication was initiated and substantially developed by the late Professor E.E. Klaus at The Pennsylvania State University. Additional and significant contributions to VPD lubrication have continued under the direction of Professor E.E. Graham at Cleveland State University. The concept of VPC lubrication was first introduced by Klaus but has since been substantially developed by Dr. Lavern Wedeven of Wedeven Associates, Edgmont, Pennsylvania. The concept of gaseous lubrication is a result of the continuing research of Professor J.L. Lauer at Rennselaer Polytechnic University. The research conducted here focuses on VPD lubrication, although as shown in Chapters 3 and 6, VPD candidate lubricants also function as condensate lubricants.

The objective of the research was to elucidate the mechanisms of VPD lubrication, with the end goal of successfully demonstrating the VPD concept in high speed rolling element bearings. For practical considerations all of the testing was performed in an air environment. With the

exception of the research reported in references 16-19, previous VPD tribological testing had been performed in N<sub>2</sub> atmosphere. To accomplish the research objective, the following approach was taken:

1. Candidate lubricants and high temperature bearing materials were evaluated in subscale bearing tests to identify promising materials for continued development.
2. Parametric testing was performed to identify critical parameters in designing a vapor phase lubrication system.
3. Analytical surface techniques were applied to investigate the lubrication and failure mechanisms of vapor lubricated bearings.
4. Surface diffusion mechanisms were investigated experimentally and analytically. The results give

further insight into the lubrication and failure mechanisms of vapor lubricated bearings.

5. Full scale bearing tests were conducted at conditions projected for an advanced gas turbine engine. Carbon-carbon bearing cages (C-C) and oil-mist delivery of the candidate lubricants were added to the testing, to improve bearing performance.

## CHAPTER 2

### MATERIAL EVALUATION

It had previously been shown that tricresyl phosphate (TCP) (16), cyclophosphazene (17), and a tertiary-butyl phenyl phosphate lubricant (17) performed well in rolling contact tests with M50 bearing steel and AISI 4340 bearing cages at temperatures of 370°C. However, it was not clear which lubricant performed the best, particularly in long term tests. Additionally, M50 bearing steel loses hardness at operating temperatures slightly above 370°C. The objective of the research described in Chapter 2 was to evaluate initial candidate VPD lubricants with candidate bearing materials selected for high temperature operation. Factorial analyses were performed to determine the relative contributions of the various materials. Bearing friction, wear, and life were used as the measures of performance.

## 2.1 Lubricant Selection

The criteria considered in the lubricant selection were; toxicity, fire resistance, boundary film lubrication characteristics, thermal and oxidative stability, and temperature-viscosity index. Based on these criteria, the following lubricants were selected: a blend of tertiary-butyl phenyl phosphate molecules (TBPP) (24), a blend of cyclophosphazene molecules (X-1P) (25), a 2 cSt unformulated polyalphaolefin (PAO), and the PAO fluid blended with 15 percent TBPP (PAO/TBPP). Tricresyl phosphate (TCP), by far the most widely used VPD lubricant, was not considered, due to toxicity considerations with the ortho-isomer (26,27). Polyol esters were also not considered, due to a highly toxic reaction, which occurs between trimethylolpropane esters and triaryl phosphate esters at elevated temperatures (28,29).

The molecular structures for TCP and molecules of TBPP and X-1P are shown in Figs. 1-3. Structurally, TBPP is similar to TCP, with the exception of the substituent on the phenyl ring. The size of the t-butyl substituent sterically hinders the formation of the ortho-isomer, substantially reducing the risk of neurotoxicity. Oral dose testing, with

TBPP molecules applied to the adult hen in the neat condition, have shown little or no neurotoxic effect (30,27).

However, TBPP has been associated with reproductive toxicity in rodents, when administered in an oral dose of 1.7 g/kg (31,32). In comparison, TCP is a more severe reproductive toxicant at an oral dose of 0.4 g/kg (31,32). Preliminary toxicity testing with X-1P has shown the oral LD<sub>50</sub> in rats to be >2.0 g/kg (25). Toxicity testing with TBPP and X-1P vapors is underway to evaluate toxicity effects from the vapor phase. In reference to the other selection criteria, both TBPP and X-1P have excellent fire resistance (24,33), boundary film lubrication characteristics (24,34), and thermal/oxidative stability (35,25). However, both lubricants have relatively poor temperature-viscosity properties.

In application, tribological systems using VPD lubrication will, typically go through a start-up period, requiring liquid lubrication. During this period, temperature-viscosity and other liquid lubrication properties may be critical. The PAO fluid was selected to potentially bridge this gap. However, preliminary VPD tests, with the PAO fluid in the neat condition, showed essentially no

lubricating effect. To improve performance, the bearing specimens were pretreated for a period of 2 hours of operation with the TBPP vapor, followed by testing with the unformulated PAO vapor. As a second approach, the PAO fluid was blended with 15 percent TBPP and used without pretreatment. Klaus and Duda used a similar approach, blending super refined mineral oil with TCP (20). Their results indicated the blended lubricant produced lower wear scars in the sliding four-ball test than either mineral oil or TCP alone. In the present effort, both pretreatment and blending were sufficient to make the PAO a viable vapor phase lubricant.

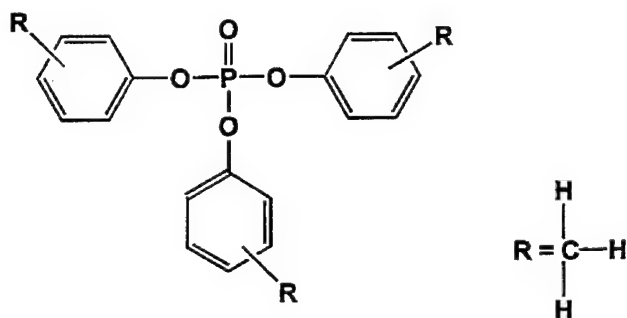


Figure 1. The molecular structure of tricresyl phosphate (TCP).

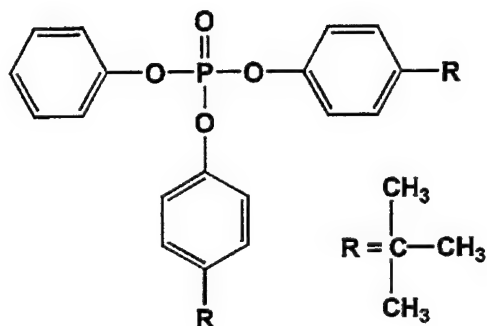


Figure 2. The molecular structure of the primary component in the tertiary-butyl phenyl phosphate (TBPP) lubricant.

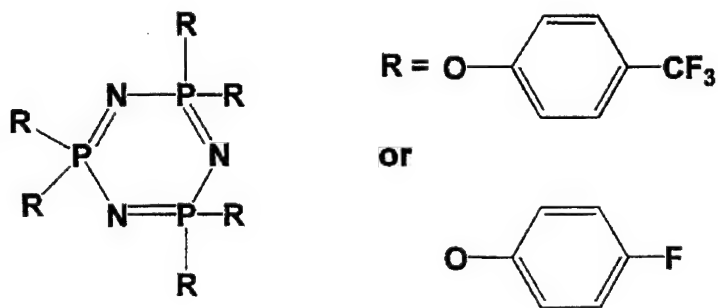


Figure 3. The molecular structure of molecules found in the cyclophosphazine candidate lubricant (X-1P).



## 2.2 Bearing Material Selection

Candidate bearing materials were selected, based on high temperature properties and chemical composition. One of the goals in the bearing material evaluation was to assess the relative importance of iron in the VPD process. TCP is known to react with ferrous alloys in the liquid state (36,37) and from the vapor phase (38). To generate a ferrous based system, T15 tool steel was selected as the material for the bearing races and rolling elements, with AISI 4340 steel for the bearing cages. The T15 steel was heat treated to achieve a tempered martensitic structure with a Rockwell C hardness of 64. T15 resists retempering at temperatures up to 450°C, which gives the steel excellent hardness retention at elevated temperatures. For the nonferrous system, the T15 races were coated with thin dense chrome (TDC). NBD 200  $\text{Si}_3\text{N}_4$  was used for the rolling elements, and Monel 400, a nickel/copper alloy, was used for the bearing cage. A secondary consideration in the selection of the nonferrous materials was their inherent oxidation resistance at elevated temperatures. The nominal thickness of the TDC coating was 2

microns. The elemental compositions of T15, Monel 400, and AISI 4340 steel are listed in Table 1.

---

Table 1. - Chemical Composition (wt %) of Candidate Bearing  
Materials

---

	C	Mn	Si	Cr	V	W	Mo	Co	Ni	Cu
T15	1.55	.30	.30	4.0	5.0	12.25	-	5.0	-	-
Monel 400	-	-	-	-	-	-	-	-	66	32
AISI 4340	.40	.90	.30	.80	-	-	.20	-	1.7	-

---

### 2.3 Test Apparatus and Procedure

A cross section of the high temperature rolling contact tester is shown in Fig. 4. The tester is based on the ball-on-rod tester, originally developed by Glover for rolling contact fatigue testing of bearing steels at ambient temperature (39). In the present configuration, the tester is used to screen high temperature materials, prior to full-scale bearing tests (40). The bearing test specimens consist of the rotating rod, three balls, a bearing cage, and two tapered races. The diameters of the ball and rod are 12.70mm and 9.52mm, respectively. The material used for the rod and tapered races is collectively referred to as the race material in the factorial analyses.

As shown in Fig. 4, the outer structure containing the tapered races is supported by a hydrostatic air bearing. Rotation of the structure is constrained by a thin wire connected to a load transducer. The force at the load transducer is proportional to the frictional force at the tapered races, by the ratio of the respective moment arms. The friction coefficient for the various material combinations was calculated from the mean friction force at

the tapered races, divided by the applied normal load between the rolling elements and tapered races.

To accelerate bearing failure, very high Hertzian contact stresses were used. The maximum Hertzian contact stress was 3.34 GPa for the metallic specimens and 3.65 GPa for combinations with  $\text{Si}_3\text{N}_4$  rolling elements. An accelerometer measures the bearing vibration and the resulting signal is used to terminate the test if the vibration reaches a level consistent with rolling contact fatigue initiation. The tests were suspended at 96 hours if they did not fail from vibration.

After testing, the wear track on each rod was examined, using a metallurgical microscope and a profilometer. The volumetric wear rate was calculated for each track, using the averaged wear volume from three profilometry traces and the number of stress cycles completed.

A schematic of the vapor phase lubrication system is shown in Fig. 5. Vapor was generated by introducing the liquid at ambient conditions into a heated stainless steel tube, 25mm in diameter by 200mm long. Shop air was used as the carrier gas, at a flow rate of 283 l/hr. A thermocouple

on the downstream side of the vapor chamber was used to monitor and control the vapor temperature.

Environmental operating conditions used in the testing are summarized in Table 2. The lubricant flow rate for the TBPP and X-1P was set at 1.17 ml/hr, based on previous work conducted by Rao (17). A higher flow rate of 3.4 ml/hr was used with the PAO and PAO/TBPP, tests to improve bearing performance. Vapor temperatures were selected, based on the level required to generate a clearly visible stream of effluent exiting the test head. The bearing operating temperature was monitored and controlled by a thermocouple mounted to the upper race. The ambient air temperature near the ball-on-rod contact was typically 25°C less than the tapered race temperature.

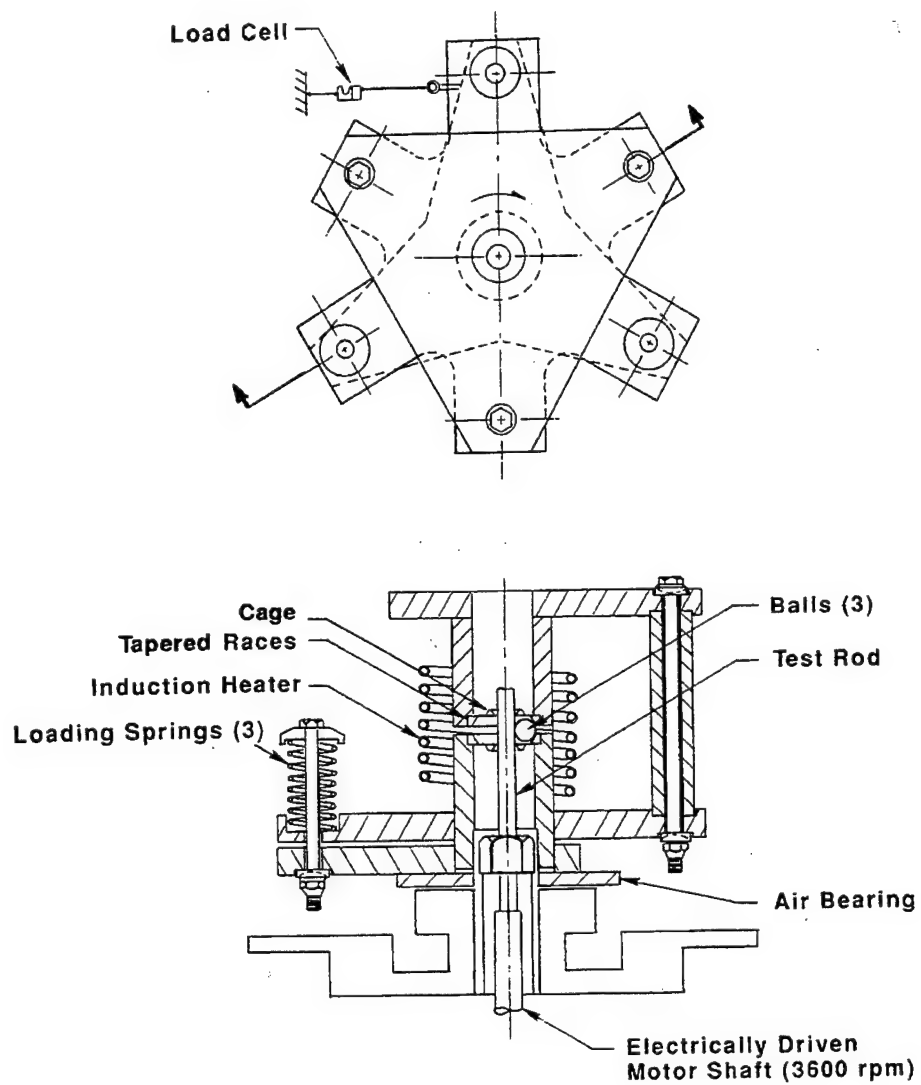


Figure 4. Cross section of the high temperature ball-on-rod tester.

---

Table 2. - Test Conditions for the Material Evaluation

---

Speed: 3600 rpm

---

Load:	Metallic 3.34 GPa	Hybrid 3.65 GPa
-------	----------------------	--------------------

---

	Temperature (°C)		Lubricant Flow Rate
	<u>Vapor</u>	<u>Bearing</u>	<u>(mL/hr)</u>
TBPP	330	370	1.17
PAO+	243	370	3.40
PAO*	243	370	3.40
X-1P	370	370	1.17

---

\* Initially pretreated for a period of 2 hours with TBPP at 330°C



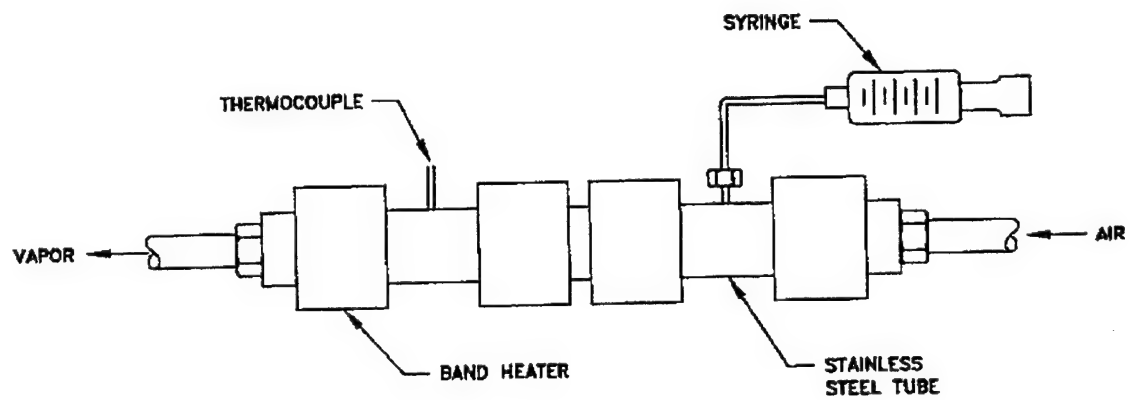


Figure 5. Vapor phase lubrication system.

## 2.4 Factorial Design

A half fraction factorial design (41) was used to generate the test matrix for the cage, race, and ball material. This matrix was then repeated for each lubricant. The type of lubricant, cage material, race material, and ball material are referred to as the design factors. Within each factor are levels, i.e., TDC vs. T15 represents two levels for the factor, race material. Bearing friction, wear, and life were used as the response variables to measure the bearing performance. Analysis of variance (ANOVA) (42) with Type I Sum of Squares was used to determine if a factor made a statistically significant contribution to the bearing performance. The significance of a factor was determined from the F-ratio, which represents the ratio of the estimated variance within factors to the estimated variance between factors. If this ratio is high, then the probability that the factor is significant in determining the measured response is also high. The significance level in the ANOVA table represents the probability of obtaining the F-ratio by chance. A low significance level indicates the factor was influential in determining the measured response. If the

significance level is less than or equal to 0.10, then the factor can be interpreted as being statistically significant at the 90 percent confidence level. The Tukey method of multiple comparisons (43) was used to determine if a particular level had an adverse or beneficial effect on bearing performance.

## 2.5 Factorial Analyses

Results for the factorial design are summarized in Tables 3-6. Analyses of the residuals were performed as a preliminary step to determine the suitability of the ANOVA model for the response data. For the friction coefficient response, the logarithm of the friction coefficient was used to stabilize the variance (44). This provided a small but beneficial improvement in the model response. The residual analyses for wear and life indicated that the model was suitable without transformation of the response variable.

The ANOVA results for the friction coefficient indicate that the lubricant is the most significant factor. The graph for the lubricant level response in Fig. 6, indicates that X-1P produces the highest friction and the measured response is statistically different than the PAO/TBPP fluid at the 90 percent confidence level. In general, Fig. 6 suggests that ferrous systems generate lower friction than nonferrous systems.

The ANOVA results for the bearing wear rate indicate that the type of lubricant and ball material has the most effect on the bearing response. The responses of the factor

levels are graphed in Fig. 7. Results indicate that the PAO and PAO/TBPP lubricants produce a similar response and the wear generated is less than that obtained with the TBPP or X-1P lubricants. The results also indicate that  $\text{Si}_3\text{N}_4$  rolling elements produce more wear than T15 rolling elements.

The ANOVA results for the bearing life indicate that the type of lubricant and race material has the most effect on bearing life. The responses of the factor levels are graphed in Fig. 8. Results indicate that the PAO fluid and TDC races have an adverse effect on bearing life. Due to the number of suspensions, the lubricant which promotes the longest life could not be determined. Fig. 8 also indicates that Monel 400 may have a beneficial effect on life; however, the results are not conclusive at the 90 percent confidence level.

Table 3. - Test Matrix and Results for the Material Evaluation

LUBE	CAGE	ROD/ RACES	BALL	FRICTION COEFFx10 <sup>4</sup>	WEAR RATE (μm <sup>3</sup> /cycle)	TIME (hrs)
TBPP	Monel	T15	Si <sub>3</sub> N <sub>4</sub>	7.91	41.08	96.0
TBPP	4340	TDC	Si <sub>3</sub> N <sub>4</sub>	6.13	28.75	96.0
TBPP	4340	T15	T15	3.13	8.88	96.0
TBPP	Monel	TDC	T15	5.06	28.55	96.0
PAO	Monel	T15	Si <sub>3</sub> N <sub>4</sub>	3.91	9.25	77.8
PAO	4340	TDC	Si <sub>3</sub> N <sub>4</sub>	6.91	7.39	23.5
PAO	4340	T15	T15	3.70	10.03	61.8
PAO	Monel	TDC	T15	4.76	1.08	12.2
X-1P	Monel	T15	Si <sub>3</sub> N <sub>4</sub>	8.48	28.01	96.0
X-1P	4340	TDC	Si <sub>3</sub> N <sub>4</sub>	7.17	33.57	50.5
X-1P	4340	T15	T15	5.80	21.39	96.0
X-1P	Monel	TDC	T15	16.10	17.84	96.0
PAO+	Monel	T15	Si <sub>3</sub> N <sub>4</sub>	7.58	20.10	96.0
PAO+	4340	TDC	Si <sub>3</sub> N <sub>4</sub>	2.87	5.56	51.6
PAO+	4340	T15	T15	3.59	0.70	96.0
PAO+	Monel	TDC	T15	3.78	3.46	96.0
TBPP	4340	T15	T15	5.68	17.24	96.0

Table 4 - Analysis of Variance Results for the LOG (Friction Coefficient)

Source of Variation	Sum of Squares	d.f.	Mean Square	F-ratio	Sig. level
MAIN EFFECTS					
Lube	1.2640258	3	0.4213419	3.316	0.0653
Cage	0.3950979	1	0.3950979	3.110	0.1083
Steel	0.0385501	1	0.0385501	0.303	0.5996
Ball	0.1115433	1	0.1115433	0.878	0.3806
RESIDUAL	1.2705758	10	0.1270576		
TOTAL (CORRECTED)	3.0797929	16			

Table 5. - Analysis of Variance Results for the Wear Rate

Source of Variation	Sum of Squares	d.f.	Mean Square	F-ratio	Sig. level
MAIN EFFECTS					
Lube	1348.3293	3	449.44311	9.711	0.0026
Cage	98.9022	1	98.90220	2.137	0.1745
Race	3.3620	1	3.36196	0.073	0.7958
Ball	461.2742	1	461.27419	9.966	0.0102
RESIDUAL	462.83788	10	46.283788		
TOTAL (CORRECTED)	2374.7055	16			

---

Table 6. - Analysis of Variance Results for the Bearing Life

Source of Variation	Sum of Squares	d.f.	Mean Square	F-ratio	Sig. level
MAIN EFFECTS					
Lube	6653.0467	3	2217.6822	7.803	0.0056
Cage	532.6881	1	532.6881	1.874	0.2009
Race	2344.6611	1	2344.6611	8.250	0.0166
Ball	200.5102	1	200.5102	0.706	0.4293
RESIDUAL	2841.9624	10	284.19624		
TOTAL (CORRECTED)	12572.868	16			

---



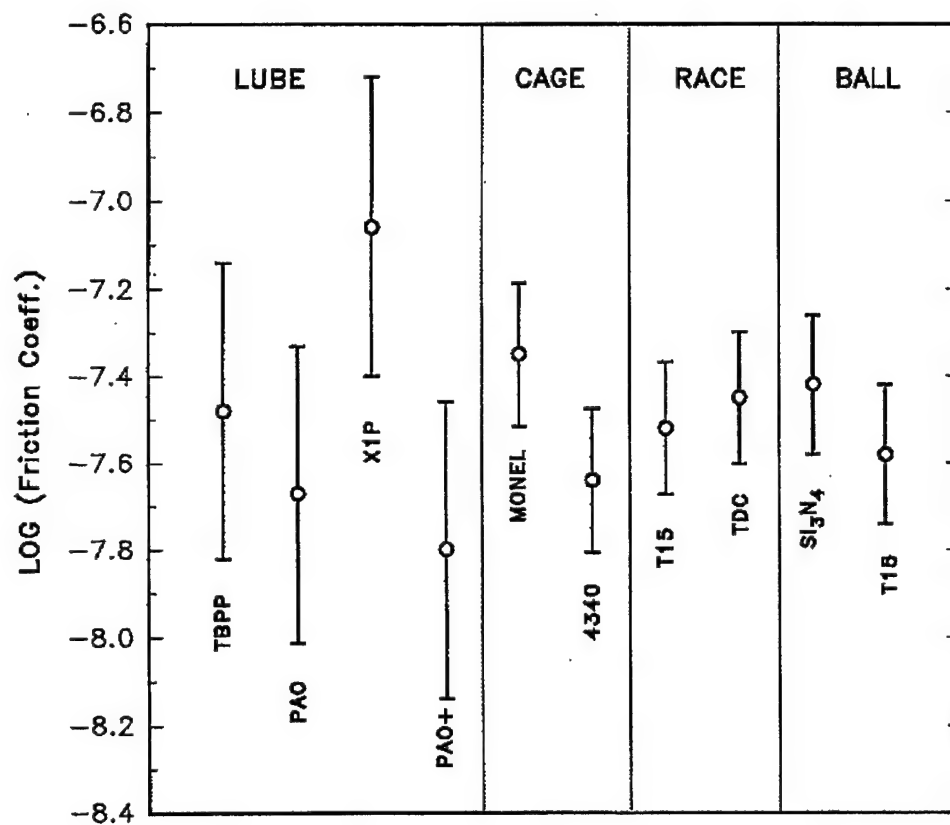


Figure 6. Ninety percent confidence bands for the mean response of friction coefficient.

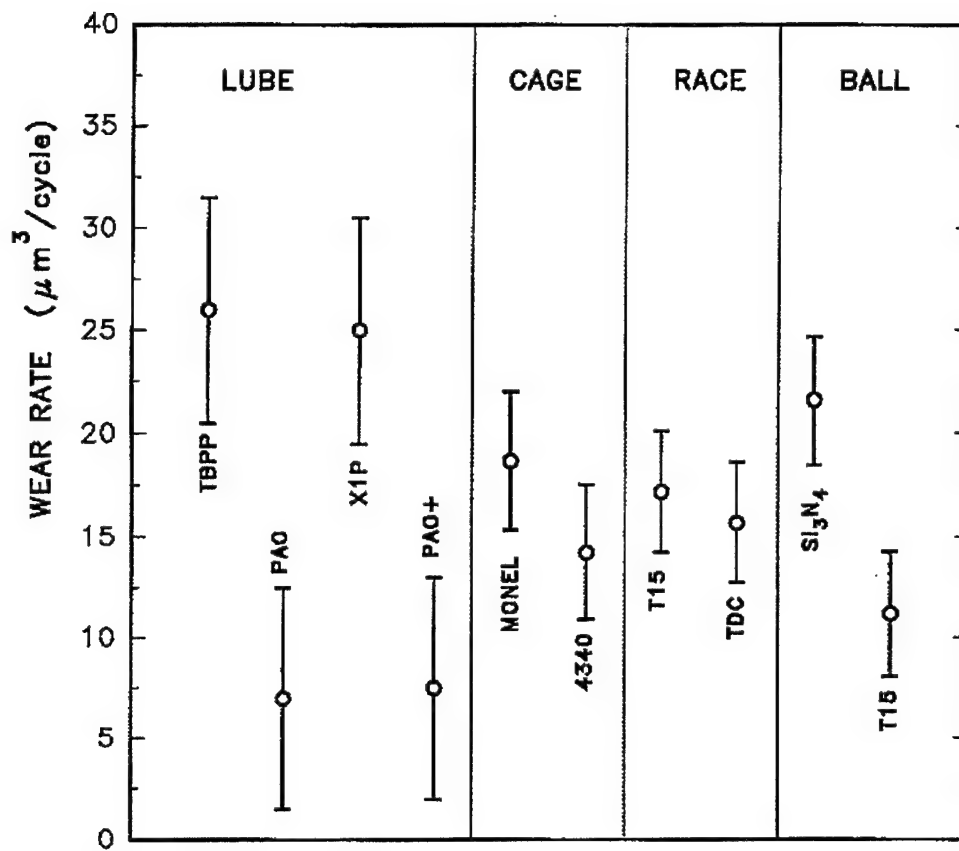


Figure 7. Ninety percent confidence bands for the mean response of bearing wear rate.

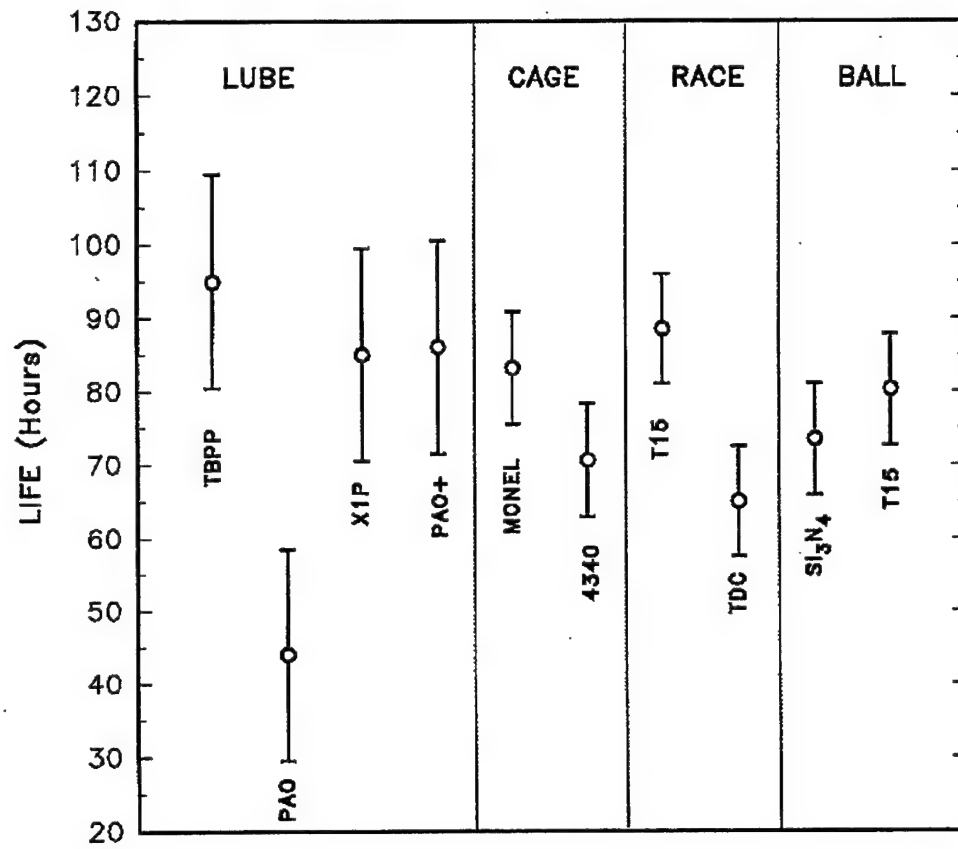


Figure 8. Ninety percent confidence bands for the mean response of bearing life.

## 2.6 Post-Test Examination

A photograph of the bearing track, generated on the rod with TBPP vapor and the ferrous alloy system, is shown in Fig. 9. The track has a highly polished surface, with surface damage consistent with micropitting from corrosion. From the profilometer trace of the wear track shown in Fig. 10, the depth of wear transverse to the rolling direction is closely approximated by an arc of 8.62mm radius. The resulting maximum Hertzian contact pressure is 2.26 GPa, a 32 percent reduction from the initial maximum contact stress. Superimposed on Fig. 9, are the initial and post-test major axes of the contact ellipse, calculated from the Hertzian solution. Also from the Hertzian solution, the maximum tensile stress and surface shear stress, due to elastic deformation, occur at the contact boundary. Using the equations of Timoshenko (45), the magnitude of these stresses, at the point where the elliptical boundary intercepts the major axes, is 0.49 GPa. Microslip in the ball-on-rod contact will also occur in this vicinity to minimize the overall tractive forces. The surface distress seen in the vertical bands of Fig. 9, is attributed to an

excess of the phosphate ion, tensile stress, and surface shear stress due to elastic deformation and sliding. Running horizontally in Fig. 9 is a denser region of micropitting distress. There are three such regions in the bearing track corresponding to the ball spacing, under static conditions. This damage occurred post-test before removing the specimens from the tester. The density of voids is attributed to corrosion along the crevice, created by the ball and rod contact, accelerated by the phosphate ion, tensile stress, and elastic shear stress.

The wear track generated with the PAO lubricant, following pretreatment with TBPP, is shown in Fig. 11. Deposits attributed to oil varnish are present on the bearing surface. All of the specimens, lubricated with the PAO in the vapor phase, show the same type of deposits in the bearing track. While these deposits likely reduced the wear rate, they also contributed to bearing vibration. The shorter lifespan with PAO lubricant is largely attributed to vibration from varnish deposits.

The wear track generated with the X-1P lubricant and the ferrous alloy system is shown in Fig. 12. At a concentration of 1.17 ml/hr, the cyclophosphazene fluid generates a matte

texture with a surface finish of 100 nm  $R_a$ . Although the as-ground surface finish is also 100 nm  $R_a$ , the topography produced by the X-1P fluid is very different.

The bearing track for the PAO/TBPP lubricant and the ferrous system is shown in Fig. 13. A highly polished surface, similar to the track generated with the TBPP vapor, is evident. However, there are no signs of the surface pitting, which was produced with the TBPP at a concentration of 1.17 ml/hr. The surface finish in the track is 10 nm  $R_a$ . The material combination with the PAO/TBPP lubricant, TDC races,  $Si_3N_4$  rolling elements, and 4340 cage, also produces a mirror surface finish. This type of finish was not seen with the other two PAO/TBPP tests, which used a Monel 400 cage, suggesting that debris from the sliding surface of the 4340 cage plays an active role in the polishing effect. This was also consistent for the combinations with the TBPP vapor and the Monel 400 cage.

Examination of the rods coated with TDC, using energy dispersive spectroscopy, indicates the TDC coating was not present in the wear track, after testing. This was not surprising, since the depth of wear for the rod specimens was

typically an order of magnitude larger than the thickness of the TDC coating, which had a nominal value of 2 microns.

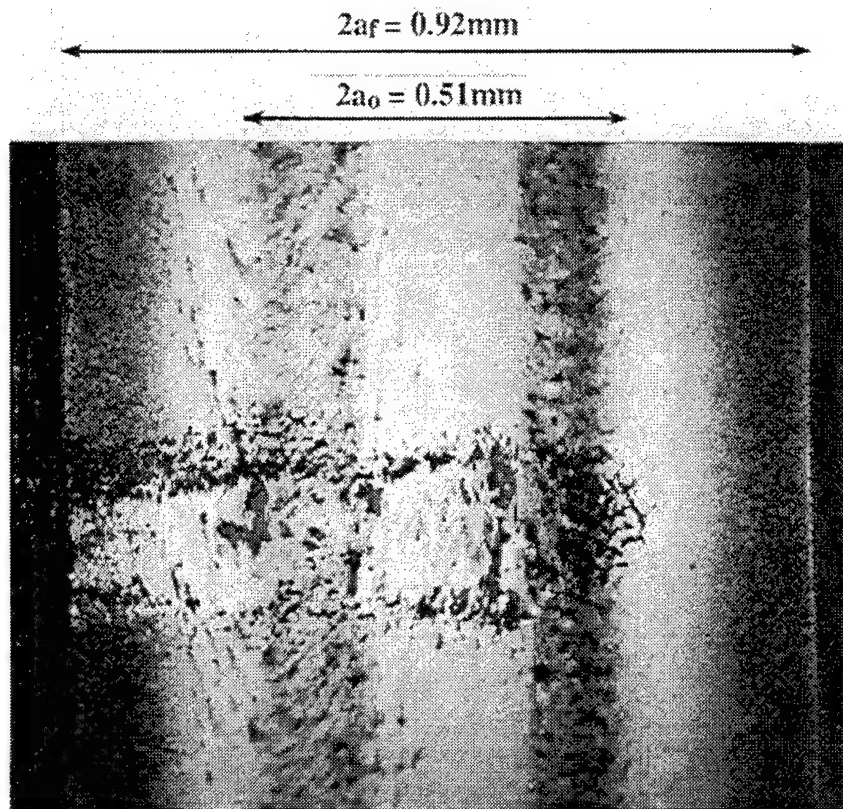


Figure 9. Optical micrograph of the wear track developed after 96 hours of testing with a T15 rod and TBPP vapor delivered at 1.17 ml/hr. The surface distress is attributed to corrosion accelerated by tensile stress.

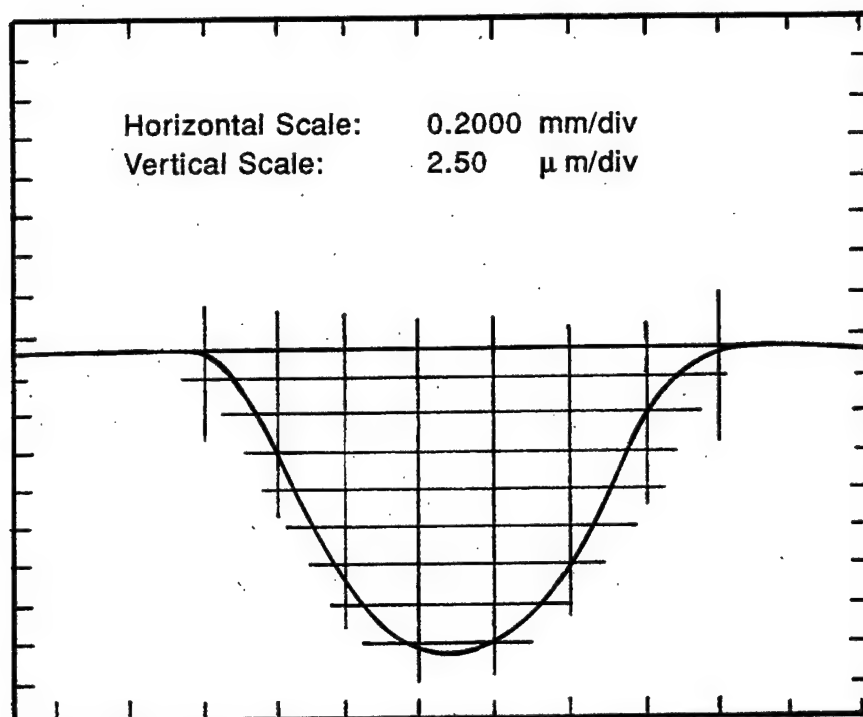


Figure 10. Profilometry trace of the wear track developed after 96 hours of testing with a T15 rod and TBPP vapor delivered at 1.17 ml/hr.



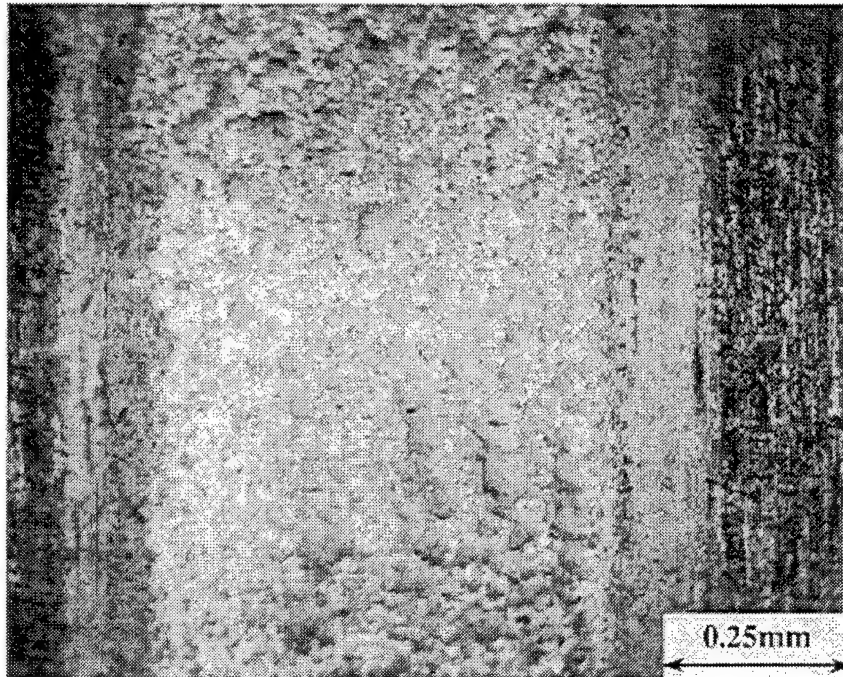


Figure 11. Wear track developed with a T15 rod and a 2 cSt polyalphaolefin lubricant (PAO) vapor delivered at 3.40 ml/hr. The rod was initially lubricated for 2 hours with TBPP vapor delivered at 1.17 ml/hr. The deposits are attributed to oil varnish from the PAO vapor. The test failed due to bearing vibration at 61.8 hours.

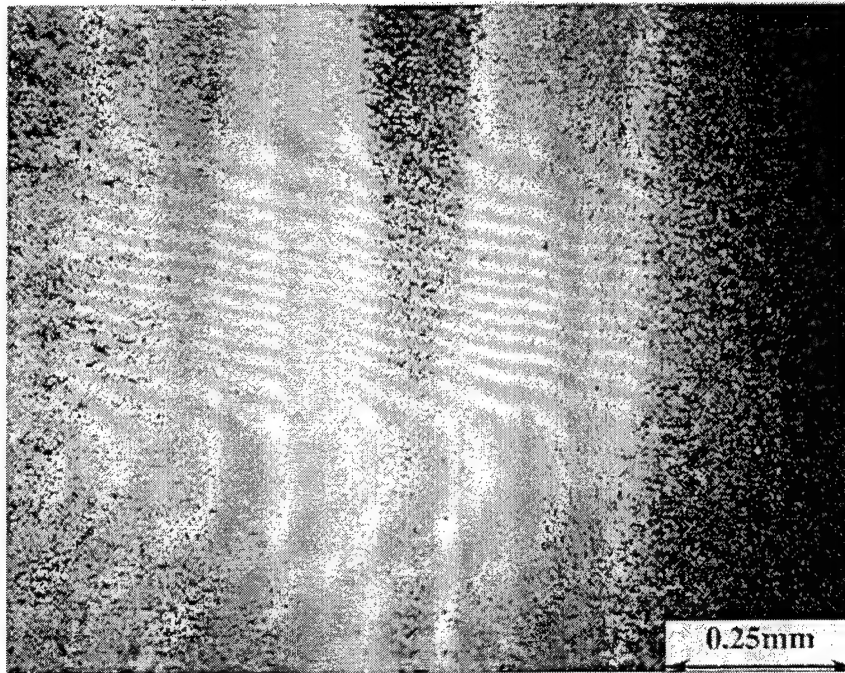


Figure 12. Wear track developed after 96 hours of testing with X-1P delivered at 1.17 ml/hr. The width of the track spans the entire picture. The matte finish is attributed to the presence of fluorine in X-1P.

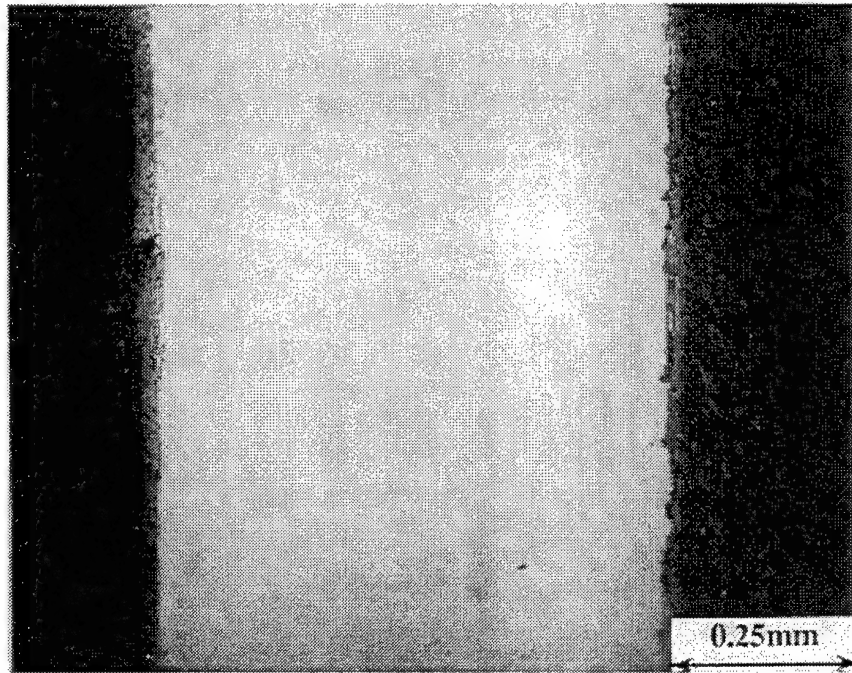


Figure 13. Wear track developed after 96 hours of testing with a T15 rod and the PAO/TBPP lubricant delivered at 3.40 ml/hr. The surface finish in the track is 10 nm compared to 100 nm outside of the track.

## 2.7 Discussion

Initial tests, with a 2 cSt PAO fluid in the neat condition, essentially showed no lubricating effect. However, when the surfaces were pretreated with TBPP vapor for a period of 2 hours under dynamic conditions, and then followed by the PAO lubricant in the neat condition, the ferrous alloy system produced a bearing life of 61.8 hours. The ability to successfully operate a bearing after the TBPP pretreatment is attributed to the initial polishing, produced by the TBPP vapor and the generation of a phosphate film. The presence of phosphate in the lubricating film has been detected on all the material combinations listed in Table 3 and will be discussed in Chapter 4.

The performance of the PAO base stock was further enhanced when blended with 15 percent TBPP. Overall, the PAO/TBPP showed the best performance of the candidate VPD lubricants, for the test conditions listed in Table 3. The performance of the PAO/TBPP lubricant is largely attributed to the highly polished surface generated in the bearing track. The 10 nm finish translates into an order of magnitude improvement in film thickness ratio, when compared

to the as-ground surface finish of 100 nm. Solid or liquid film lubricants have not demonstrated this type of polishing effect in the ball-on-rod test. Thus, an important aspect of the VPD lubrication mechanism appears to be the ability to compensate for thin film lubrication, through chemical polishing. The concept of chemical polishing has been applied by Beeck (46,47) and by Klaus and Fenske (46,48) to explain the anti-wear properties of phosphorus, containing lubricity additives in the liquid phase. In these early papers, the polishing effect was attributed to the formation of a phosphide eutectic. Subsequent papers by Godfrey (36) and Beiber, et al. (37), showed that TCP deposits a phosphate film, rather than a phosphide film, and the role of TCP as a polishing agent was substantially diminished. In the vapor phase it appears that phosphate esters act as both polishing agents and phosphate film formers.

A critical parameter in chemical polishing, from the vapor phase, appears to be the concentration of TBPP. At a concentration of 1.17 ml/hr, TBPP vapor generates a highly polished surface, accompanied with micropitting in regions associated with high tensile and surface shear stress. For the PAO/TBPP test, the concentration of TBPP delivered was

0.51 ml/hr and this mixture did not produce the micropitting seen with the TBPP in the neat condition. Also, the blending of TBPP with the PAO eliminated the oil varnish deposits, which occurred with the PAO fluid in the neat condition. The effect of lubricant concentration on bearing performance is discussed in more detail in Chapter 3.

The effect of ferrous alloys cannot be clearly determined from the test results, since the TDC coating was compromised, due to wear in the bearing track. However, systems with higher iron content, generally, produced lower friction, promoted longer life (except for the specimens with the Monel cage), and reduced the wear rate, particularly for T15 rolling elements compared to  $\text{Si}_3\text{N}_4$  rolling elements. The higher wear rate with  $\text{Si}_3\text{N}_4$  is attributed to the higher modulus of elasticity of ceramics compared to steel, which, in turn, generates a higher Hertzian contact stress for a given load. Additionally, surface analysis of the  $\text{Si}_3\text{N}_4$  rolling elements did not show the phosphate peaks found on T15 rolling elements and T15 rod specimens. Bearing specimens containing AISI 4340 cages produced a more pronounced polishing effect on the rod, than specimens containing Monel 400 cages. Finally, the limited number of

tests conducted can only determine the main effects of the design variables, using statistical analyses. However, the data suggests that interaction effects exist between the lubricants and bearing materials.

### CHAPTER 3

#### SYSTEM PERFORMANCE EVALUATION

The objective of this portion of the project was to examine the relative effect of vapor lubrication system parameters on bearing performance. Parameters included in the evaluation were type of lubricant, bearing temperature, vapor concentration, and vapor temperature. The TBPP, PAO/TBPP, and X-1P lubricants evaluated in Chapter 2 are also discussed in the system evaluation. Additionally, a blend of 67 percent TBPP with 33 percent tributyl phosphate (TBPP/TBP), a polyphenylether (5P4E), a perfluoroalkylether (Z), and a solid lubricant coating were included in this study. Particular emphasis was placed on identifying the system parameters to obtain the best bearing performance over the widest temperature range.



### 3.1 Test Apparatus and Procedure

The ball-on-rod tester described in Chapter 2 was also used to assess the system parameters. As shown in Fig. 4, the test specimens were heated using an induction coil. This feature provides rapid heating of the bearing specimens and was used in this study to simulate the initial temperature conditions found in mechanical systems, which internally generate heat. Gas turbines and internal combustion engines are two examples of heat generating systems. The vapor lubrication system discussed in Chapter 2 was also used in this portion of the research. Consistent with the procedures used in Chapter 2, the bearing temperatures were measured by a thermocouple mounted to the tapered races. For the bearing temperature tests, T15 high temperature tool steel was used for the race and rod material, NBD 200  $\text{Si}_3\text{N}_4$  for the rolling elements, and AISI 4340 for the bearing cage. All of the remaining tests used the same bearing materials, except for the rolling elements, which were T15 tool steel. Also, consistent with the procedure described in Chapter 2, the resulting maximum Hertzian contact stress for the specimens with  $\text{Si}_3\text{N}_4$  rolling elements was 3.65 GPa. The maximum contact

stress for the remaining tests with steel rolling elements was 3.34 Gpa.

### 3.2 Lubricant Properties and Selection

The PAO/TBPP and TBPP lubricants were selected based on the bearing performance obtained in Chapter 2. The X-1P and 5P4E were included in the system evaluation, due to their excellent thermal and oxidative stability properties (25,49). The TBP was blended with the TBPP to improve the low temperature viscosity. The blending of alkyl phosphate esters, i.e., TBP, with aryl phosphate esters, i.e., TBPP, is a technique used for several decades to improve the temperature-viscosity properties of fire resistant hydraulic fluids (50). The molecular structure of the 5P4E and X-1P fluids is sufficiently different from most hydrocarbon based materials and it is difficult to identify fluids which are soluble in them. In turn, this makes it difficult to alter their temperature-viscosity properties to any significant degree. The Z perfluoroalkylether was selected based on the excellent temperature-viscosity properties possessed by this fluid (51) and also due to the nonflammability of the

perfluoroalkylethers. The molecular structures of the TBP and 5P4E are shown in Figs. 14 and 15. The molecular structure of the Z fluid was not found in a search of the public literature. However, it is known that this fluid is a blend of linear molecules of relatively low molecular weight.

To assess the temperature-viscosity properties of the candidate lubricants, viscosity measurements were made in accordance with ASTM D455-88 (52) at 40°C and 100°C. The data were then fitted to Walther's temperature-viscosity equation (53):

$$\text{Eq 1: } \nu = \log^{-1}[\log^{-1}(A - B \log T_k)] - 0.7$$

The temperature required to produce a lubricant viscosity of 20,000 cSt was extrapolated, using Walther's equation. The value of 20,000 cSt is considered the pumpability point for current U.S. Air Force aviation lubricants.

Viscosity data for the candidate lubricants are compared to a 4 cSt polyolester aviation lubricant in Table 7. As shown in Fig. 16, the ratio of the TBP in the TBPP/TBP was selected to give the fluid a temperature-viscosity index

similar to the polyolester. The results indicate that the PAO/TBPP, TBPP/TBP, and Z fluids represent candidate vapor phase lubricants, which also possess good low temperature viscosity properties.

The solid lubricant coating was selected to assist in the lubrication of the bearing, during start-up conditions. Energy dispersive spectroscopy (EDS) analysis indicates the presence of phosphorus, aluminum, lead, and antimony in the coating. The particular EDS system used in the analysis, is unable to detect the presence of oxygen. The results suggest that  $\text{PbO}$  and  $\text{Sb}_2\text{O}_3$  were used as the solid lubricants contained in an  $\text{AlPO}_4$  binder. The prospect of a phosphate binder was considered attractive, due to the possibility of synergistic reactions with the test lubricants in the vapor phase.

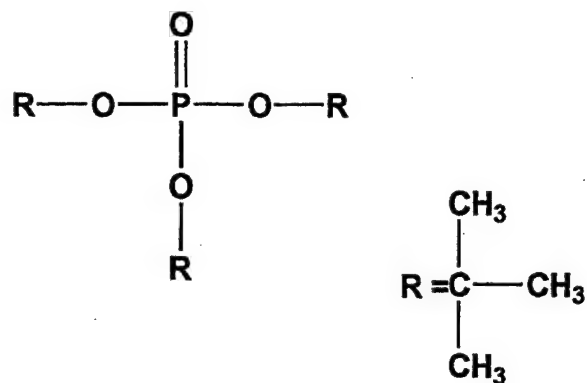


Figure 14. Molecular structure of tributyl phosphate (TBP).

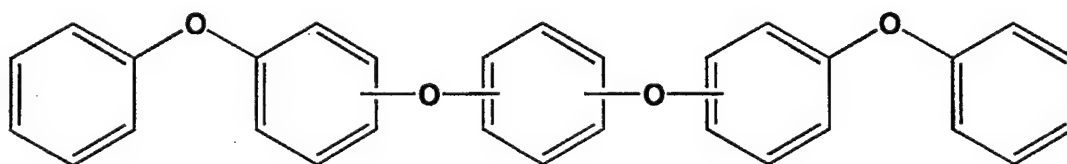


Figure 15. Molecular structure of a five-ring polyphenylether (5P4E).

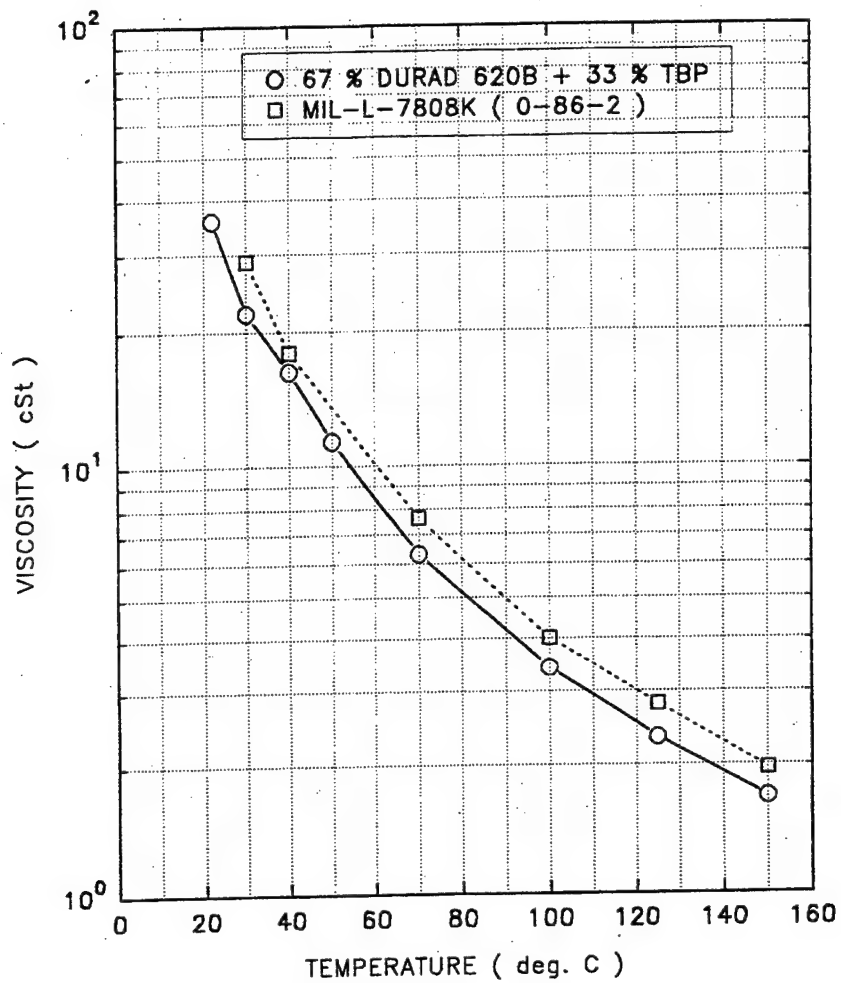


Figure 16. Temperature-viscosity graph of the TBPP blended with 33 percent TBP (TBPP/TBP) compared to a 4 cSt polyol ester aircraft engine lubricant.

Table 7. - Physical Properties of the Test Lubricants Compared to a 4 cSt Polyol Ester

	PAO/ TBPP	TBPP	TBPP/ TBP	X-1P	5P4E	Z	7808K
Viscosity @ 40°C (cSt)	6.21	119.2	16.32	210.0	278.5	17.09	17.98
Viscosity @ 100°C (cSt)	1.90	8.59	3.41	10.80	12.64	5.77	4.01
Flash Point (°C)	*	254	*	>270	288	*	>210
Specific Gravity (g/cm <sup>3</sup> )	0.83	1.12	1.02	1.45	1.16	1.73	0.96
Walther Coeff.							
A	9.95	11.19	9.99	11.52	11.44	6.26	9.16
B	4.02	4.36	3.97	4.47	4.43	2.47	3.63
Temperature @ 20,000 cSt (°C) <sup>+</sup>	-65	-8	-45	0	3	-83	-49

\* Undetermined

+ Extrapolated using Wather's equation

### 3.3 Bearing Temperature Tests

To determine the effect of temperature on the bearing performance, the bearing temperature was ramped from room temperature to 204°C, and then sequentially increased by increments of 56°C after each 15-minute period of operation. A lubricant flow rate of 2.5 ml/hr was used for all of the test lubricants. Shop air flowing at 283 l/hr was used to transport the vapor to the bearing surface. The bearing surfaces were pretreated with the lubricant vapor for a period of 20 minutes prior to test. A vapor delivery temperature of 330°C was used for the TBPP, TBPP/TBP, and Z tests. A lower vapor temperature of 300°C was used for the PAO/TBPP test; due to the lower vapor point and thermal and oxidative stability of the polyalphaolefin, fluid compared to the other test lubricants. For similar reasons, a higher vapor temperature of 370°C was used with the 5P4E and X-1P lubricants. Bearing friction and vibration were monitored during the test to measure the bearing performance. An accelerometer signal was used to automatically terminate the test if the vibration reached a level consistent with the initiation of a rolling contact fatigue spall.



Thermogravimetric analysis (TGA) was also performed on the test lubricants to help distinguish whether the bearings were lubricated by condensation or deposition. The TGA tests were conducted in an air environment with a temperature ramping rate of 10°C per minute. The temperature required for 10 percent weight loss was used as the boundary point for vapor phase condensation (VPC) lubrication. The temperature required for 90 percent weight loss was used as the boundary point for vapor phase deposition (VPD) lubrication. The region in between was defined as mixed-mode lubrication.

Friction traces for the test lubricants are shown in Figs. 17-22. Superimposed on each friction trace are the regions where VPC, mixed-mode, and VPD lubrication occurred, based on the TGA data presented in Table 8. In general, all of the lubricants were able to operate with VPC lubrication. A step increase in friction was encountered with most of the test lubricants, as the bearing entered mixed-mode lubrication. This step is very noticeable for the TBPP/TBP and the 5P4E fluids. All of the fluids demonstrated VPD lubrication, except for the Z perfluoroalkylether. As the bearing temperature increased in the deposition mode, the lubricants containing high levels of phosphorus performed the

best. Both the TBPP and TBPP/TBP reached very low levels of friction prior to thermal failure at 600°C. The X-1P cyclophosphazine demonstrated similar properties as the TBPP based phosphate esters, but did not fail from thermal failure in an 8-hour test at 650°C. The maximum operating temperature for the candidate lubricants are summarized in Table 9. A 15-minute period of sustained operation was used to determine the maximum operating temperature.

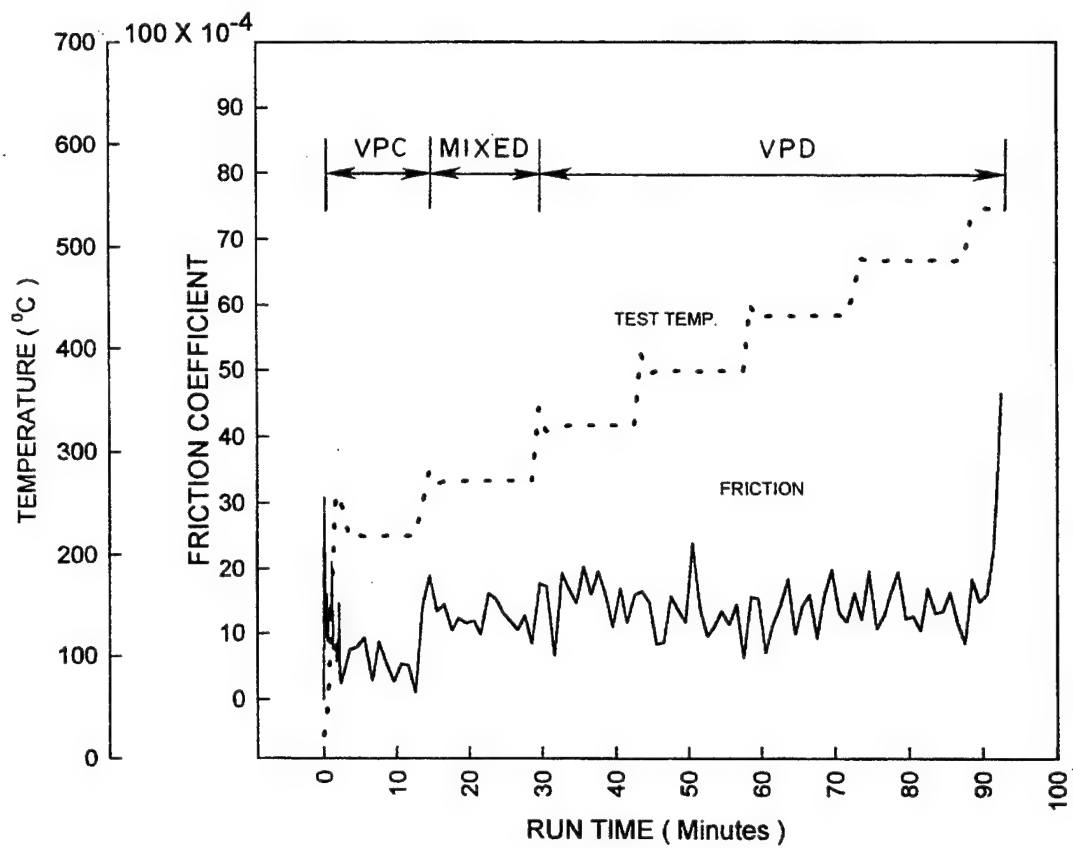


Figure 17. Bearing temperature test with the PAO fluid blended with 15 percent TBPP (PAO/TBPP).

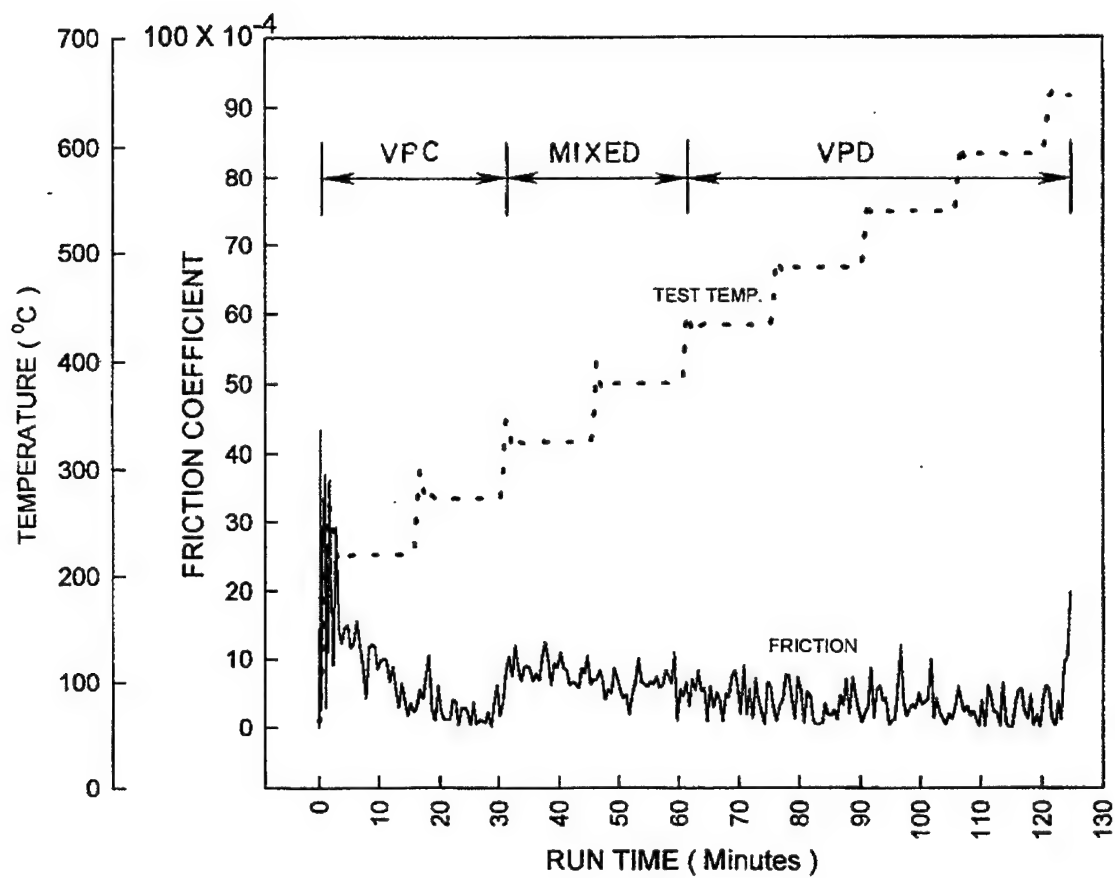


Figure 18. Bearing temperature test with the TBPP lubricant.

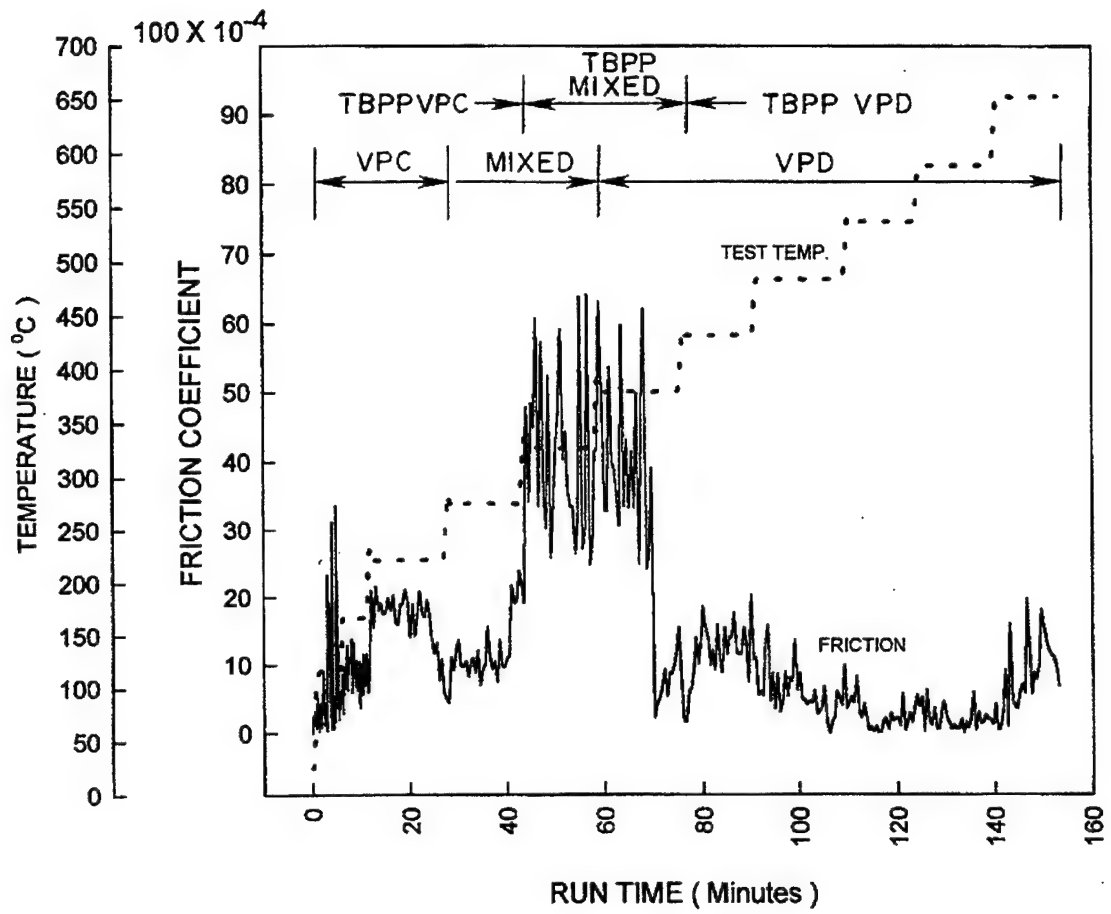


Figure 19. Bearing temperature test with the TBPP/TBP lubricant.

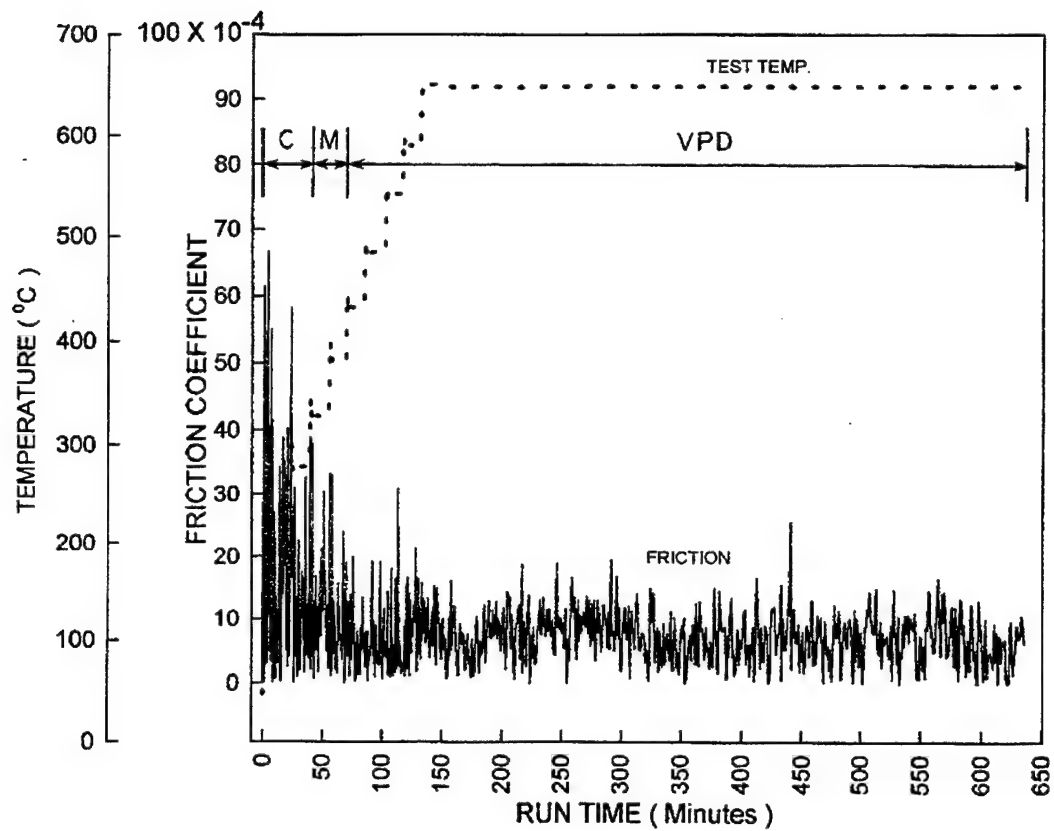


Figure 20. Bearing temperature test with the X-1P lubricant.

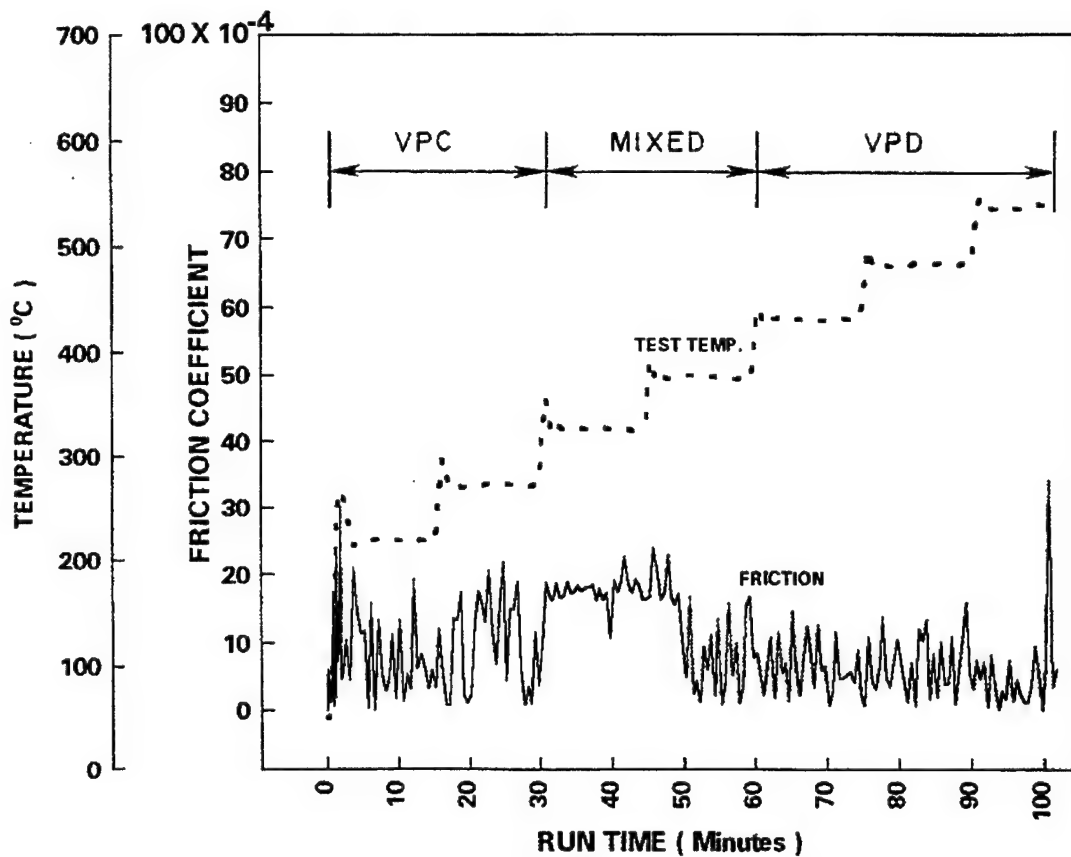


Figure 21. Bearing temperature test with the 5P4E lubricant.

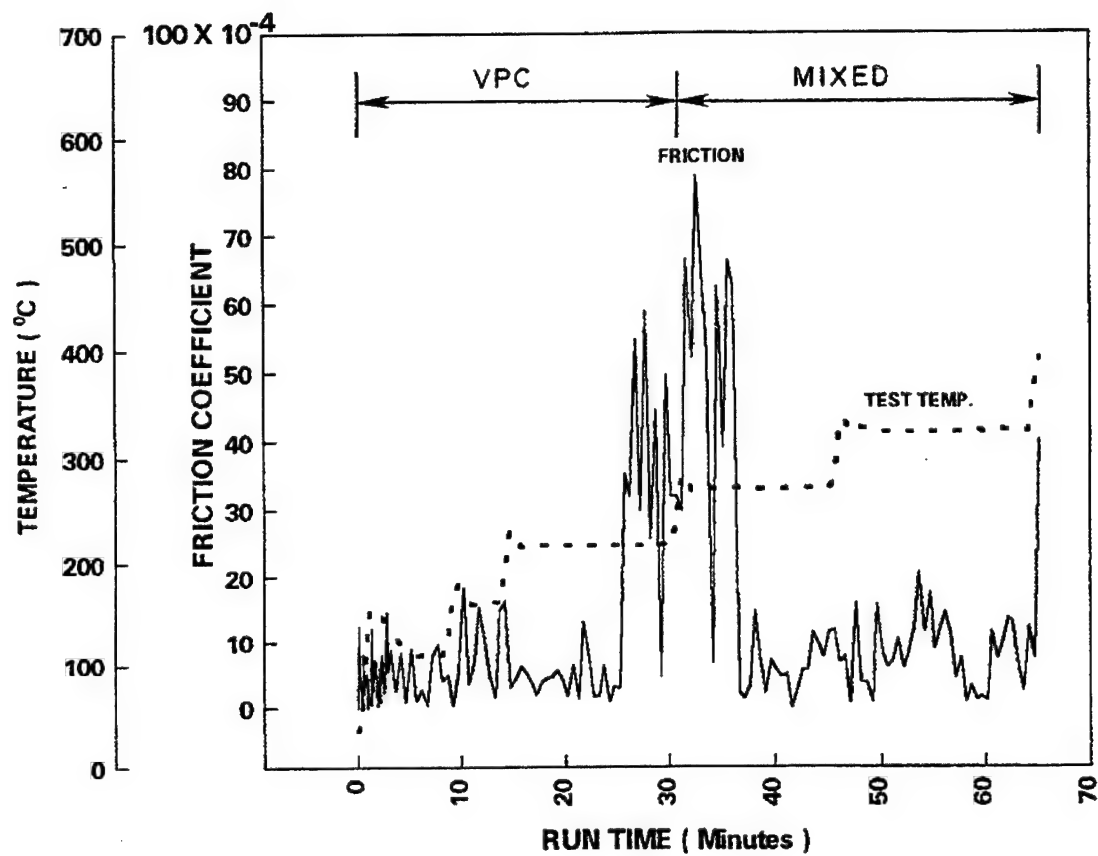


Figure 22. Bearing temperature test with the Z perfluoroalkylether.



Table 8. - Thermogravimetric Analysis Data

	PAO/ TBPP	TBPP	TBPP/ TBP	X-1P	5P4E	Z
90% wt (°C)	187	296	200	321	345	294
10% wt (°C)	266	363	355	377	410	386

Table 9. - Maximum Bearing Temperature for Sustained Operation

	PAO/ TBPP	TBPP	TBPP/ TBP	X-1P*	5P4E	Z
	538	594	538	650	482	260
Temperature	482	594	538	650	538	316
(°C)	482	594	538	650	538	

\* Temperature ramping stopped at 650°C. The actual maximum operating temperature for X-1P is higher than 650°C.

### 3.4 Vapor Temperature Tests

To determine the effect of vapor temperature on bearing performance, the air temperature exiting the vapor lubrication system was ramped from 316°C to 538°C in increments of 28°C. The bearing temperature was maintained at 371°C throughout the test. TBPP and X-1P were both evaluated under the same operating conditions for comparison.

Friction traces for the vapor-temperature tests are shown in Figs. 23 and 24. Both TBPP and X-1P provided low friction over the entire vapor temperature test range of 316°C to 538°C.

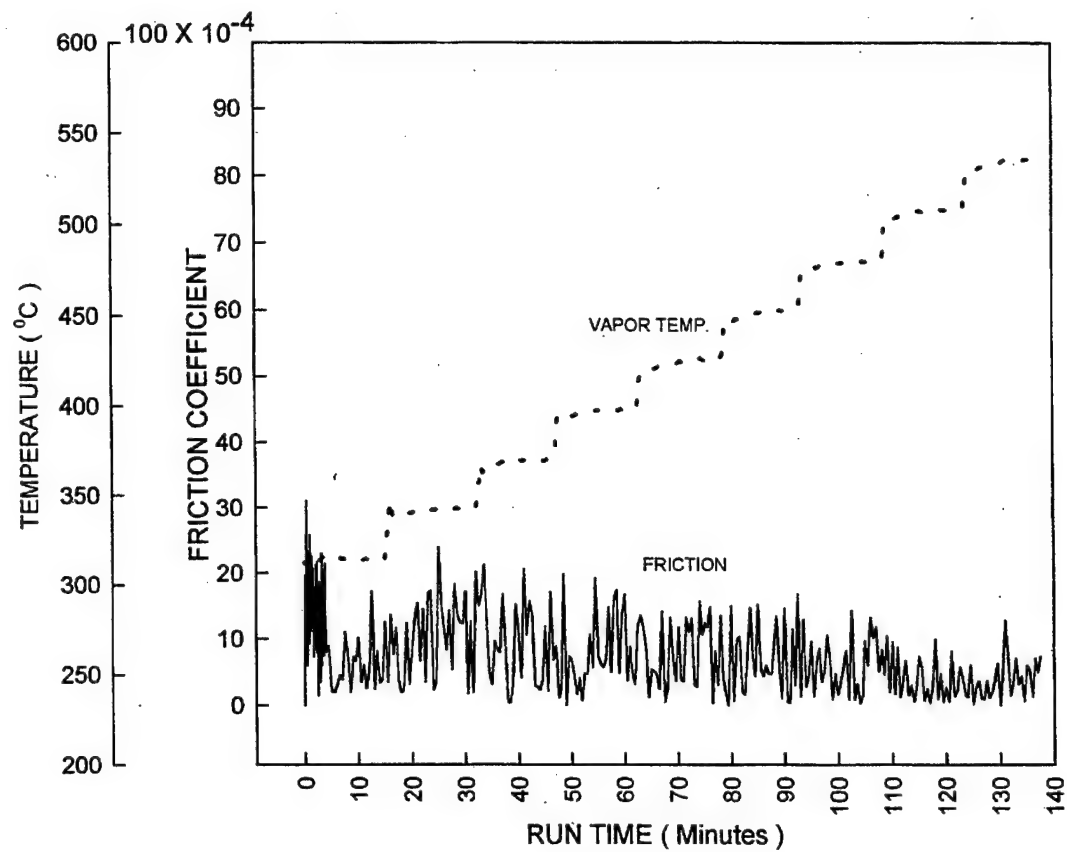


Figure 23. Vapor temperature test with a t-butylphenyl phosphate.

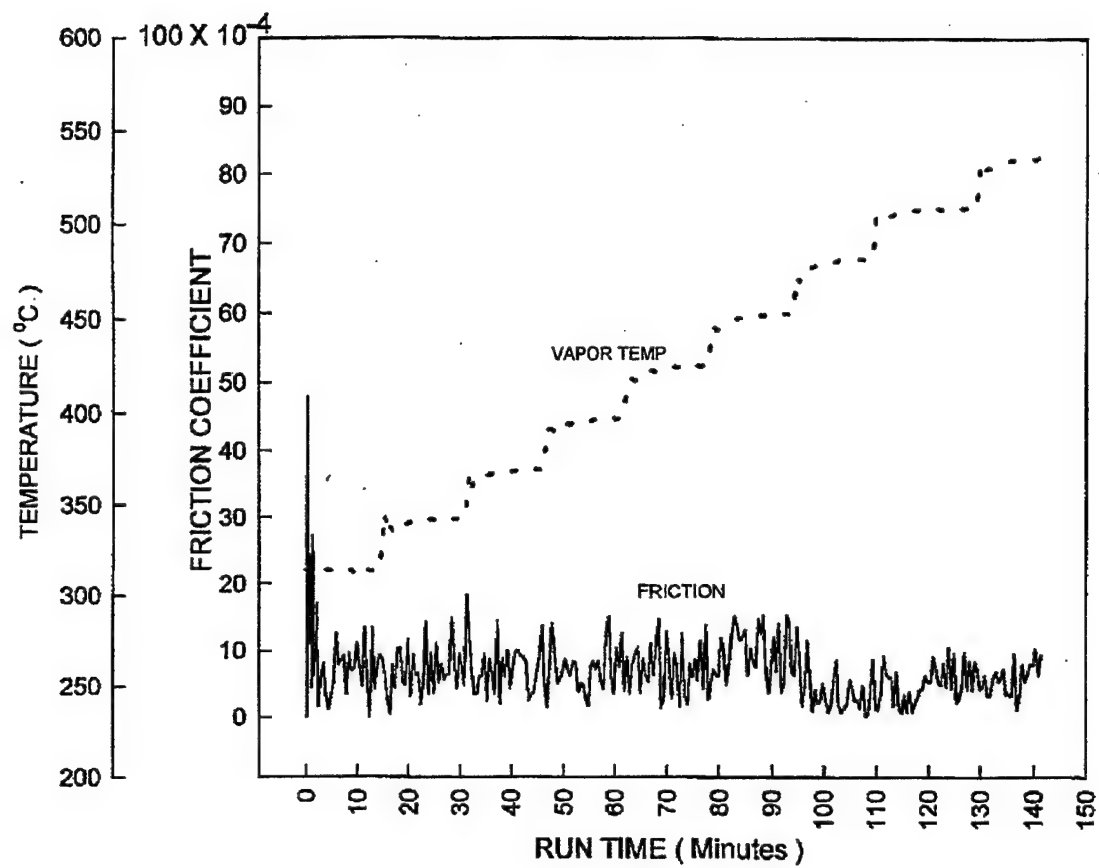


Figure 24. Vapor temperature test with the X-1P cyclophosphazine.

### 3.5 Solid Lubricant Coating Tests

To assess the response of vapor lubricated bearings under a cold start condition, the bearing temperature was ramped from room temperature to 380°C over a 2-minute period.

The vapor delivery system was preheated so that the air stream temperature was 330°C prior to test. TBPP lubricant delivered at 2.5 ml/hr was introduced into the vapor chamber, coinciding with the start-up of the bearing. The bearing was allowed to continue operation for an 8-hour period after reaching the steady state bearing temperature. Tests were conducted on bearing specimens, with and without a solid lubricant coating, for comparison. The solid lubricant coating was applied to the rod, races, and cage, but not to the rolling elements. Five cold-start tests were conducted on the same bearing track for the coated and uncoated specimens.

Results from the room temperature to 380°C ramping tests are presented in Figs. 25 and 26. The coating provided a significant reduction in friction, during the initial start up from room temperature. In subsequent restarts, the start-up friction was reasonably low for both coated and uncoated

specimens. The mean friction coefficient for specimens with the solid lubricant was  $3.8 \times 10^{-4}$ . In comparison, the mean friction coefficient for the uncoated specimens was  $8 \times 10^{-4}$ . Optical micrographs of the bearing tracks for the rod specimens, with and without the coating, are shown in Figs. 27 and 28, respectively. The specimen with the coating shows significantly less surface damage, than the specimen without the coating. EDS analysis of the coated specimen indicates the solid lubricated coating was removed during test. Fig. 29 presents a Scanning Electron Microscopy (SEM) image of one of the surface pits formed on the rod without the solid lubricant coating. Surface cracks around the pit suggests that the pit propagates, at least in part, by surface delamination.

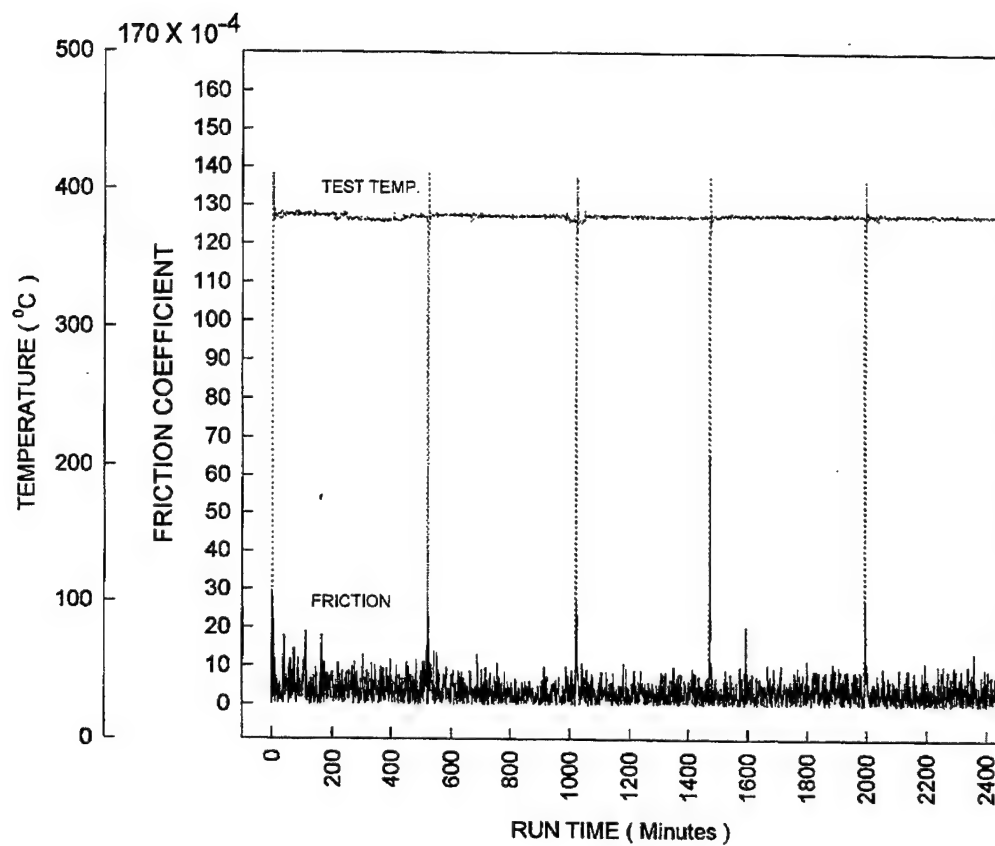


Figure 25. Five cold-start tests with a solid lubricant applied to the bearing samples. *t*-Butylphenyl phosphate was used as the vapor phase lubricant.

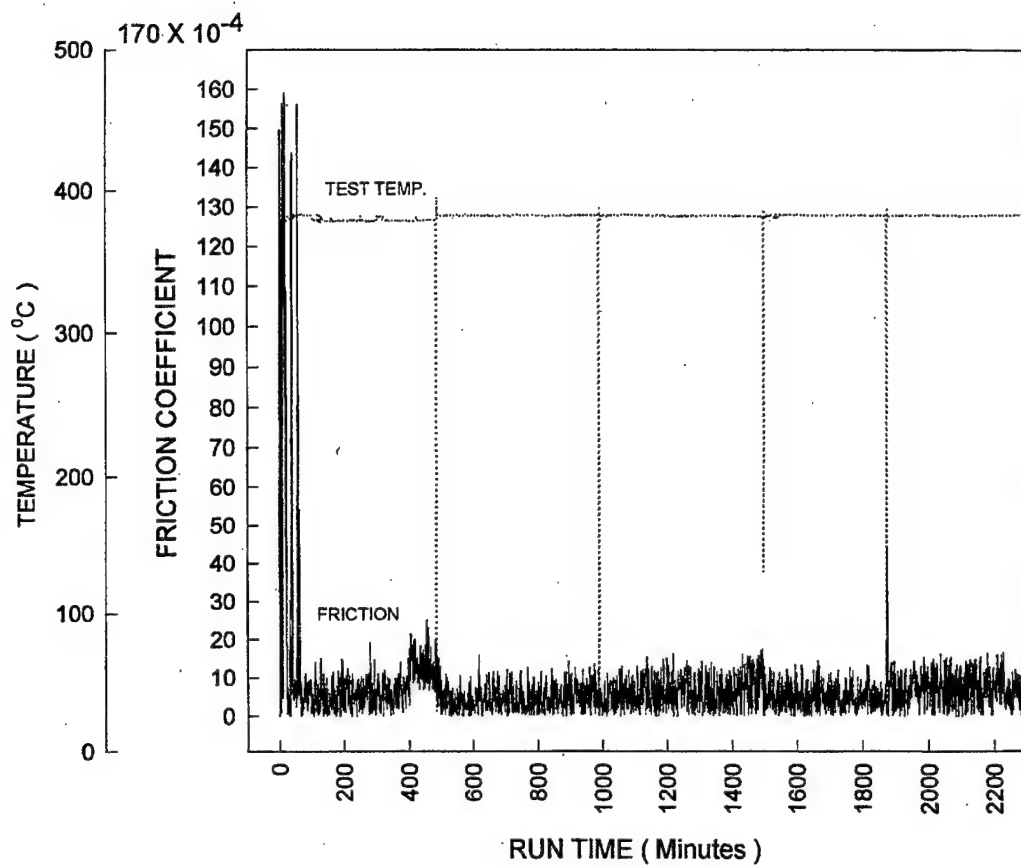


Figure 26. Five cold-start tests without the solid lubricant coating. *t*-Butylphenyl phosphate was used as the vapor phase lubricant.



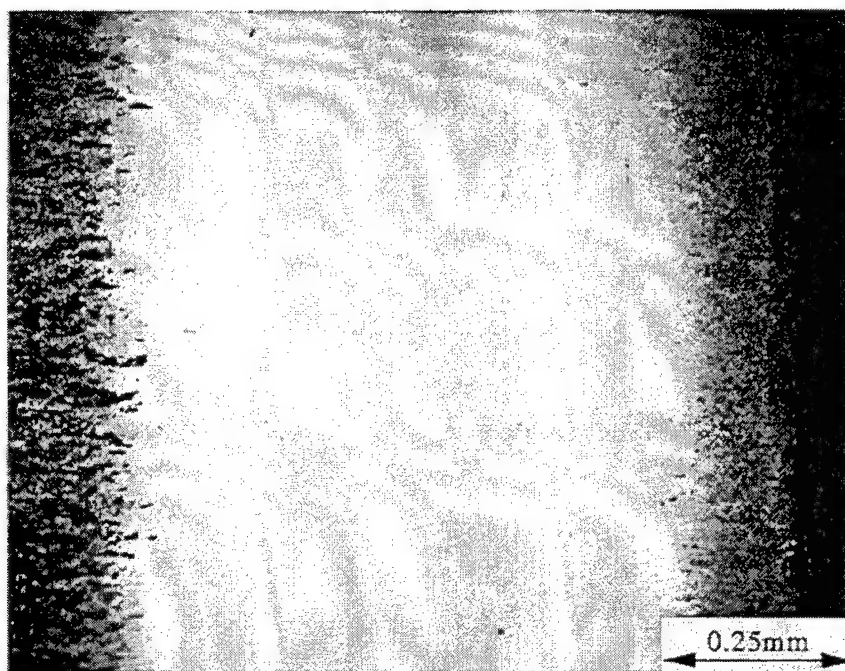


Figure 27. Optical micrograph of the bearing track formed after the cold-start tests with the initial application of a solid lubricant coating.

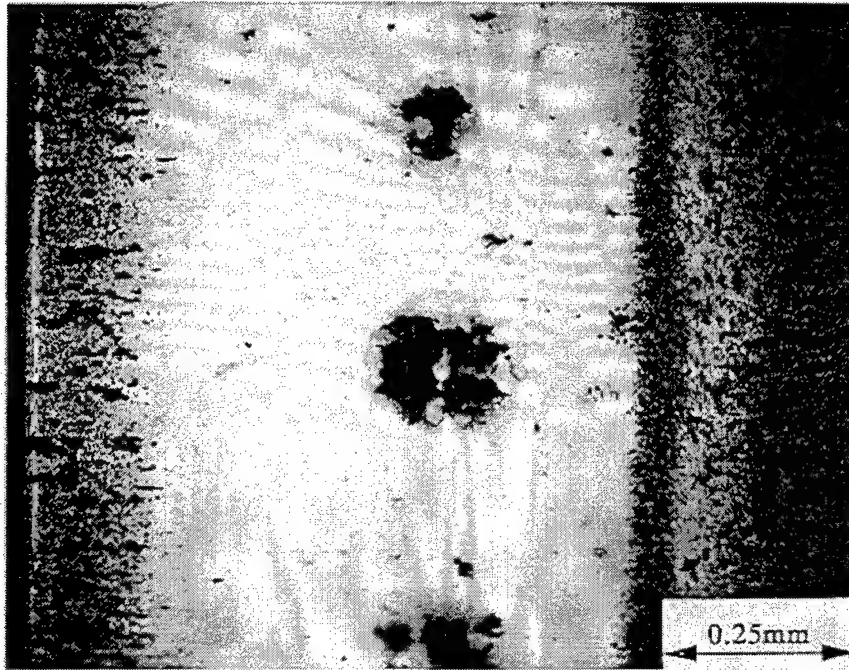


Figure 28. Optical micrograph of the bearing tract formed after the cold-start tests without the initial application of a solid lubricant coating.

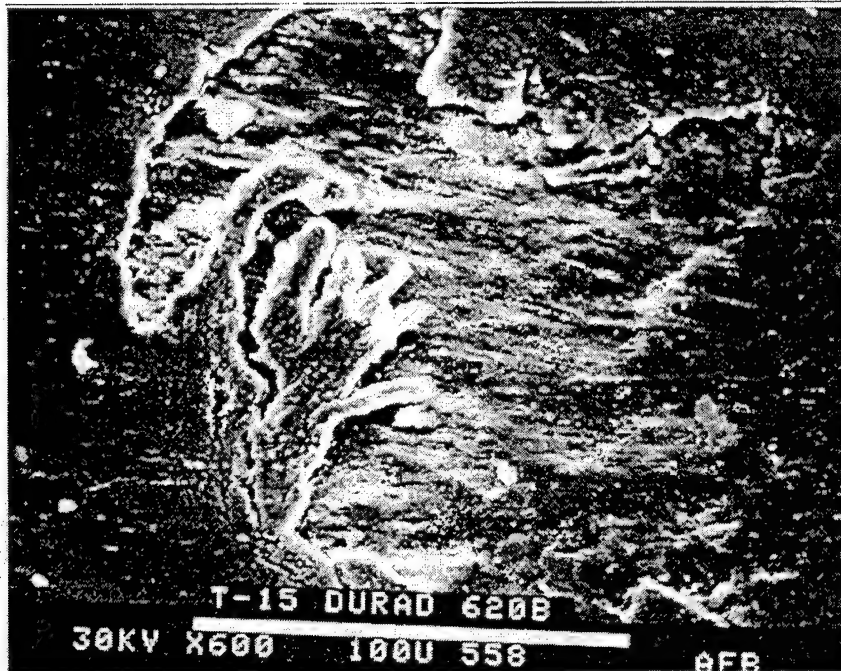


Figure 29. Scanning electron microscopy (SEM) image of a surface pit formed on the uncoated rod during the cold-start tests.

### 3.6 Lubricant Concentration Tests

Concentration tests were conducted with the TBPP fluid at bearing temperatures of 371°C and 500°C. The lubricant vapor temperatures were maintained at 330°C and 450°C, respectively. The vapor concentration was adjusted by varying the lubricant flow rate with a laboratory syringe pump. The maximum flow rate of the lubricant in a 20-hour test, was limited to 3.3 ml/hr, due to size limitations of the syringe. The flow of air, measured at room temperature, was regulated at 283 l/hr. Using a molecular weight of 438 for di(p-t butylphenyl)phenyl phosphate, a typical molecule in the TBPP fluid, the mole percent value can be obtained by multiplying the lubricant flow rate in ml/hr by 0.022.

Friction results for the concentration tests are shown in Fig. 30. The lowest friction for the bearings operating at 371°C and 500°C occurred at lubricant flow rates near 1.2 ml/hr and 2.8 ml/hr, corresponding to mole percentage values of 0.026 and 0.062, respectively.

Wear results for the concentration tests are shown in Fig. 31. The minimum value for the bearing wear rate at 371°C occurs near 1.5 ml/hr, corresponding to a concentration

of 0.033 mole percent. The minimum wear rate at the bearing temperature of 500°C was not obtained in the 20-hour test, due to sample size limitations with the laboratory syringe pump. However, by following the trend in the data, it appears the minimum will occur in the vicinity of 4 ml/hr or 0.09 mole percent.

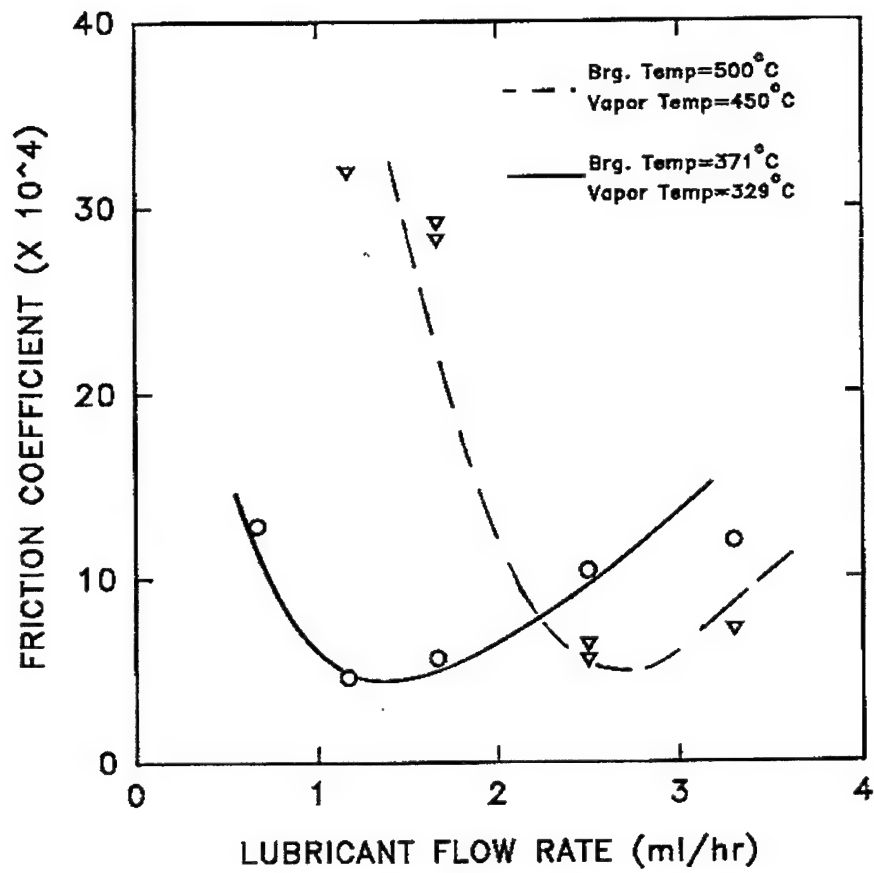


Figure 30. The effect of lubricant flow rate on the bearing friction coefficient.

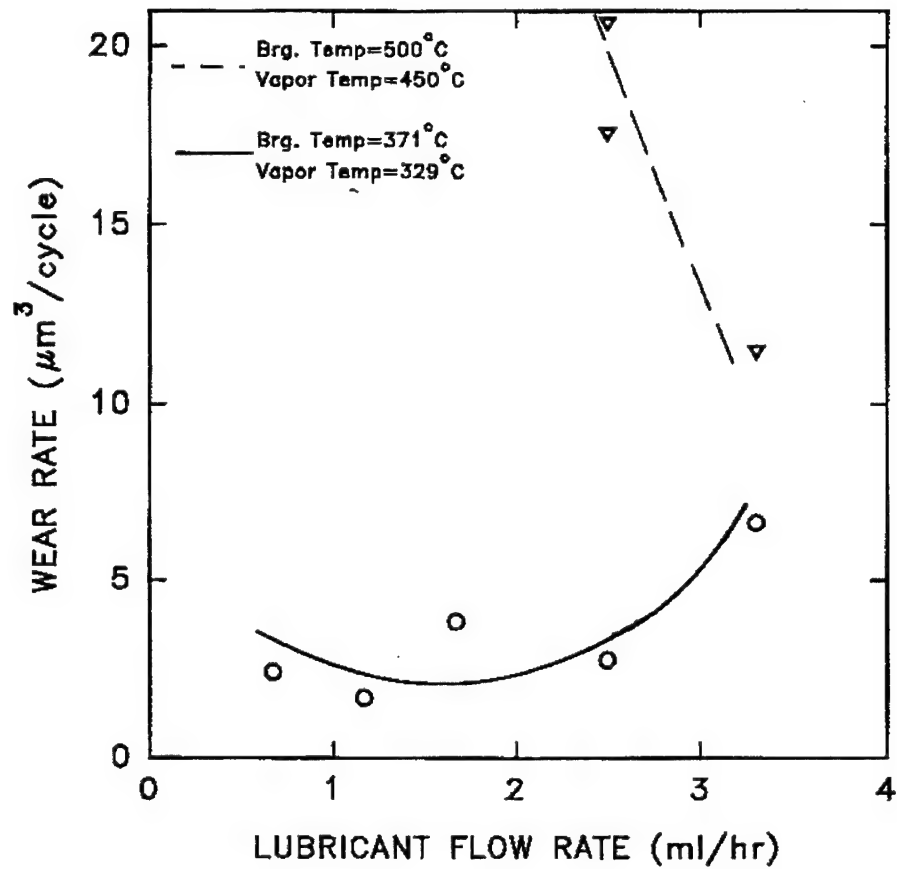


Figure 31. The effect of lubricant flow rate on the bearing wear rate.

### 3.7 Discussion

All of the test lubricants performed well in the condensation mode, demonstrating behavior consistent with liquid lubrication. As the bearing temperature increased, a step increase in the friction coefficient was encountered with several lubricants at temperatures consistent with the onset of significant lubricant volatilization. This step is particularly high for the TBPP/TBP and 5P4E lubricants. All of the lubricants were able to transition into the vapor deposition mode, except the Z perfluoroalkylether. This is attributed to the difference in decomposition products of fluorocarbon lubricants.

The friction coefficient, of the TBPP and TBPP/TBP lubricants, continued to decrease with increasing bearing temperature, in the deposition mode. The lowest friction was reached, just prior to thermal failure at 600°C. The X-1P demonstrated similar friction characteristics but did not fail from thermal failure in an 8-hour test at 650°C. The improved performance of the phosphorus lubricants compared to the 5P4E polyphenylether and Z perfluoroalkylether emphasizes



the importance of phosphorus in VPD lubrication. Additionally, comparison of the performance of phosphorus lubricants to the condensation performance of several lubricants, reinforces that these are viable high temperature lubricants, which operate over a very broad temperature range as VPC and VPD lubricants.

Vapor delivery temperatures, in the range of 318°C to 538°C, did not appear to be a critical factor in the deposition performance for the TBPP and X-1P lubricants. Recent research performed by Wright (28) has shown that TBPP vapors primarily consist of the parent molecules and phenol by-products, in the temperature range of 300°C to 600°C. Above 600°C, severe thermal degradation of the TBPP molecule occurs. This suggests that TBPP can be transported to bearing surfaces in a hot air stream at temperatures up to 600°C.

The solid lubricant coating was beneficial in reducing the initial friction under the cold-start conditions. In subsequent restarts, the start-up friction was relatively low for both coated and uncoated specimens. Post-test examination of the rod using EDS, indicates the solid lubricant was removed from the bearing track during test. The

lower friction in subsequent restarts for the coated, as well as uncoated rods, is attributed to a vapor deposition film left from the previous test. The lower mean friction for the coated samples, as compared to the uncoated samples, is attributed to less surface damage on the specimens with the solid lubricant.

Post-test examination of the uncoated rod, used in the cold-start test, showed that pitting occurred in the bearing track. Surface pitting frequently occurs with the TBPP vapor lubricant in regions of high tensile and high shear stress, high bearing temperatures, and/or high concentrations of lubricant. SEM analyses of a pit, formed on the uncoated rod, indicate the pit was propagating by surface delamination. The appearance of surface pits, generated with vapor phase lubrication, is similar to corrosion pits commonly found on aircraft engine bearings upon visual inspection. It is thought that the high shear forces, generated during the initial cold-start, precipitated micro-surface damage, which propagated into the surface pits shown in Fig. 28. In Chapter 4, the bearing track for the uncoated specimen is cross sectioned and further examined, using Auger electron spectroscopy.

Lubricant concentration is a critical parameter in optimizing the performance of a vapor lubrication system, with relatively small changes in lubricant supply having a significant impact on friction and wear. Additionally, the data indicate that the optimum concentration is affected by the bearing temperature. Klaus and Duda proposed that the lubricant concentration should be set to match the disappearance of the lubricant on the bearing surface (20). This suggests that the optimum concentration will be system specific and can be affected by parameters such as surface speed, percent sliding, and bearing temperature. The optimum concentrations found in the rolling contact tester, 0.03 mole percent and 0.08 mole percent for bearings operating at 371°C and 500°C, respectively; are significantly less than the 0.5 mole percent value determined by Klaus and Duda in the 4-ball tester at 700°C.

Maintaining good low temperature-viscosity properties enables a vapor lubrication system to rapidly supply the lubricant, under cold-start conditions. Of the lubricants tested, the TBPP/TBP offers the best low end viscosity, while maintaining bearing performance at elevated temperatures. However, as previously mentioned in the discussion, the

TBPP/TBP lubricant experiences a step in friction at intermediate temperatures.

## CHAPTER 4

### SURFACE ANALYSES

The following techniques were used to investigate the deposition film formed on specimens from Chapters 2 and 3:

- Fourier Transform Infrared Microscopy ( $\mu$ -FTIR)
- Raman Spectroscopy
- Auger Electron Spectroscopy (AES)
- Scanning Electron Microscopy (SEM)
- Energy Dispersive Spectroscopy (EDS)

The objective of the analyses was to further the basic understanding of the lubrication and failure mechanisms of high temperature rolling contacts, lubricated from the vapor phase.

#### 4.1 Experimental Procedure

Samples selected for surface analyses are listed in Table 10. The samples were generated in tests previously described in Chapters 2 and 3.

The infrared spectra were collected with an IRPLAN infrared microscope, integrated to a Perkin Elmer System 2000 FTIR spectrometer. A 15X reflecting objective was employed to focus the infrared radiation on the test samples and to collect the reflected radiation from the sample. A 100  $\mu$  spot size was used to generate the infrared spectra.

The Raman spectra were collected with a Reinshaw System 2000 Raman microprobe, using a HeNe laser (632.8 nm) as the excitation source. An Olympus 50X (0.80 N.A.) objective was employed to focus the laser onto the sample and collect the resulting scattered radiation. The use of this objective produced a sampling area, on the order of 2  $\mu$  in diameter. Power at the sample did not exceed 10 milliwatts and an integration time of 400 seconds per spectral element was employed.

The Auger spectra were collected with a Varian 981-2707 spectrometer. An Ar ion gun was used to sputter etch the surface for depth profiling. The approximate sputter rate was 8 nm/min. A 5 KeV electron beam was used to excite the sample surface for detection of the Auger electrons. A spot size of approximately 50  $\mu$  was used to generate the Auger spectra.

To gain further insight into the surface damage associated with the TBPP vapor lubrication, the rod specimen corresponding to Sample Set 1 was sectioned and polished to reveal the subsurface region of the bearing track. After sectioning, the sample was further analyzed, using a Lrica 360 FE scanning electron microscope. The microscope was equipped with an atmospheric thin window for EDS analysis.

Table 10 - Samples Selected for Surface Analyses

Sample Set	1	2	3	4	5	6
<u>Materials</u>						
Lubricant	TBPP	TBPP	PAO/TBPP	5P4E	X-1P	TBPP
Rod	T15	T15	T15	T15	T15	T15
Cage	4340	4340	4340	4340	4340	4340
Ball	T15	Si <sub>3</sub> N <sub>4</sub>	Si <sub>3</sub> N <sub>4</sub>	Si <sub>3</sub> N <sub>4</sub>	Si <sub>3</sub> N <sub>4</sub>	T15
<u>Test Condition</u>						
Bearing Temp(°C)	370	25-650	25-482	25-538	25-650	370
Lubricant Rate (ml/hr)	2.5	2.5	2.5	2.5	2.5	2.5
Test Duration(hr)	96	2.1	1.5	1.8	10.7	40
<u>Analysis Technique</u>						
μ-FTIR	Yes	Yes	Yes	Yes	Yes	No
Raman	Yes	Yes	Yes	Yes	Yes	No
AES	Yes	No	No	No	No	Yes
SEM	No	No	No	No	No	Yes
EDS	No	No	No	No	No	Yes
Ref. Figs.	9,10	18	17	21	20	26,28



## 4.2 $\mu$ -FTIR Results

The infrared spectrum of a TBPP film, deposited just outside the bearing track of Sample Set 1, is shown in Figs. 32 and 33. The locations of the infrared absorption bands at 2960, 2930, and 2850  $\text{cm}^{-1}$  in Fig. 32, correlate with the  $\text{CH}_2$  and  $\text{CH}_3$  stretching modes in the n-alkane structure (55). The absorption at 2337  $\text{cm}^{-1}$  correlates with the P-H stretch in the phosphite ion,  $\text{HPO}_3^{2-}$ , and the hypophosphite ion,  $\text{H}_2\text{PO}_2^-$  (56). The band at 1745  $\text{cm}^{-1}$  is consistent with the location expected for C=O (57). The band at 1545  $\text{cm}^{-1}$  has not been identified. The prominent absorption band at 1060  $\text{cm}^{-1}$  is consistent with the P-O stretching bond, found in phosphate structures (56,58). The band at 930  $\text{cm}^{-1}$  correlates with the P-O-P absorption band (56).

An infrared spectrum of iron phosphate (59), produced from reactions of phosphoric acid with an iron surface, is shown in Fig. 34. There are two peaks correlating to the P-O and P-O-P stretching modes at 1135 and 940  $\text{cm}^{-1}$ . The locations of these absorption bands are different than the

locations associated with the P-O stretch and the P-O-P bands in the vapor deposition film.

The infrared spectrum of the TBPP deposition film inside the bearing track for the rod specimen in Sample Set 1, is shown in Fig. 35. The spectrum does not show any prominent absorption bands. There are two plausible explanations:

1. Lack of sufficient film to absorb any significant amount of infrared radiation, or;
2. The bulk of the material present does not have any significant dipole moment (i.e., amorphous carbon). A dipole moment is required for infrared absorption to occur(60).

Analyses using Auger and Raman spectroscopy indicates that both 1 and 2 are factors.

The infrared spectrum of the TBPP lubricant, prior to test, is shown in Fig. 36. In comparing the lubricant spectrum to the deposition film spectra, shown in Figs. 32 and 33, it is clear that significant chemical reactions have occurred between the lubricant and the T15 material.

The infrared spectrum of the film formed on a T15 ball, from Sample Set 1, is shown in Fig. 37. The ball shows a strong band correlating with a phosphate structure. The bands associated with the n-alkanes are not present and the band associated with P-H bond is substantially reduced.

The infrared spectrum of the film formed on the T15 rod from the Sample Set 2 is shown in Fig. 38. The absorption bands associated with the n-alkanes are substantially reduced, the P-H band is substantially larger, and the prominent band associated with the P-O stretch, now occurs at  $970\text{ cm}^{-1}$  rather than at  $1060\text{ cm}^{-1}$ . An increase in P-O-P constituents would shift this band lower (61, 56).

The infrared spectrum of the film formed, on a  $\text{Si}_3\text{N}_4$  ball from Sample Set 2, is shown in Fig. 39. The ceramic surface does not generate a phosphate/phosphite film.

Infrared spectra of films, generated outside the bearing track for the PAO/TBPP, X-1P, and 5P4E lubricants, are shown in Figs. 40-42. The spectra were obtained from the rod specimens generated in Sample Sets 3 through 5, respectively. The PAO/TBPP and X-1P lubricants generate a phosphate/phosphite structure, similar to the TBPP when the lubricants are delivered in the vapor phase. This occurred

even though the X-1P lubricant molecule, Fig. 3, is substantially different than the TBPP molecule shown in Fig. 2. However, both molecules contain phenoxy groups attached to a pentavalent phosphorus ion. The film deposited by the 5P4E lubricant indicates a small quantity of n-alkanes, P-H, and other unidentified bonds. The presence of the n-alkanes and apparent phosphorus is attributed to residual effluent from previous lubricants. This occurred even though the test head was ultrasonically cleaned and baked, prior to testing each lubricant. Even though phosphorus is present in the 5P4E deposition film, there is not a strong presence of the phosphate/phosphite mixture. The background noise in the 5P4E spectrum, also, suggests the deposition film is thinner than obtained with the phosphorus containing lubricants.

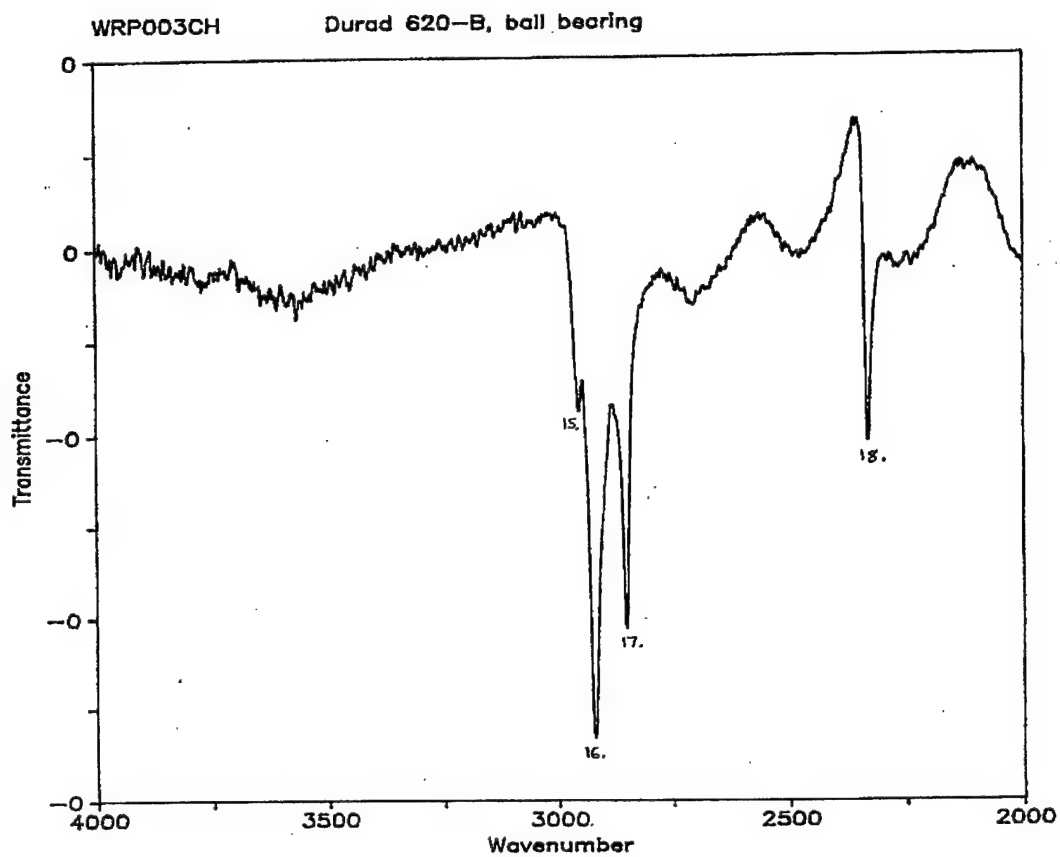


Figure 32. Fourier transform infrared (FTIR) spectrum of a rod specimen lubricated with TBPP vapor outside of the wear track, 4000  $\text{cm}^{-1}$  to 2000  $\text{cm}^{-1}$ .

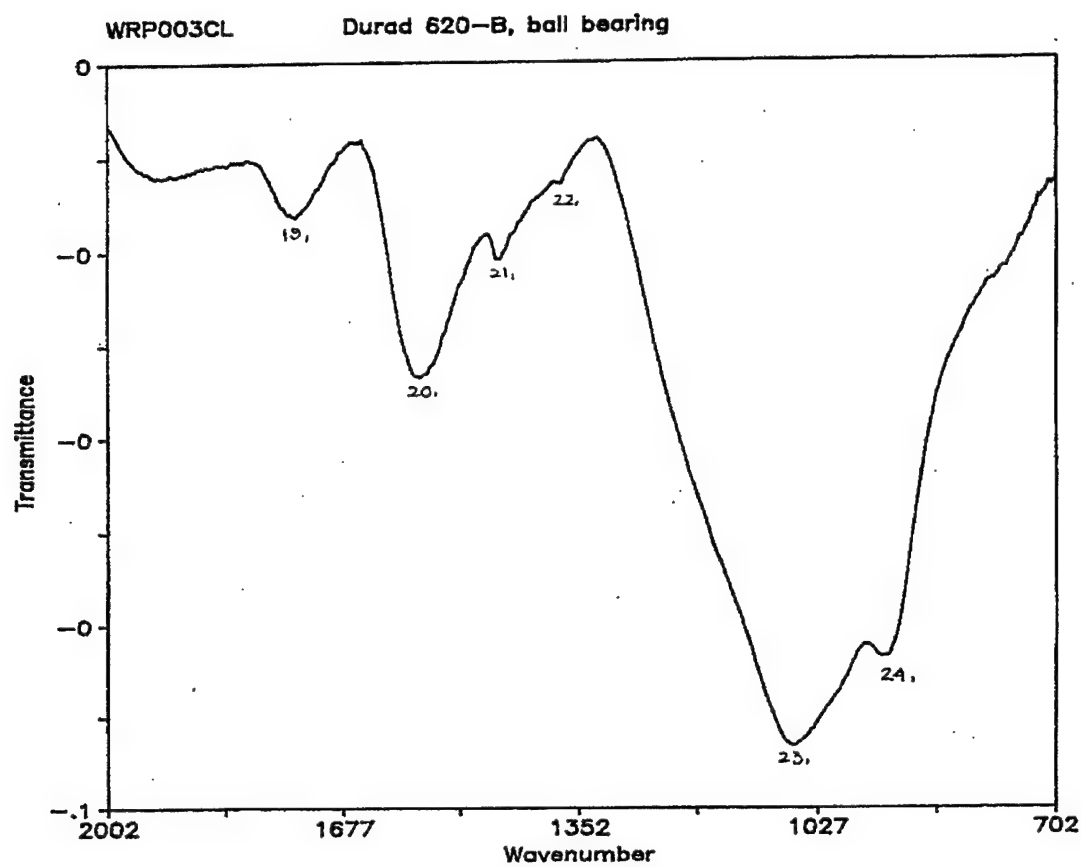


Figure 33. FTIR spectrum of a rod specimen lubricated with TBPP vapor outside of the bearing track,  $2000\text{cm}^{-1}$  to  $700\text{cm}^{-1}$ .

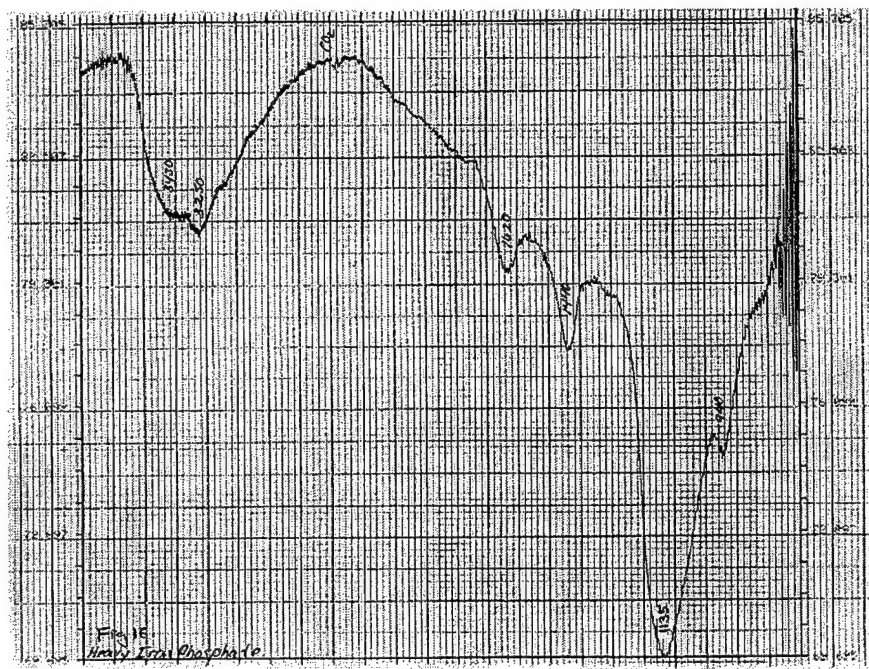


Figure 34. FTIR spectrum of iron phosphate produced by the reaction of phosphoric acid on an iron surface.

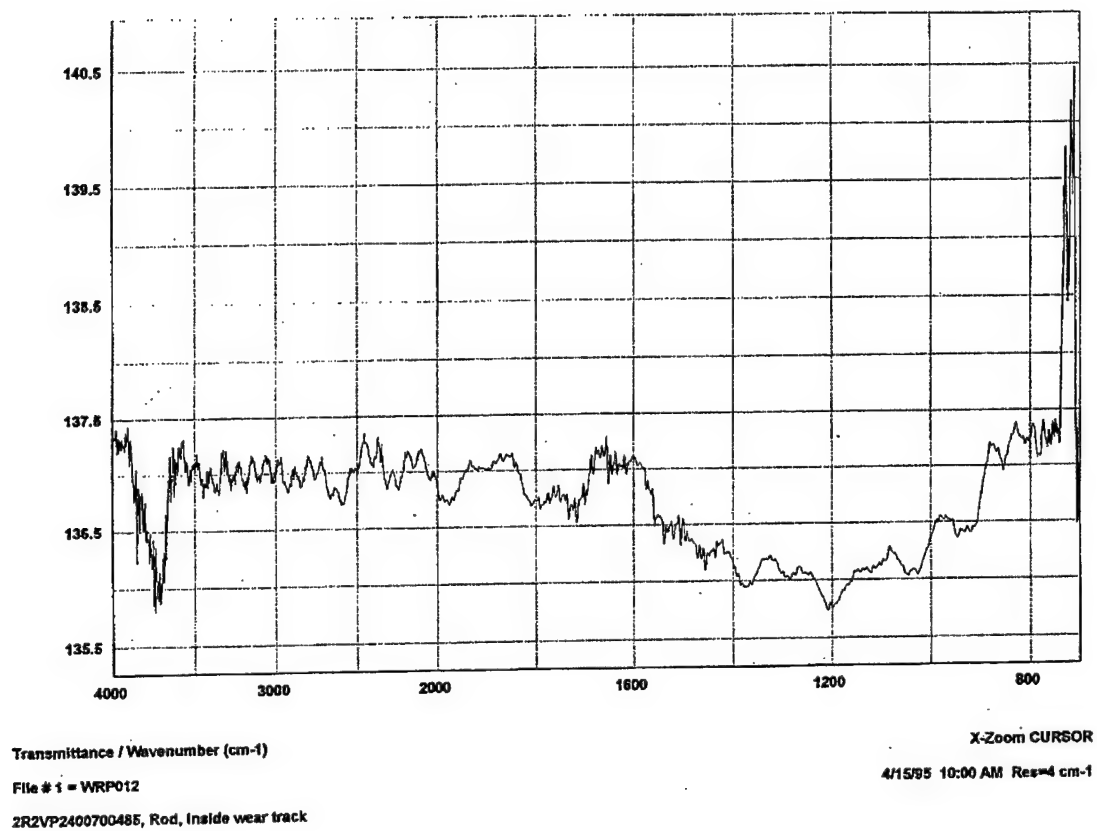


Figure 35. FTIR spectrum of a rod specimen lubricated with TBPP vapor inside the wear track.



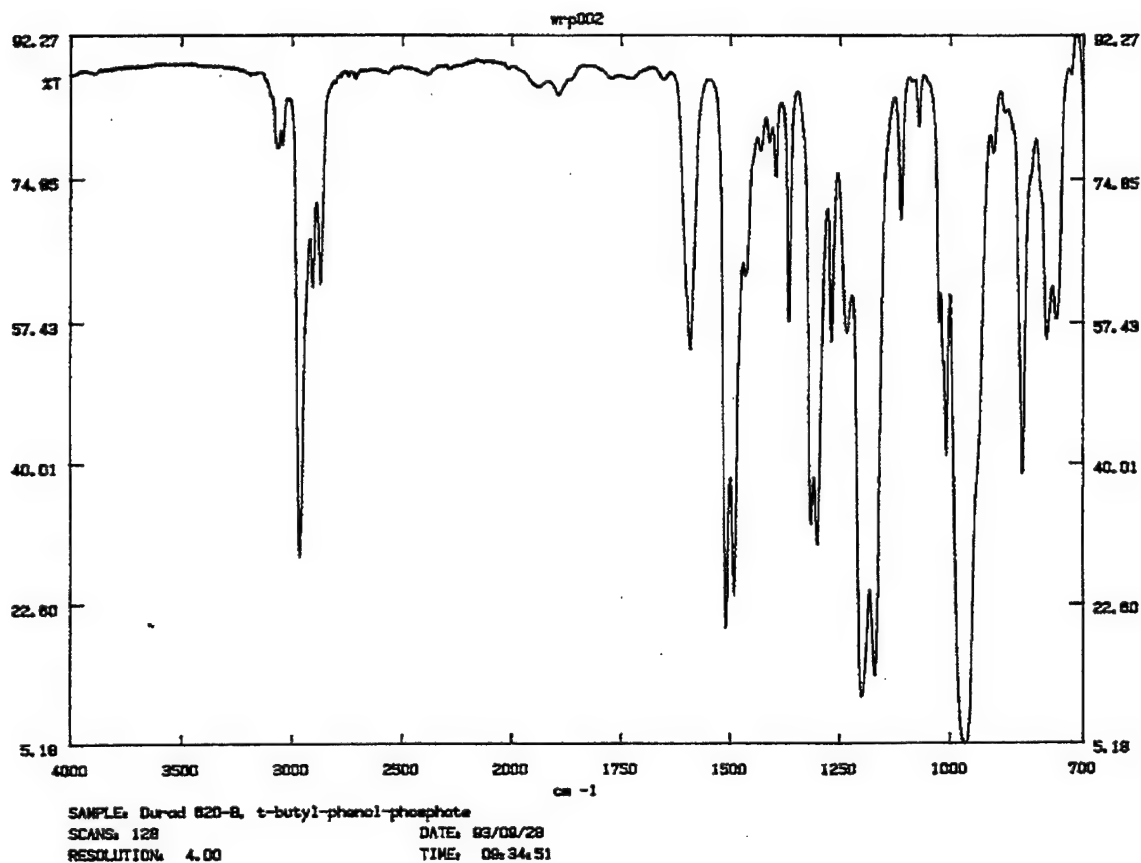
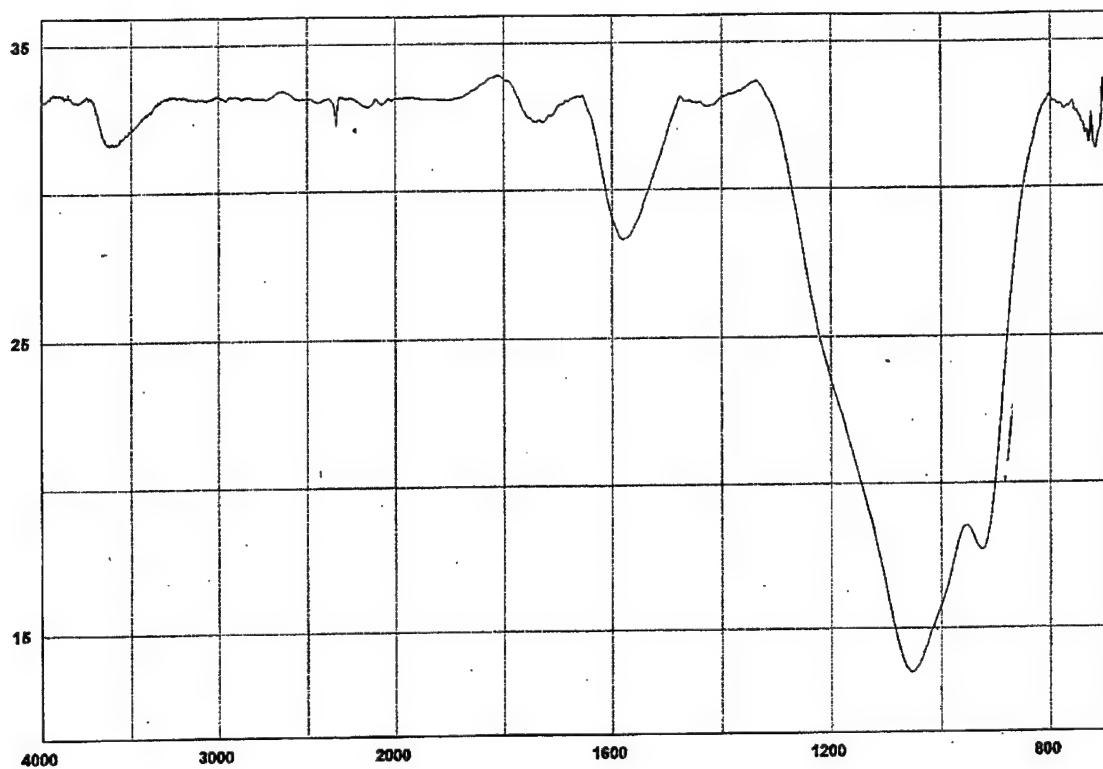


Figure 36. FTIR spectrum of the TBPP lubricant prior to the test.



Transmittance / Wavenumber (cm-1)

File # 1 = WRP014

2R2VP2400700485, ball

X-Zoom CURSOR

4/16/95 1:49 PM Res=4 cm-1

Figure 37. FTIR spectrum of a T15 ball lubricated with TBPP vapor.

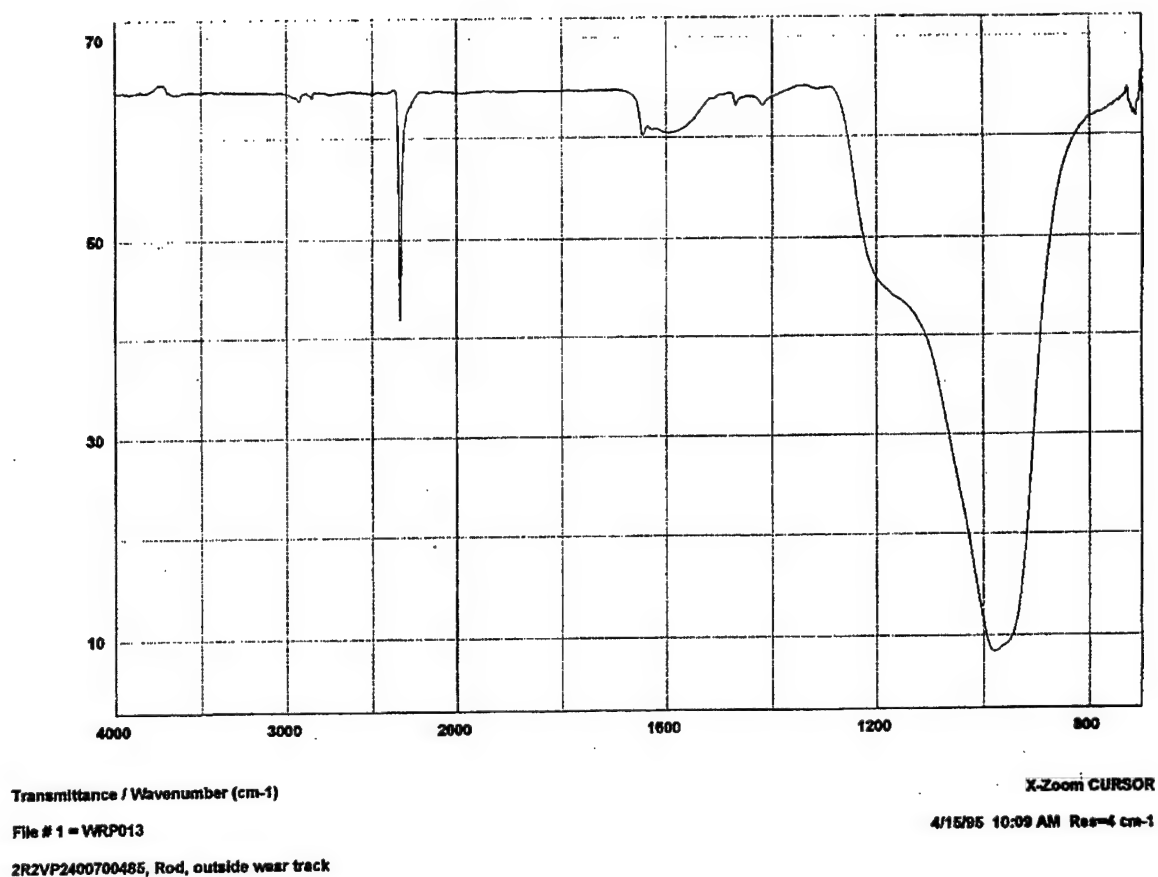
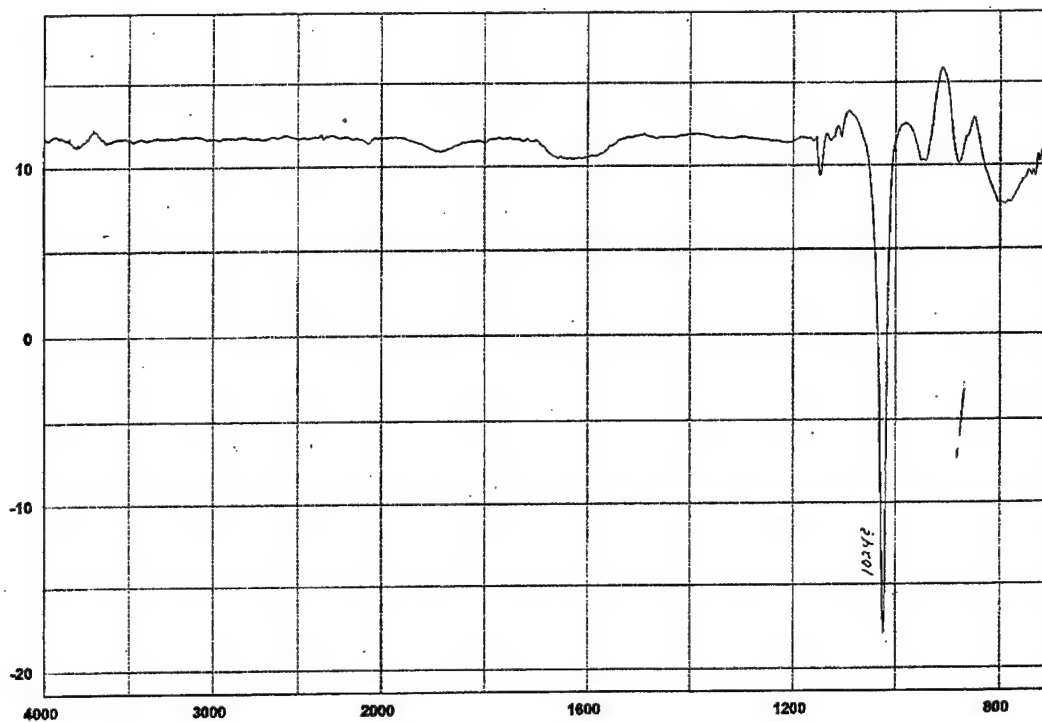


Figure 38. FTIR spectrum of rod after the bearing temperature test with TBPP vapor.



Transmittance / Wavenumber (cm-1)

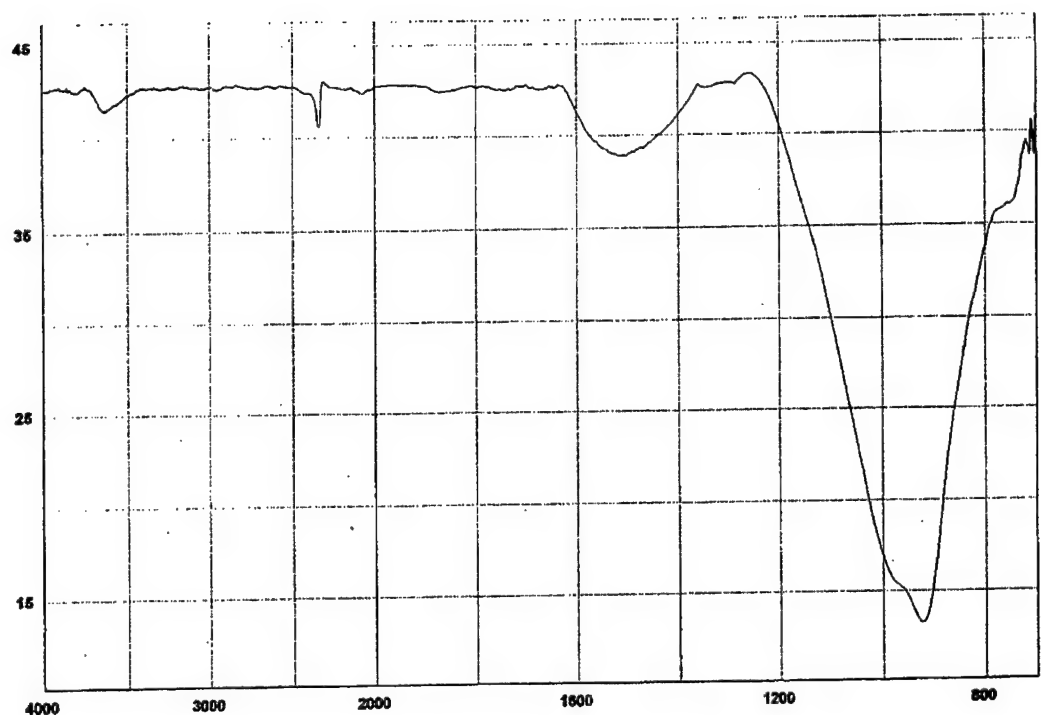
File # 1 = WRPC018

2R2VP22000VT530, ball

X-Zoom CURSOR

4/16/95 2:33 PM Res=4 cm-1

Figure 39. FTIR spectrum of a  $\text{Si}_3\text{N}_4$  ball lubricated with TBPP vapor.



Transmittance / Wavenumber (cm-1)

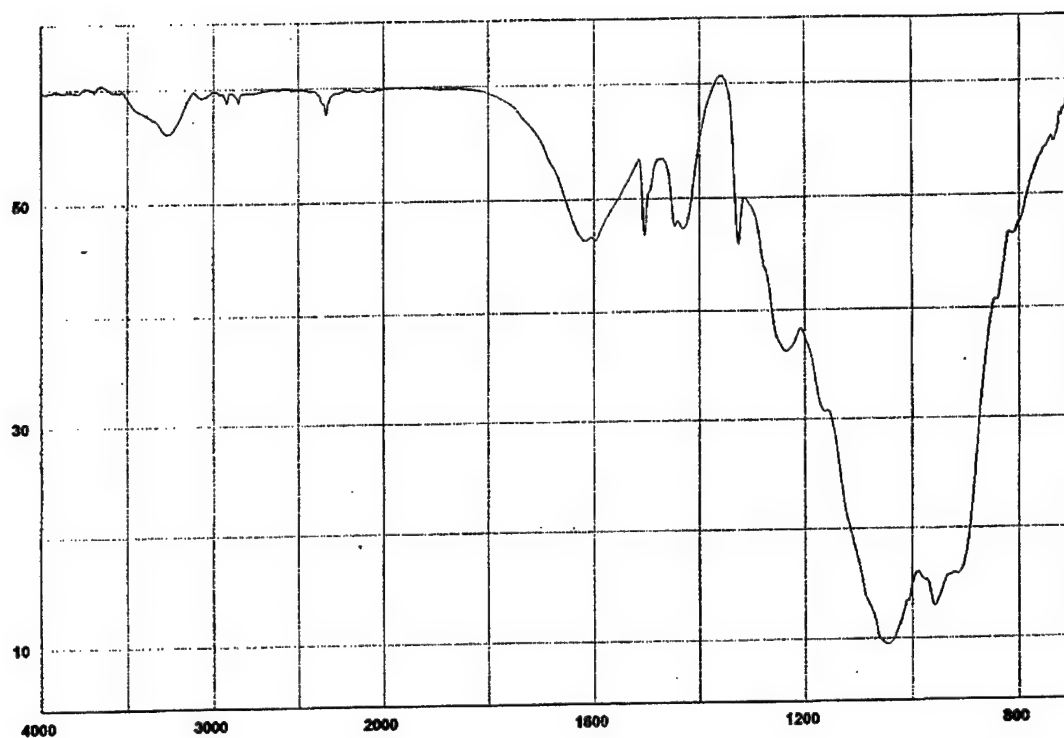
File # 1 = WRPC024

2R2VP21400VT530, Rod, inside, 1st wear track

X-Zoom CURSOR

4/15/95 3:32 PM Res=4 cm-1

Figure 40. FTIR spectrum of the rod after the bearing temperature test with PAO/TBPP vapor.



Transmittance / Wavenumber (cm-1)

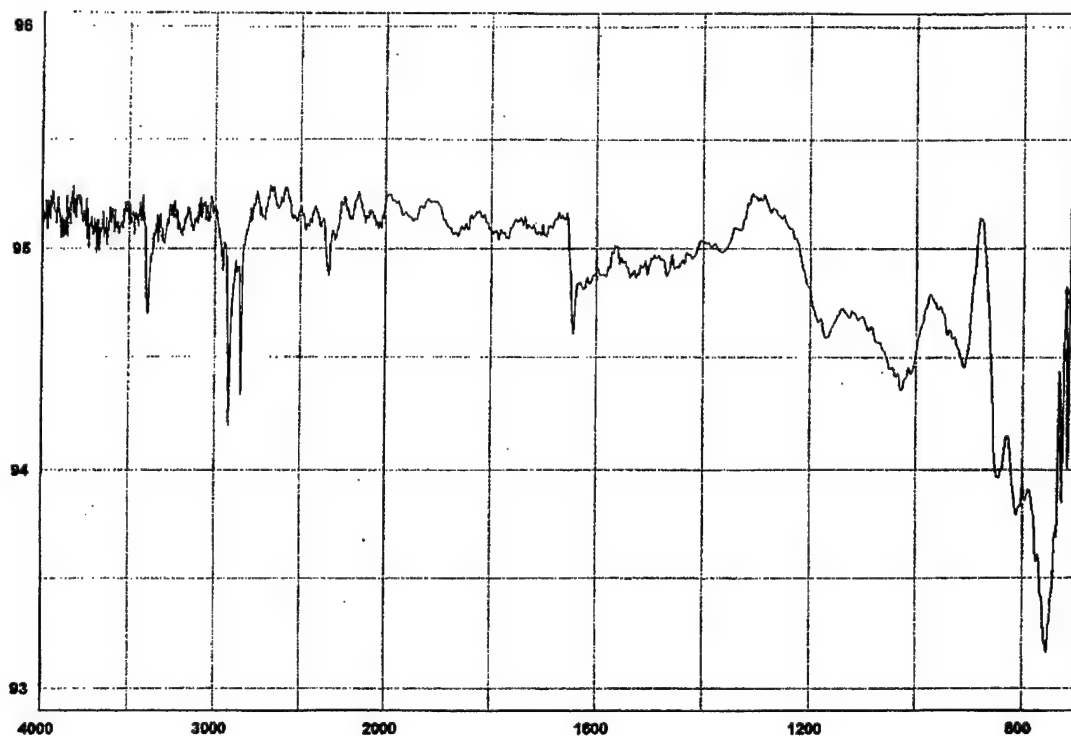
File # 1 = WRPC032

2RZVP21800VT530, Rod, outside, 1st wear track

X-Zoom CURSOR

4/16/95 9:05 AM Res=4 cm-1

Figure 41. FTIR spectrum of the rod after the bearing temperature test with X-1P vapor.



Transmittance / Wavenumber (cm-1)

X-Zoom CURSOR

File # 1 = WRPC042

4/16/95 11:18 AM Res=4 cm-1

2R2VP21900VT630, Rod, outside, 2nd wear track

Figure 42. FTIR spectra of the rod after the bearing temperature test with 5P4E vapor.

### 4.3 Raman Spectroscopy Results

Raman spectra of the rod specimen, corresponding to Sample Set 2 outside and inside the bearing track, are shown in Figs. 43 and 44. The two large Raman bands at 1355 and 1590  $\text{cm}^{-1}$  are characteristic of amorphous carbon with strain in the lattice structure (62). The relative intensity of the 1355  $\text{cm}^{-1}$  band to the 1590  $\text{cm}^{-1}$  band is a measure of the relative degree of disorder in the graphitic structure (63) and the shift of the 1590  $\text{cm}^{-1}$  from 1580  $\text{cm}^{-1}$  towards 1620  $\text{cm}^{-1}$  is a measure of the strain in the graphitic structure (62). The minor transition at 657  $\text{cm}^{-1}$ , outside the bearing track is consistent with  $\text{Fe}_3\text{O}_4$  (64). The minor transition at 434  $\text{cm}^{-1}$ , inside the bearing track, has not been identified.

Raman spectra inside the bearing track, after bearing temperature tests with PAO/TBPP, X-1P, 5P4E vapor are shown in Figs. 45-47. All of the deposition films indicate the presence of amorphous carbon. The bands at 1360  $\text{cm}^{-1}$  and 1620  $\text{cm}^{-1}$  in the PAO/TBPP deposition film are similar to bands produced on oxidized and polished surfaces of carbon (63). The transitions at 347  $\text{cm}^{-1}$  and 416  $\text{cm}^{-1}$  in the



PAO/TBPP deposition film have not been identified. Transitions in the 5P4E deposition film are consistent with:  $\text{Fe}_2\text{O}_3$ , at 221, 291, and 406  $\text{cm}^{-1}$  (64);  $\text{Si}_3\text{N}_4$  at 612  $\text{cm}^{-1}$ ;  $\text{Fe}_3\text{O}_4$  at 657  $\text{cm}^{-1}$  (64); and amorphous carbon at 1355 and 1590  $\text{cm}^{-1}$ . The 5P4E deposition film, also, appears to contain less amorphous carbon than the films obtained with vapor phase lubricants containing phosphorus.

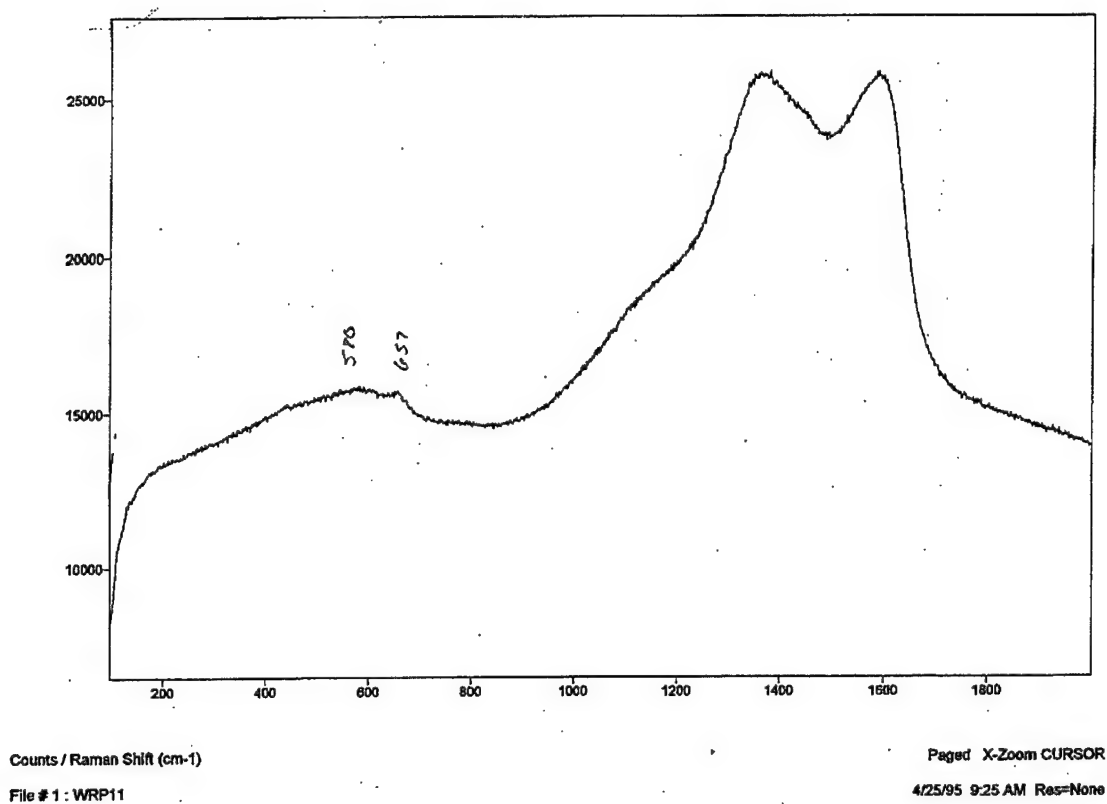
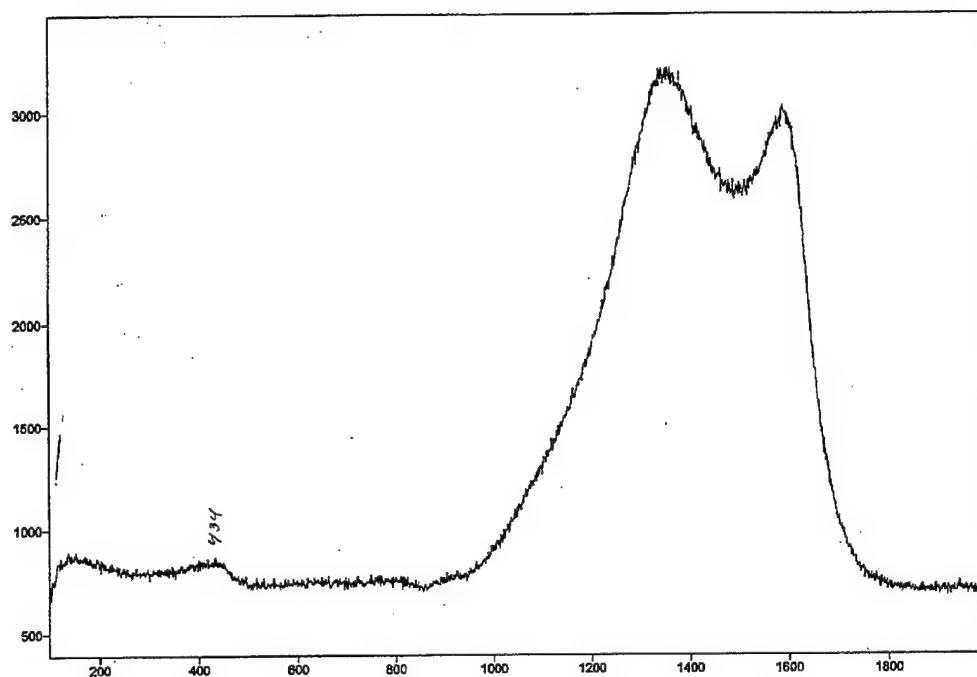


Figure 43. Raman spectrum of the rod outside the bearing track after the bearing temperature test with TBPP vapor.



Counts / Raman Shift (cm-1)

File # 2 = WRP12

Paged X-Zoom CURSOR

4/25/95 9:39 AM Res=None

Figure 44. Raman spectrum of the rod inside the bearing track after the bearing temperature test with TBPP vapor.

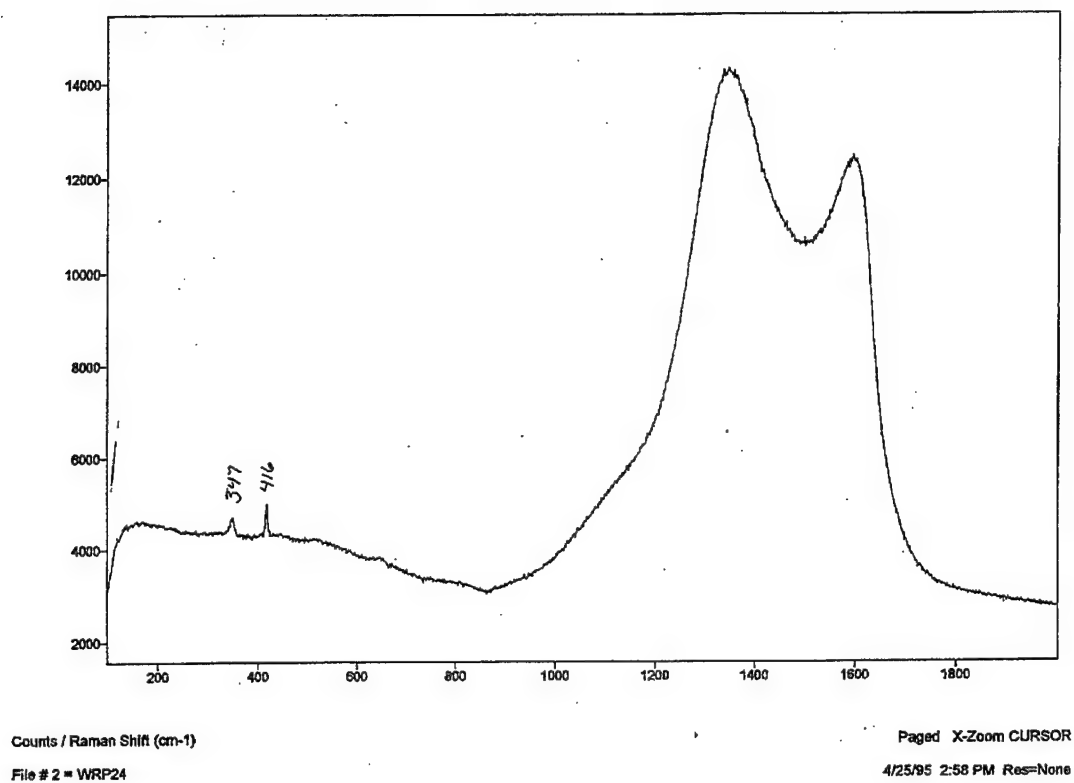


Figure 45. Raman spectrum of the rod inside the bearing track after the bearing temperature test with PAO/TBPP vapor.

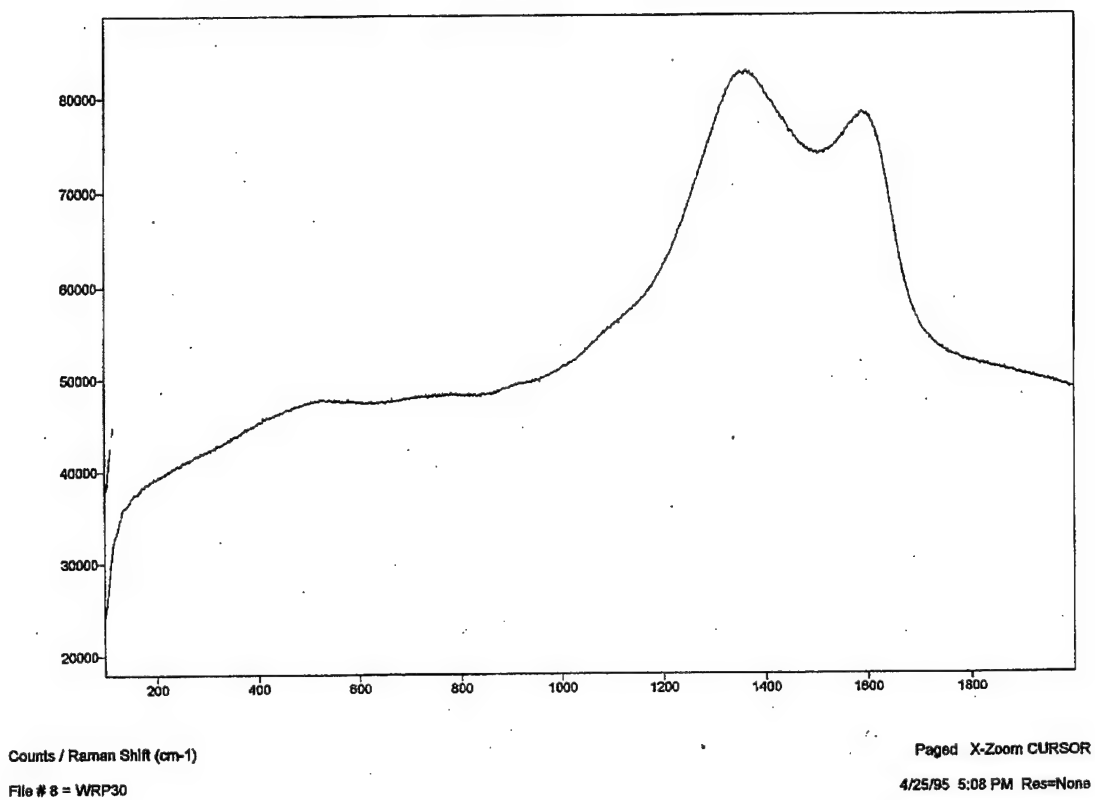


Figure 46. Raman spectra of the rod after the bearing temperature test with X-1P vapor.

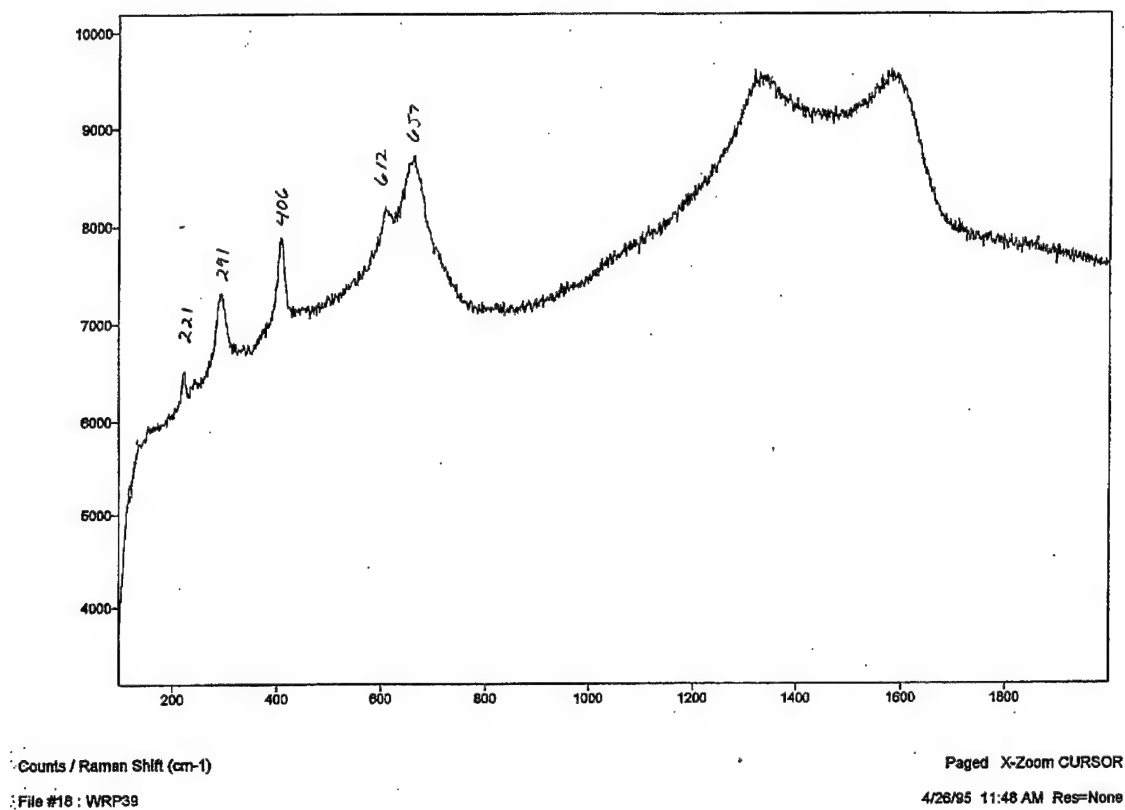


Figure 47. Raman spectra of the rod after the bearing temperature test with 5P4E vapor.

#### 4.4 AES Results

An AES depth profile of a TBPP deposition film, formed in the bearing track of the rod from Sample Set 1, is shown in Fig. 48. The results indicate that the deposition film is predominately composed of carbon and iron, with lesser amounts of oxygen, phosphorus, and chromium. The shape of the iron and carbon profiles are consistent with diffusion profiles, generated by two semi-infinite sources bound at a common interface (65,66). The Matano interface, which defines the conservation of mass boundary, occurs in the vicinity of 30 nm. The maximum level of phosphorus was found at a depth of approximately 14 nm, in the deposition film. After 10 minutes of sputtering; i.e., 80 nm, the composition of the material remains relatively constant. Table 11 compares the known composition of T15 steel to the composition detected at 14 nm, 30 nm, and 80 nm. Also, included in Table 11, is the composition detected with an untested T15 rod. The untested rod was used as the reference sample. The composition at 80 nm indicates a decrease in iron from the reference sample, with corresponding increases in carbon, phosphorus, and oxygen. Tungsten and vanadium are probably also present;

however, these elements were not sampled for this particular specimen.

Auger spectra were also obtained in the bearing track of the rod from Sample Set 6. This particular specimen had larger areas of surface damage than other TBPP lubricated specimens and was, thus, better suited for elemental analysis of a region associated with corrosion pitting. The specimen analyzed was previously shown in Figs. 28 and 29. Auger spectra, obtained inside and outside the damaged region, are shown in Figs. 50 and 51. In both cases the spectra are for the elements detected after sputtering 10 nm of the surface. The damaged region indicates a higher percentage of carbon, phosphorus, and oxygen than the undamaged region, with a corresponding decrease in iron. Elemental results, prior to and after a 10 nm sputter, are summarized in Table 12. A depth profile of the corrosion pit is shown in Fig. 52. In comparison to Fig. 48, the region associated with corrosion pitting indicates a decrease in the concentration of iron; with increased concentrations of phosphorus, carbon, and oxygen; and the effects are seen at a deeper level in the substrate.



Table 11. - Auger Elemental Analysis of a TBPP Deposition  
Film

Remark	Element									
	Fe	C	Mn	Si	Cr	V	W	Co	P	O
Known Composition of T15 by Atomic%	73.1	7.35	0.28	0.63	4.4	5.6	3.8	4.8	-	-
TBPP Specimen Unspattered	1.5	89.5	-	-	0.3	-	-	-	0.7	7.0
TBPP Specimen 18 nm Sputtered	6.0	78.0	-	-	2.0	-	-	-	6.0	8.0
TBPP Specimen 80 nm Sputtered	61.0	27.5	-	-	6.0	-	-	-	2.5	3.0
T15 Specimen Untested	58.0	15.0	-	-	7.0	3.0	13.0	5.0	-	-

Table 12. - Auger Elemental Analysis of a TBPP Corrosion Pit

Remark	Element							
	Fe	C	Cr	V	W	Co	P	O
Wear Track	2.6	87.2	-	0.7	-	-	1.0	8.6
Unspattered								
Corrosion Pit	7.3	89.4	-	0.5	-	-	1.2	7.3
Unspattered								
Wear Track	16.4	49.7	3.7	3.8	10.3	2.8	3.1	10.1
10 nm Sputter								
Corrosion Pit	7.2	70.9	1.7	0.8	4.4	1.1	4.1	9.8
10 nm Sputter								

T-15 Rod Test 2R2VP2830800485 AES Depth Profile in Wear Track

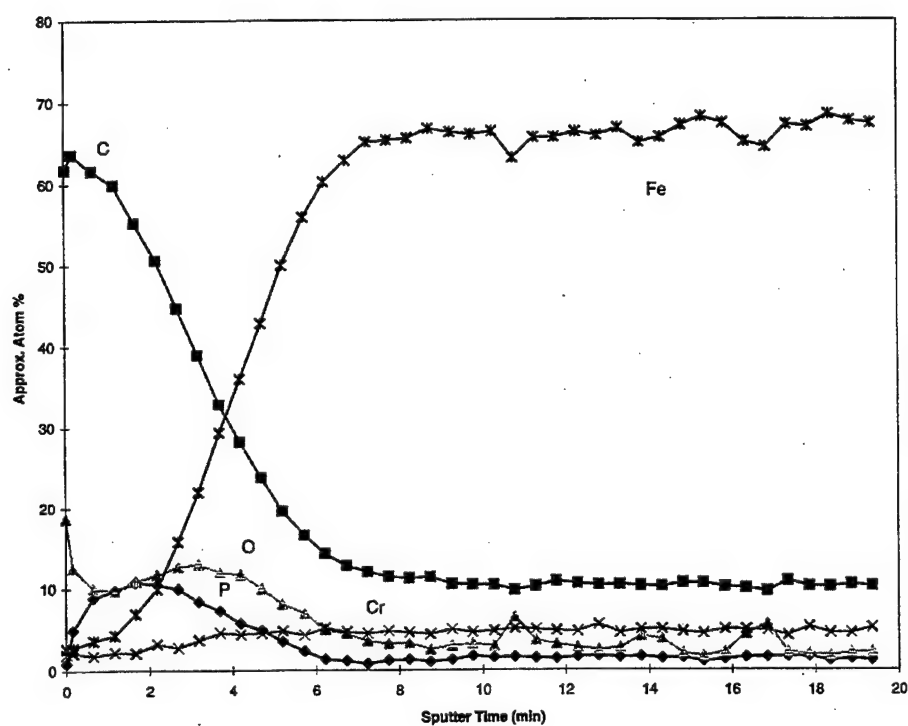


Figure 48. Auger depth profile of a TBPP deposition film formed in the bearing track.

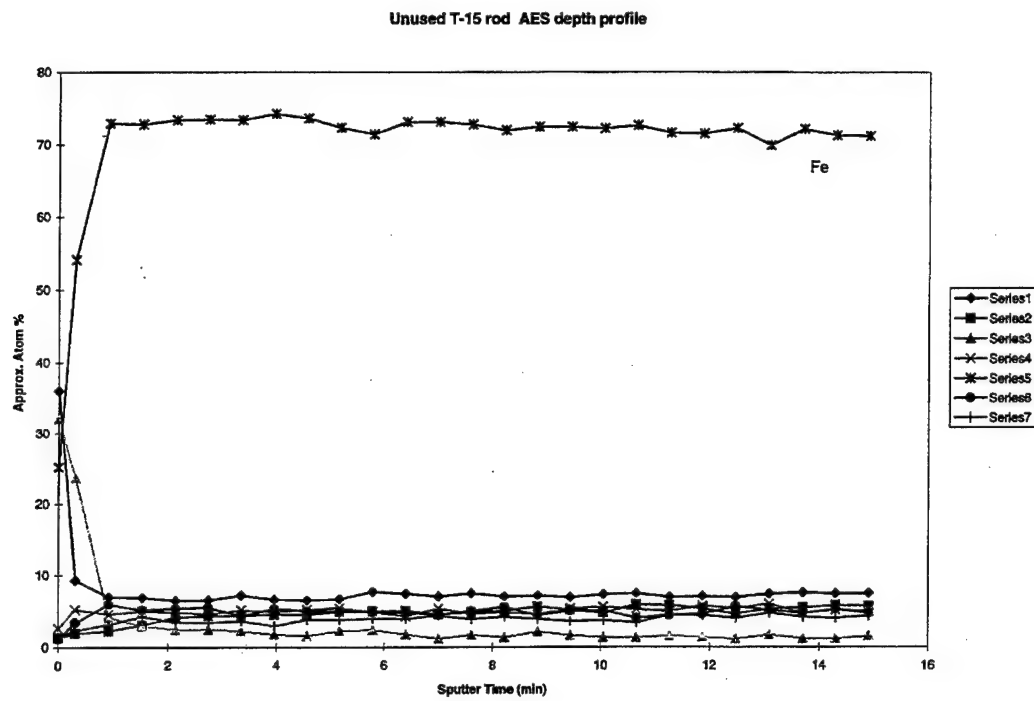


Figure 49. Auger depth profile of an unused T15 rod.

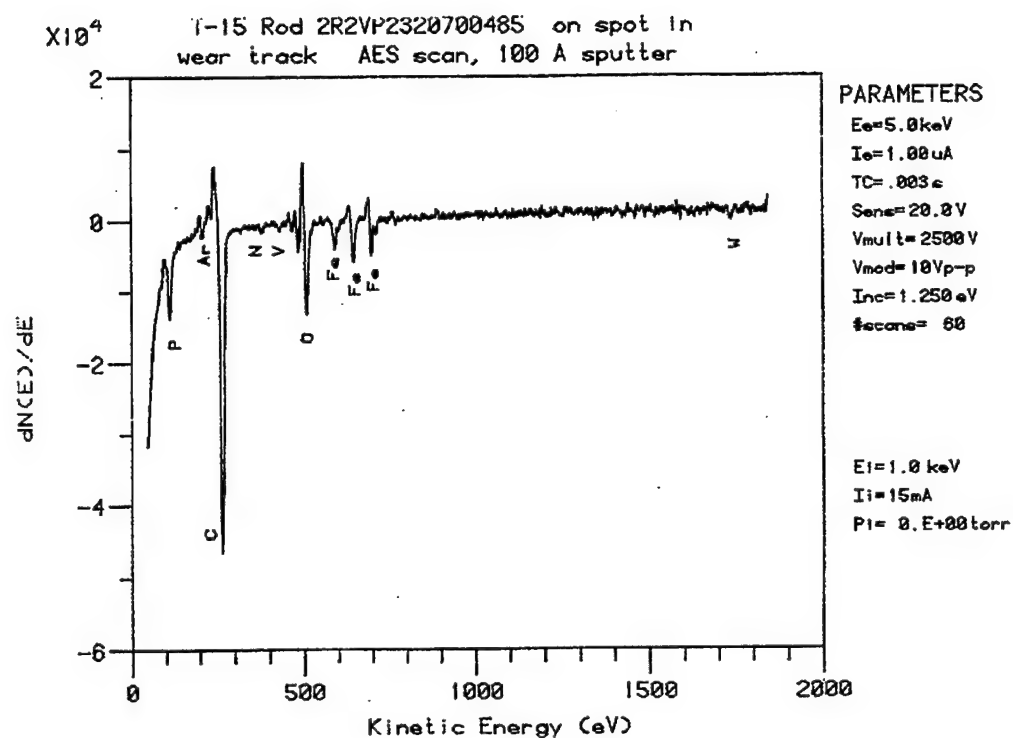


Figure 50. Auger spectrum formed in the bearing track separate of a corrosion pit.

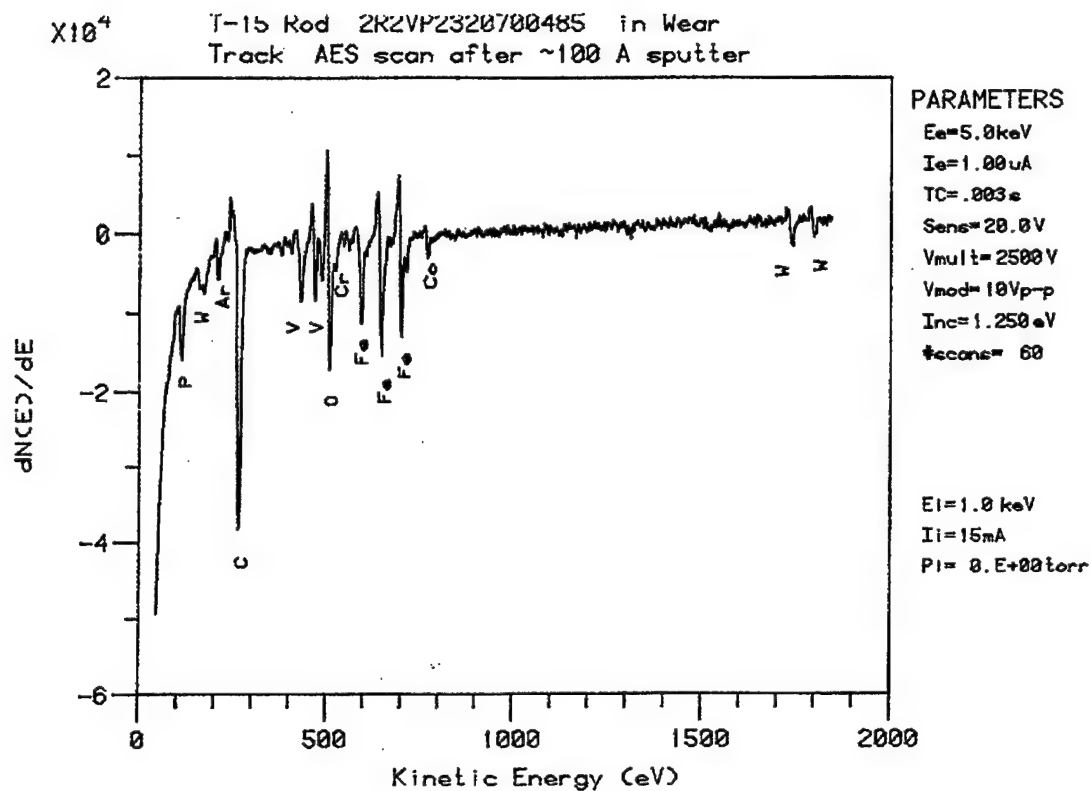


Figure 51. Auger spectra obtained in a region associated with corrosion pitting.

T-15 Rod Test 2R2VP2320700485 AES Depth Profile on Spot in Wear Track

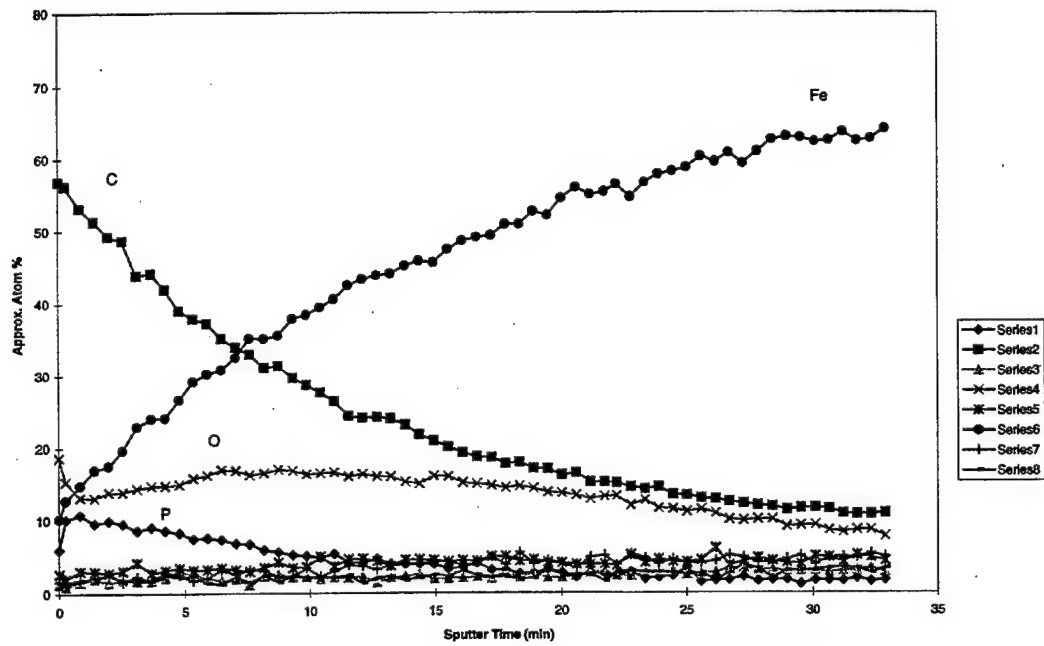


Figure 52. Auger depth profile of the region associated with corrosion pitting.

#### 4.5 SEM/EDS Results

A photograph of the cross-sectioned rod from Sample Set 1 is shown in Fig. 53. An SEM image of the bearing track subsurface is shown in Fig. 54. The darker region shows penetration of a damaged area into the matrix of the steel. The maximum depth of penetration is approximately 10  $\mu$ , one-half the distance of the maximum wear determined from the profilometry trace shown in Fig. 10.

The boundary of the corrosion pit with the normal matrix of the bearing steel at higher magnification is shown in Fig. 55. The grain boundaries of the steel are visible and the darker region is penetrating into the grains themselves. There also appears to be a slight preferential attack at the grain boundaries.

The localized regions, denoted by the letters A-G in Fig. 55, were further examined, using EDS analysis. The EDS spectra, corresponding to these regions, are shown in Figs. 56-62. Table 13 lists the composition of the different regions based on the EDS spectra. In comparing the spectra of region "C", Fig. 58, to the region labeled "G", Fig. 62,



it is clear that the matrix of the steel has been altered. In particular, the darker region labeled "G" is significantly reduced in iron. Sodium and sulfur are also present in the modified matrix with an increase in carbon.

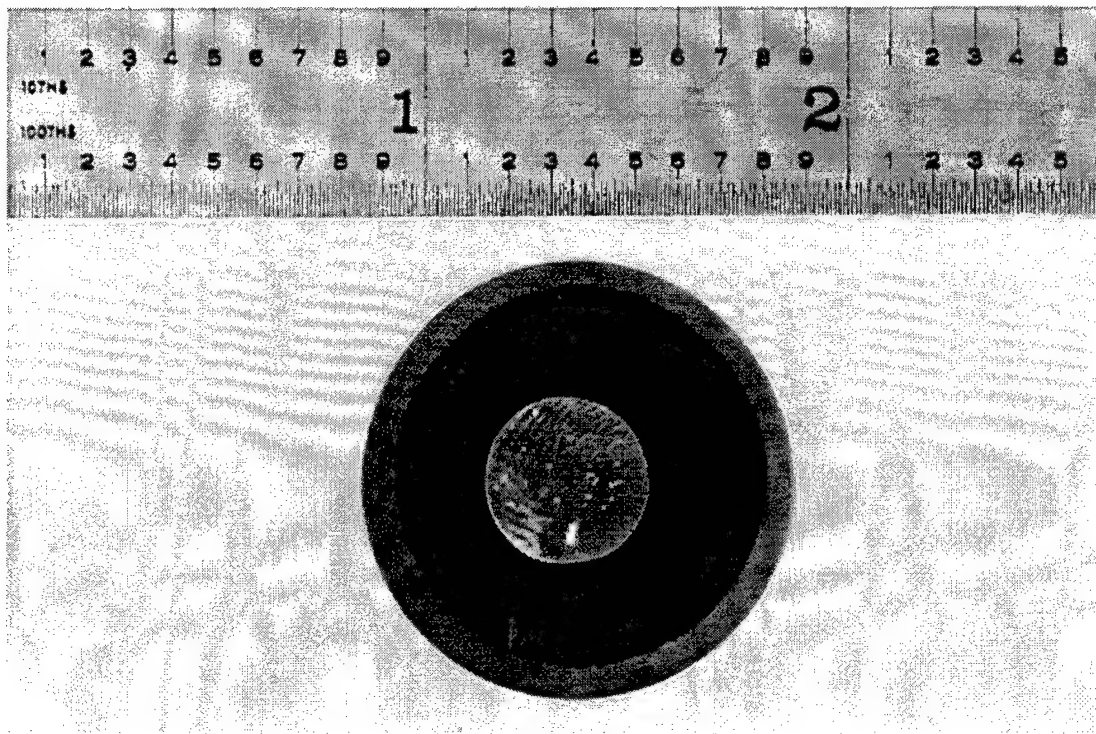


Figure 53. Sectioned rod mounted in epoxy after polishing.



T15 Rod, T15 Races, T15 Balls, Steel Cage  
Test Temp.: 371°C, Vapor Temp.: 329°C  
Lubricant: Durad 620B, Flow Rate: 2.5 ml/hr  
Run Time: 96 hrs., Stress: 3.34 GPa

Figure 54. SEM image of a corrosion pit penetrating into the subsurface.

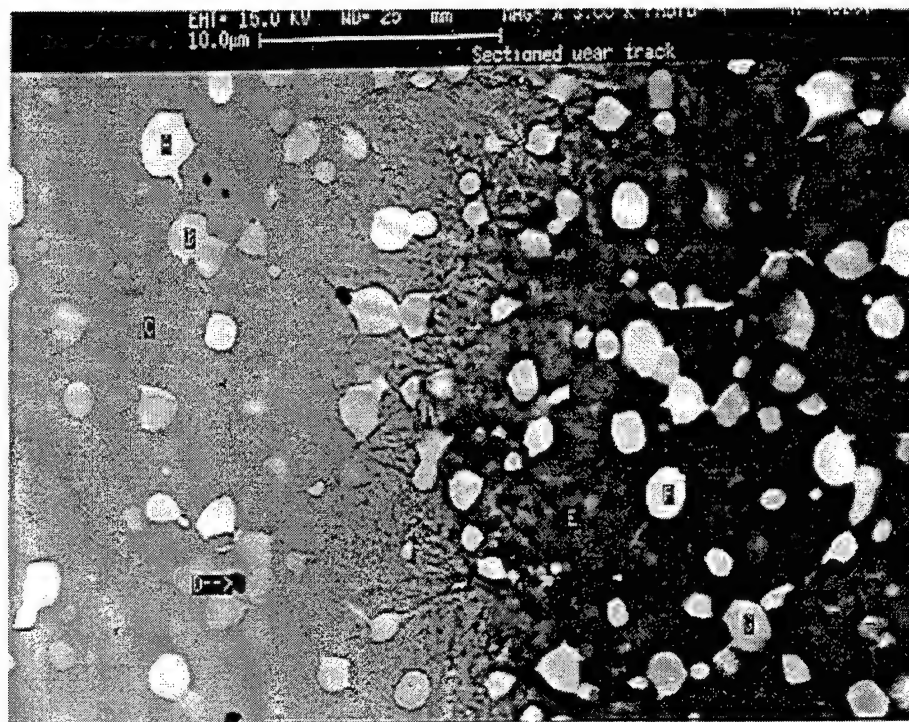


Figure 55. Boundary of the corrosion pit with the normal T15 steel.

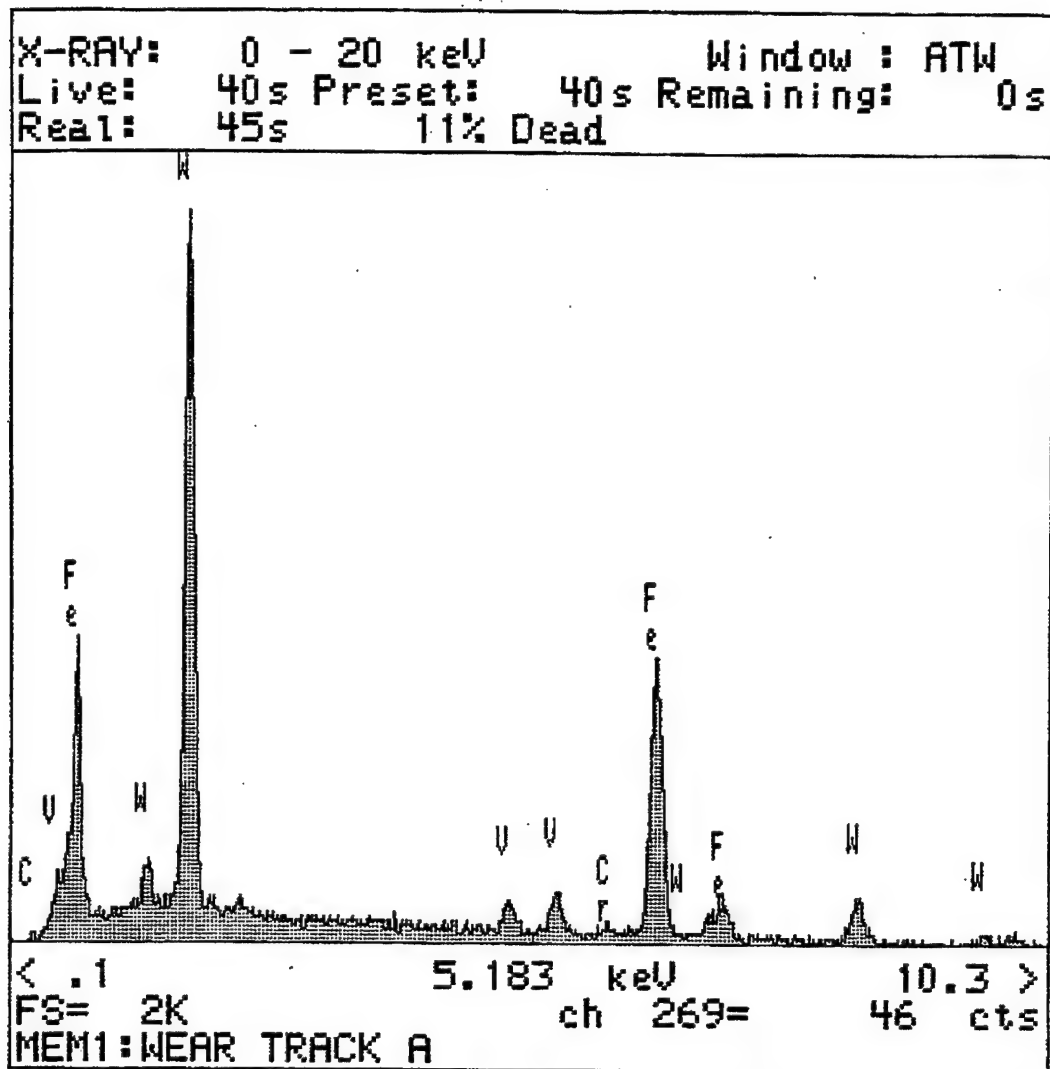


Figure 56. Energy dispersive spectroscopy (EDS) spectrum of region "A" in Fig. 55.

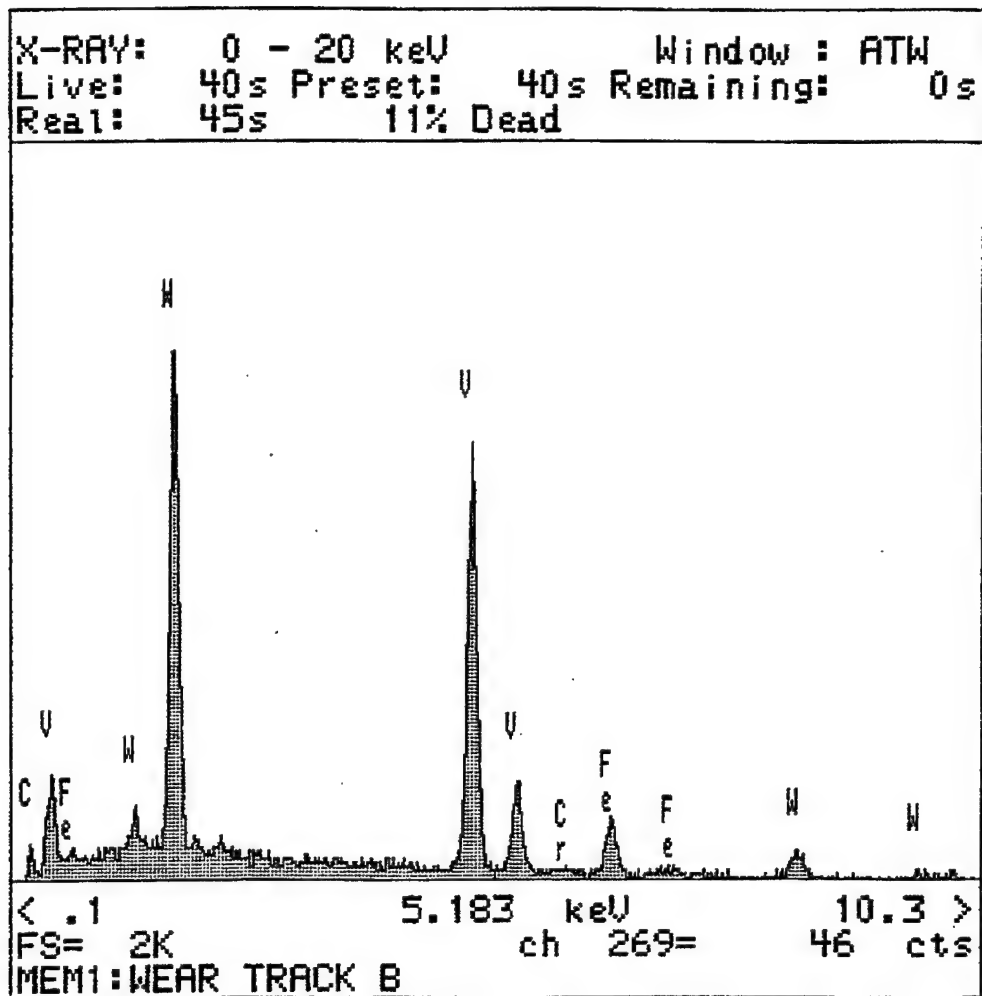


Figure 57. EDS spectrum of region "B" in Fig. 55.

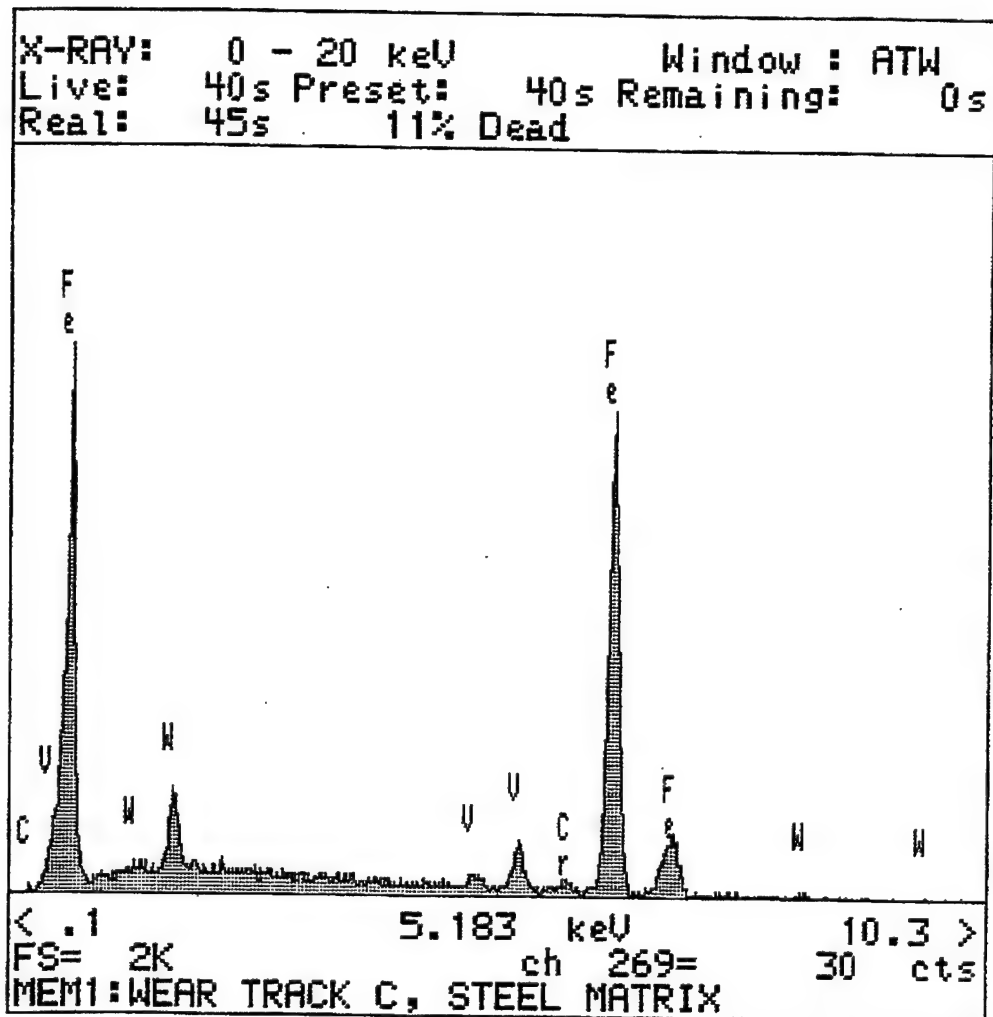


Figure 58. EDS spectrum of region "C" in Fig. 55.

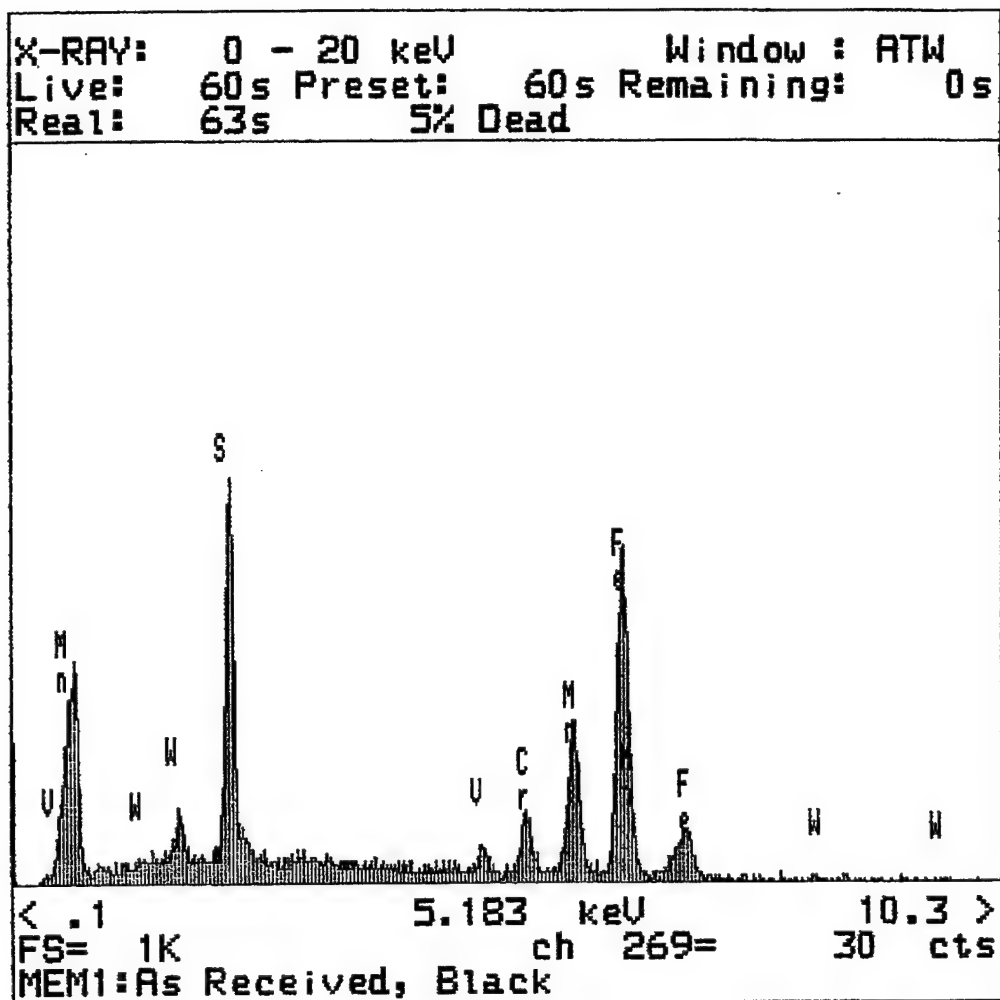


Figure 59. EDS spectrum of region "D" in Fig. 55.



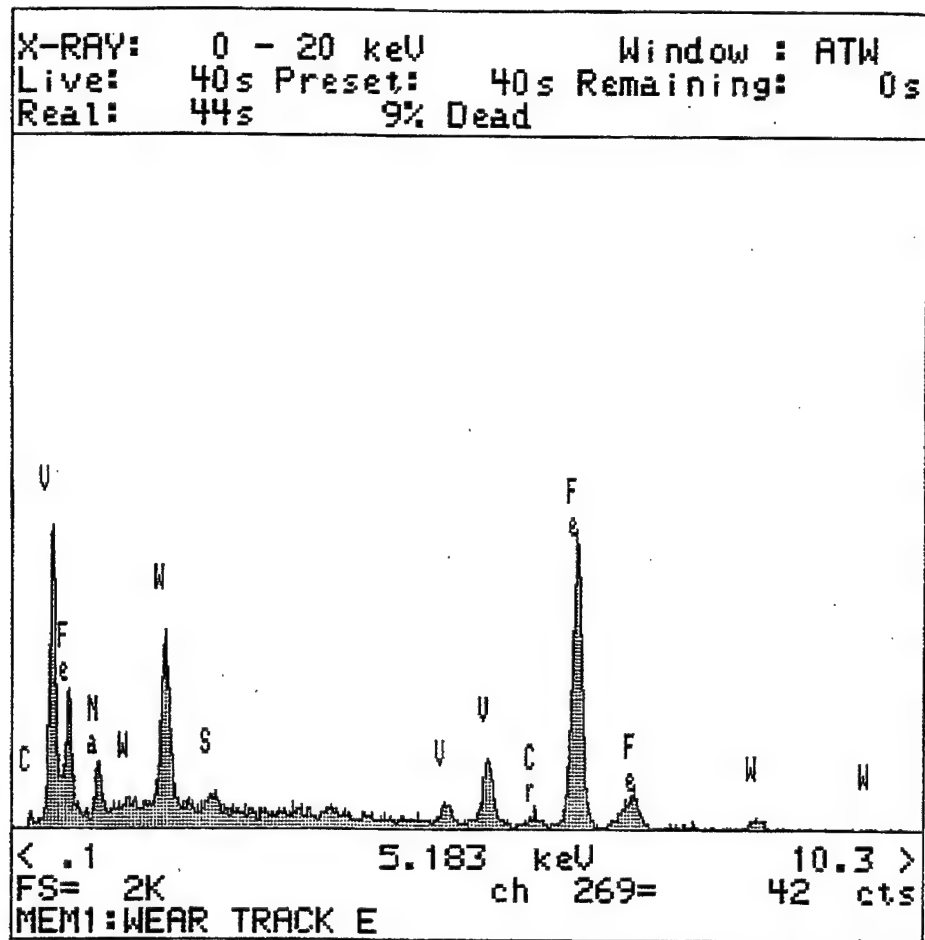


Figure 60. EDS spectrum of region "E" in Fig. 55.

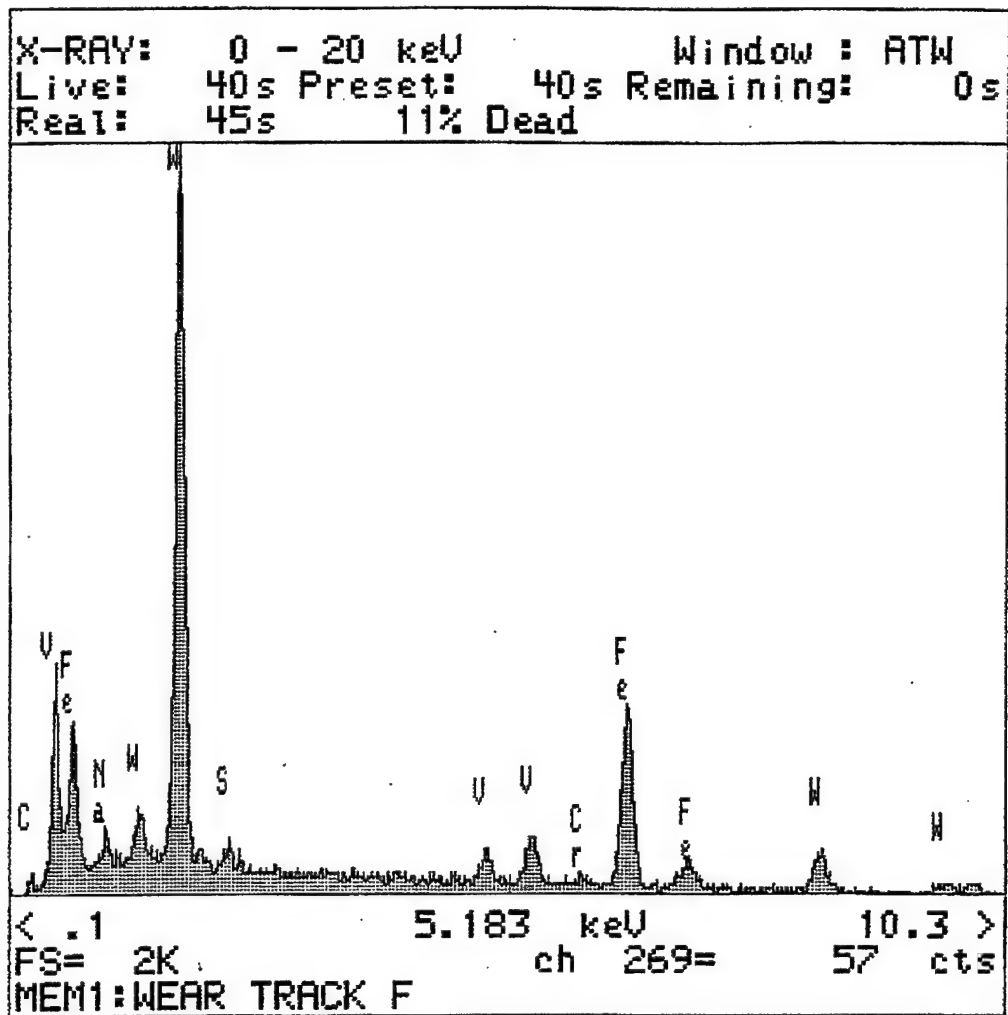


Figure 61. EDS spectrum of region "F" in Fig. 55.

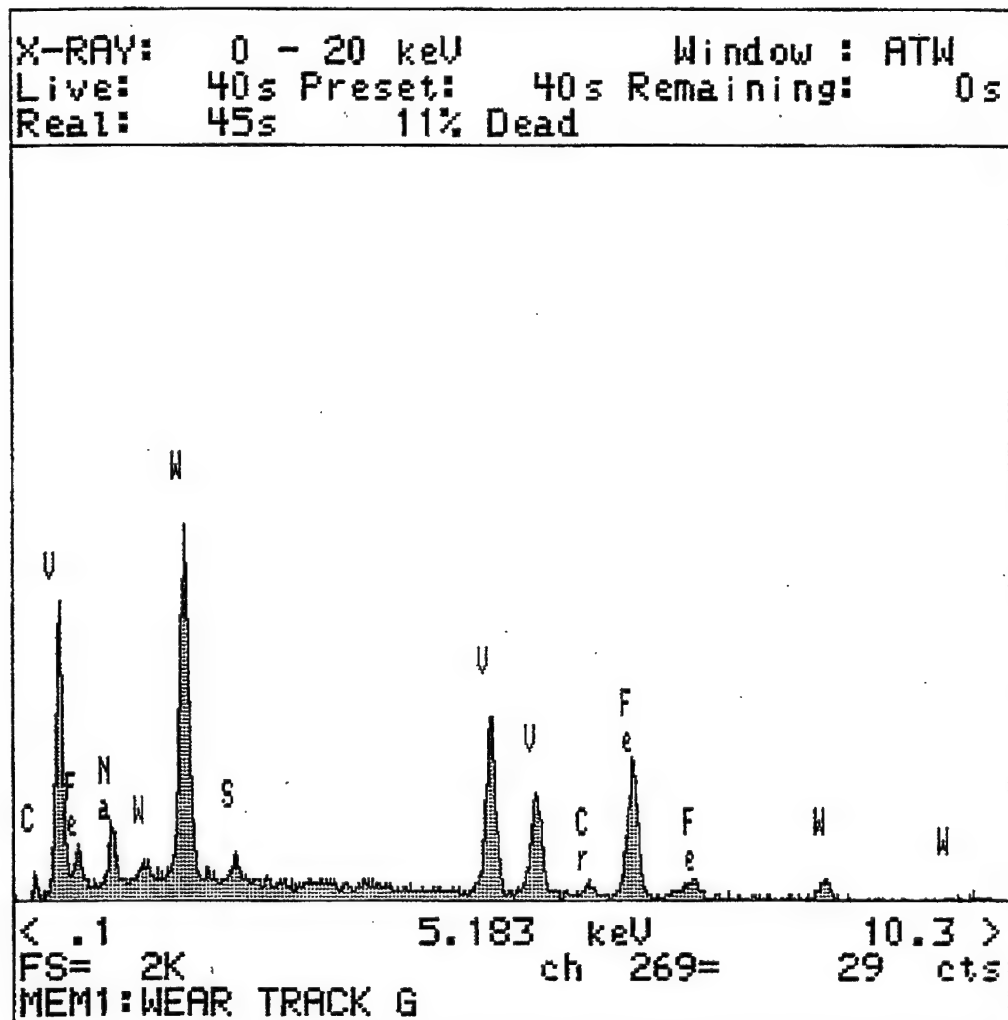


Figure 62. EDS spectrum of region "G" in Fig. 55.

---

Table 13. - Composition of Sectioned Wear Track

---

Region	Proposed Composition
A	Tungsten Carbide
B	Metallic Carbide
C	T15 Matrix
D	Manganese Sulfide
E	Modified T15 Matrix
F	Tungsten Carbide
G	Metallic Carbide

---

#### 4.6 Discussion

$\mu$ -FTIR results indicate that all of the vapor phase lubricants containing phosphorus, TBPP, PAO/TBPP, and X-1P, form a deposition film composed of P-O, P-H, and P-O-P bonds, outside of the bearing track. Bands associated with the n-alkanes were also found in specimens, lubricated with TBPP vapor at bearing temperature of 370°C. At higher bearing temperatures, i.e., Fig. 38 compared to Figs. 32 and 33, there was a decrease in the n-alkanes, an increase in the P-H bond, and shift of the P-O bond from 1060  $\text{cm}^{-1}$  to 970  $\text{cm}^{-1}$ . The shift in the P-O bond is consistent with an increase in P-O-P linkages. Inside the bearing track, infrared absorption did not occur, probably due to insufficient film thickness and the relatively large percentage of carbon detected.

Morales, et al., found similar results using  $\mu$ -FTIR analyses performed insitu with the deposition of TCP vapor on an iron coated NaCl window (38). Possible bonds identified by Morales include P-O, P-H, P-O-P, P-O-C, P=O, and n-alkanes. Morales concluded that the film initiated as

FePO<sub>4</sub>·2H<sub>2</sub>O, followed by a polymeric growth of an organophosphorus compound. Since phosphorus bonds were not detected on the Si<sub>3</sub>N<sub>4</sub> ball, it seems likely that iron is involved in the formation of the phosphate/phosphite structure on the metallic specimens. Additionally, previous efforts have reported the formation of FePO<sub>4</sub>·2H<sub>2</sub>O on ferrous materials exposed to TCP in the liquid state (36,37). However, the infrared spectra detected on the rods do not match the iron phosphate spectrum shown in Fig. 34, suggesting that the types of phosphates detected are more complicated than simple iron phosphate.

Further insight is provided by considering the properties of the P-O-P bonds detected. P-O-P bonds exist in the form of condensed phosphates, of which there are three major groups (67):

<u>Functional Group</u>	<u>Stoichiometry</u>	<u>Structure</u>
(a) Linear Polyphosphate	P <sub>n</sub> O <sub>3n+1</sub> <sup>(n+2)-</sup>	chains
(b) Metaphosphates	P <sub>n</sub> O <sub>3n</sub> <sup>n-1</sup>	rings
(c) Ultraphosphates	P <sub>n</sub> O <sub>3n+m</sub> <sup>(n+2m)-</sup>	cages, sheets,
	1 ≥ m ≤ n/2	3-D structures

All condensed phosphates form by the repeated condensation of tetrahedral  $\text{PO}_4$  groups, which link by sharing a common oxygen atom (67). In this manner, condensed phosphates form at elevated temperatures from smaller phosphate molecules (67). For  $n=m=1$ , these compound reduce to the phosphate ion  $\text{PO}_4^{-3}$ . For larger values on  $n$ , all of these compounds approach an oxygen to phosphorus ratio of 3. Examples of condensed phosphates in crystalline form and as a phosphate glass are shown in Figs. 63 and 64. The width of the infrared bands, detected in the deposition film, are more indicative of an amorphous structure such as a phosphate glass.

The Auger depth profiles shown in Figs. 48 and 52 do not support the required stoichiometry for phosphorus and oxygen solely in the form of phosphates, condensed phosphates, or phosphites. Specifically, the level of phosphorus is much higher than required. This indicates that phosphorus must be present in other forms. In a previous study of iron foils exposed to TCP vapor in  $\text{N}_2$  atmosphere at  $700^\circ\text{C}$ , Klaus, et al., (68) found that the deposition film was composed of  $\text{Fe}_3\text{P}$  and  $\text{Fe}_3\text{C}$  near the iron substrate,  $\text{Fe}_2\text{P}$  and  $\text{Fe}_5\text{C}_2$  in the intermediate film, and  $\text{FePO}_4$  at the film and vapor boundary. Klaus' results were determined, using x-ray diffraction

(XRD). Since XRD is not sensitive to amorphous structures, this technique would not be able to identify the presence of a phosphate glass structure. The higher ratio of phosphorus to oxygen detected in the AES analyses, could be a result of  $\text{Fe}_3\text{P}$  and  $\text{Fe}_2\text{P}$  in the deposition film, in addition to amorphous and crystalline phosphates and phosphites. Unfortunately, the curved surface of the rod specimen is not amenable to XRD for similar analyses.

The Raman analyses indicate that a graphitic structure is present in deposition films formed with the TBPP, PAO/TBPP, X-1P, and 5P4E lubricants. However, the films generated with the organophosphorus lubricants indicated a stronger presence of graphite in the deposition film. Additionally, films generated with the organophosphorus lubricants showed very little or no detectable amounts of metal oxide on the bearing surface. In comparison, the 5P4E deposition film showed several bands consistent with  $\text{Fe}_2\text{O}_3$  and  $\text{Fe}_3\text{O}_4$ . It is also worth noting, that the 5P4E deposition film was generated at a lower bearing temperature than the TBPP and X-1P films. The ability of the organophosphorus lubricants to provide oxidation protection is not surprising. Alkyl phosphate esters have proven to be very



good oxidation inhibitors for graphitic structures at temperatures up to 400°C (69). Additionally, phosphate glasses are commonly used as oxidation inhibitors for C-C composites at even higher temperatures. Phosphate films are also commonly used on ferrous materials for corrosion protection (70). An important role of the organophosphorus lubricants appears to be their ability to protect the bearing surface, while maintaining higher levels of lubricious carbon in the deposition film at elevated temperatures. Iron oxides and particularly,  $\text{Fe}_2\text{O}_3$ , are known to be abrasive in tribocontacts (71).

The decreased levels of iron with significant increases in oxygen, phosphorus, and carbon in the damaged area of Sample Set 6 supports a corrosion mechanism. Surfaces, which are passivated by normally protective films, are often susceptible to corrosion pitting in regions of high tensile stress (72). This is consistent with findings in Chapters 2 and 3. Additionally, enhanced corrosion pitting of substrates, protected by phosphate films, has been noted, when high levels of carbon are present (73).

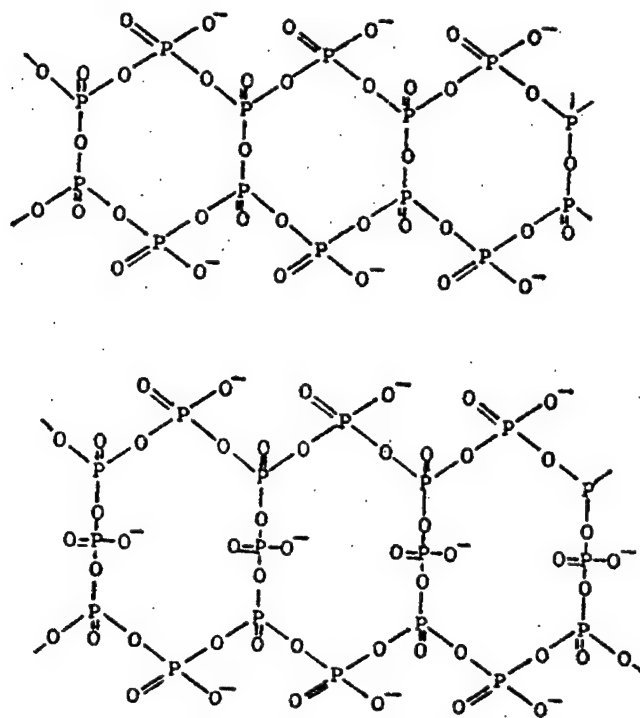


Figure 63. Structures of typical condensed phosphate crystals.

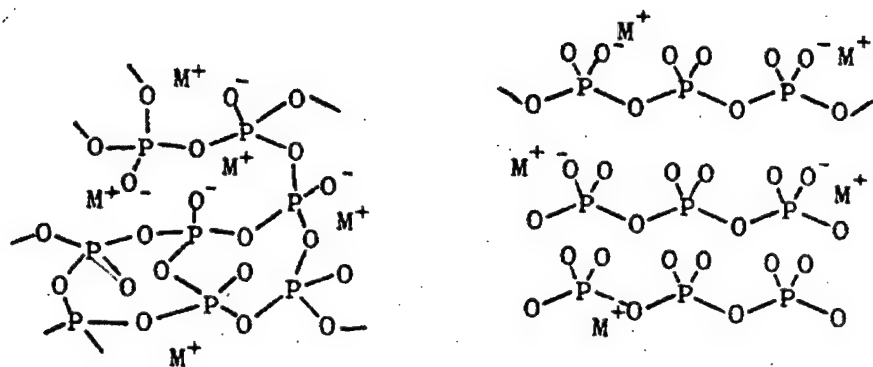


Figure 64. Structures of typical condensed phosphate glasses.

## CHAPTER 5

### DIFFUSION ANALYSES

In Chapter 4 it was noted that AES depth profiles obtained on surfaces lubricated with TBPP vapor, were consistent with known diffusion profiles. Specifically, the iron and carbon composition in the subsurface varied, in a manner consistent with the solutions expected for two semi-infinite materials bound at a common interface. The objective of the work described in this chapter was to apply the semi-infinite solution to determine the order of magnitude of the diffusion coefficients for iron and carbon. Once the magnitude of the diffusion coefficients are known, then mechanism(s) which govern the film growth can be postulated.

## 5.1 Theory and Governing Equations

Fick's second law describes mass diffusion in a concentration gradient, when mass is conserved (74,75). If the diffusion coefficient is independent of the gradient, Fick's second law, in one dimension, can be expressed as:

$$\text{Eq 2: } \frac{\partial c}{\partial t} = \nabla \left( D \frac{\partial c}{\partial x} \right) = D \frac{\partial^2 c}{\partial x^2}$$

Equation 2 has the following solutions for the prescribed boundary conditions (65,66):

$$\text{Eq 3: } c_{Fe}(x,t) = \frac{c_{Fe}^{+\infty} - c_{Fe}^{-\infty}}{2} \left[ 1 + \operatorname{erf} \left( \frac{x}{2\sqrt{Dt}} \right) \right] + c_{Fe}^{+\infty}$$

$$c_{Fe}(x,0) = c_{Fe}^{+\infty}; x > 0$$

$$c_{Fe}(x,0) = c_{Fe}^{-\infty}; x < 0$$

$$\text{Eq 4: } c_C(x,t) = \frac{c_C^{-\infty} - c_C^{+\infty}}{2} \left[ 1 - \operatorname{erf} \left( \frac{x}{2\sqrt{Dt}} \right) \right] + c_C^{+\infty}$$

$$c_C(x,0) = c_C^{+\infty}; x < 0$$

$$c_C(x,0) = c_C^{-\infty}; x > 0$$

The concentration gradients for Equations 3 and 4 were obtained by applying the chain rule to the definition of the error function (76) and differentiating the concentration with respect to  $x$ . The resulting equations are:

$$\text{Eq 5: } \frac{\partial c_{Fe}}{\partial x} = \frac{c_{Fe}^{+\infty} - c_{Fe}^{-\infty}}{2\sqrt{\pi Dt}} \exp\left[\frac{-x^2}{4Dt}\right]$$

$$\text{Eq 6: } \frac{\partial c_C}{\partial x} = \frac{c_C^{-\infty} - c_C^{+\infty}}{2\sqrt{\pi Dt}} \exp\left[\frac{-x^2}{4Dt}\right]$$

When diffusion occurs in a concentration gradient, it is often the case that the diffusion coefficient will vary with the concentration (77,78). This is equivalent to saying that the diffusion coefficient is a function of  $x$  since the concentration varies with  $x$ ;

$$\text{Eq 7: } D = f(x)$$

In this situation, Equation 2 becomes a nonhomogeneous differential equation, and Equations 3 and 4 are no longer valid.

Although Equation 2 has no known closed form solution when  $D = f(x)$ , the diffusion coefficient at a specific location, defined by  $c(x_m) = c_m$ , can be determined using the Boltzman-Matanao method (77,79).

$$\text{Eq 8: } D = \frac{1}{2t} \frac{dx}{dc} \bigg|_{c=c_m} \int_{c_m}^{c+\infty} x dx$$

The reciprocal of the concentration gradient,  $dx/dc$ , and the integral term are usually determined graphically from experimental data. The method is depicted in Fig. 65. The Matano interface is the boundary where the depletion of mass on one side of the surface equals the accumulation on the other side of the surface, i.e., a conservation of mass surface.

When one solid diffuses at a faster rate in a pair of semi-infinite solids, the Matano interface between the solids moves in time. This is known as the Kirkendall effect (77,78). The diffusion coefficient, determined from a Boltzman-Matano analysis,  $D$ , is then a mean value between the intrinsic diffusion coefficients,  $D_{Fe}$  and  $D_C$ . To determine  $D_{Fe}$  and  $D_C$ , a system of two equations in two unknowns is solved using Darken's analysis (77,78):

$$\text{Eq 9: } v_m = \frac{1}{c_T} \left[ D_{Fe} \frac{\partial c_{Fe}}{\partial x} + D_C \frac{\partial c_C}{\partial x} \right]_{x=x_m}$$

$$\text{Eq 10: } D = \left[ \frac{c_C}{c_T} D_{Fe} + \frac{c_{Fe}}{c_T} D_C \right]_{x=x_m}$$

Where the term  $c_T$  is the total concentration:

$$\text{Eq 11: } c_T = [c_{Fe} + c_C]_{x=x_m}$$



The values of  $D_{Fe}$  and  $D_C$  calculated from Equations 9 and 10, are specific to the location,  $x_m$ .

Darken derived his equations, based on the principles of conservation of mass (77). The premise of Darken's analysis is that the net vacancies, created by the diffusion of two species, remains at zero, relative to the fixed ends of the sample pair. According to Darken's equations, the flux of iron and carbon can be expressed as:

$$\text{Eq 12: } J_{Fe} = -D_{Fe} \frac{\partial c_{Fe}}{\partial x} \left[ 1 + \frac{c_{Fe}}{c_T} \right] + \frac{c_{Fe}}{c_T} D_C \frac{\partial c_C}{\partial x}$$

$$\text{Eq 13: } J_C = -D_C \frac{\partial c_C}{\partial x} \left[ 1 + \frac{c_C}{c_T} \right] + \frac{c_C}{c_T} D_{Fe} \frac{\partial c_{Fe}}{\partial x}$$

The net flux of vacancies is then equal to (76):

$$\text{Eq 14: } J_v = J_{Fe} + J_C = 0$$

Equations 12 and 13 are the counterparts of Fick's first law for diffusion, in a semi-infinite pair, when one species diffuses at a faster rate (77).

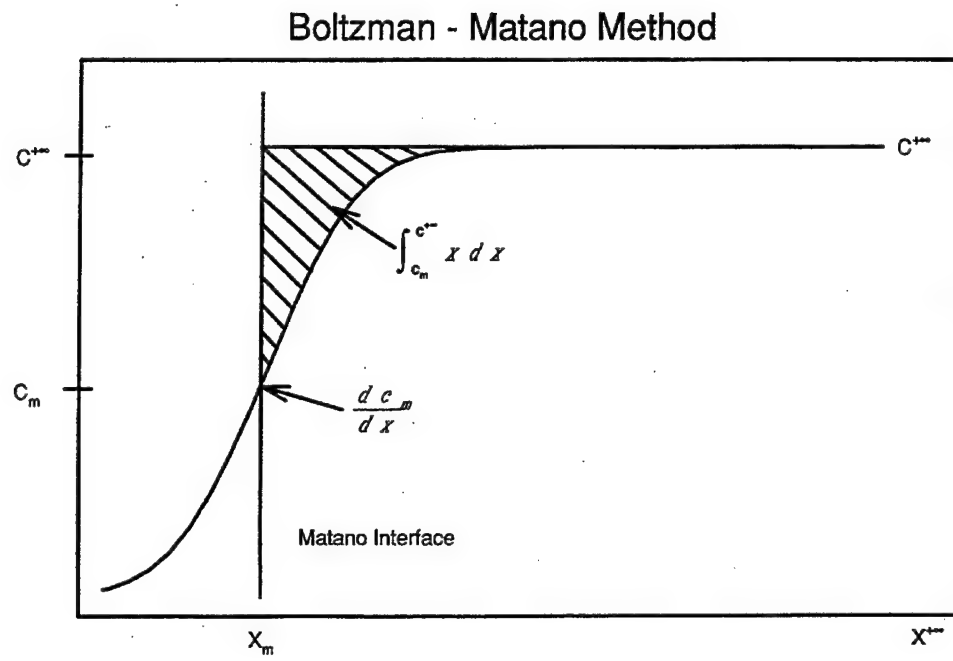


Figure 65. Boltzman-Matano method for calculating the diffusion coefficient.

The relationship of  $D_{Fe}$  to self-diffusion coefficient,  $D_{Fe}^*$ , is given by:

$$\text{Eq 15: } D_{Fe} = D_{Fe}^* \left[ 1 + \frac{d \ln \gamma_1}{d \ln (c_{Fe}/c_T)} \right]$$

Where  $D_{Fe}^*$  is determined by measuring the diffusion of iron isotopes in an iron matrix. The term,  $d \ln \lambda_1 / d \ln (c_{Fe}/c_T)$ , is a thermodynamic activity coefficient driven by some external force. Ions traveling in a potential field, atoms diffusing in a stress gradient, or atoms diffusing in a thermal gradient are examples of external forces fields (77, 78, 80). In the absence of external forces, the diffusion coefficient equals the self-diffusion coefficient. A similar expression also exists for  $D_C$ .

## 5.2 Boundary and Initial Conditions

While it is relatively straight forward to determine the diffusion term  $Dt$  from the experimental AES data, it is much more difficult to determine the actual diffusion coefficients  $D_{Fe}$  and  $D_C$ . The difficulty arises from wear in the bearing, which essentially makes it impossible to determine the initial conditions.

The effect of wear in the bearing contact is summarized in Fig. 66. For a diffusion profile to exist under dynamic conditions, requires that the Matano interface of iron travels at a velocity,  $v_m$ , equal to the wear rate,  $dw/dt$ . If  $v_m$  is less than  $dw/dt$ , the wear boundary will surpass the Matano interface over time. Under this scenario, a diffusion profile could still be detected in the bearing track, if the profile were generated post-test, while the bearing cooled to room temperature in a vapor rich atmosphere. For the Matano interface to travel faster than the wear boundary, requires an ever increasing diffusion coefficient,  $D_{Fe}$ , which physically is not possible.

Additional boundary conditions, which affect the diffusion rate are: stress gradients, temperature gradients,

and for VPD lubrication, chemical reaction rates. The nature of these boundary conditions is very complex. In the present analyses, their relative effects are investigated experimentally.

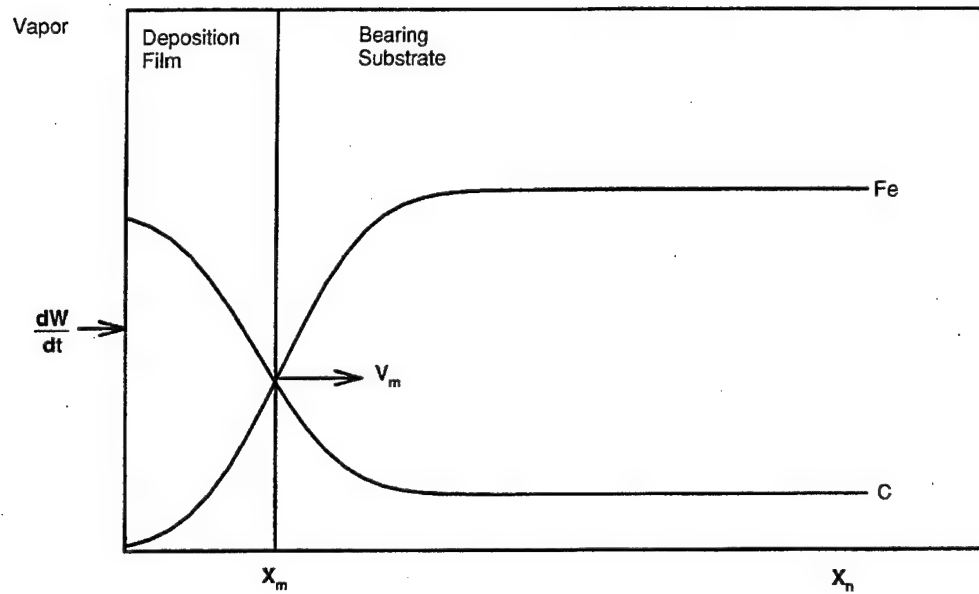


Figure 66. Wear at the bearing surface and its relationship to the Matano interface. For equilibrium under dynamic conditions,  $dw/dt = v_m$ .

### 5.3 Experimental Procedure

To gain further insight into the affect of boundary conditions on the diffusion mechanism(s), eight additional ball-on-rod tests were conducted. The additional tests are summarized in Table 14.

To separate the dynamic contribution from the post-test contribution, several tests were conducted where the bearings were quenched with liquid  $N_2$  after testing. The times listed in Table 14 refer to the length of exposure to the TBPP vapor, before quenching. During this period, the bearing was held at the test temperature, under static conditions. The induction heaters and vapor were terminated simultaneously, with the application of the liquid  $N_2$ . Thermocouple measurements of the bearing race indicate the race reached the boiling point of  $N_2$ , within 30 seconds of applying the liquid  $N_2$ , essentially stopping all thermally driven reactions.

To investigate the effect of suspected chemical reaction rates, an additional test was performed with the 5P4E lubricant, at the same conditions as the TBPP lubricant. Based on the results in Chapter 4, it was thought that the

phosphorous anions were involved in the accelerated diffusion of iron cations. In recent research performed by the Armstrong Medical Research Laboratory (81), a strong presence of inorganic phosphate as well as phenol by-products has been detected in the vapor decomposition products of the TBPP lubricant. The molecular structure of 5P4E, Fig. 15, suggests this molecule will decompose in the vapor phase, to form phenol by-products, without the presence of the phosphate ions. Differences between the diffusion profiles of TBPP and 5P4E are likely a result of cation diffusion involved with the TBPP organo-phosphate lubricant and the iron substrate.

Additional tests were also performed with different test durations, to evaluate the effect of test time on the diffusion process. These tests were also conducted at a higher bearing temperature, to measure the effect of temperature on the diffusion rate.



Table 14 - Additional Samples Generated for AES Depth Analysis

Sample Set	7	8	9	10	11	12	13	14
<u>Materials</u>								
Lubricant	TBPP	TBPP	5P4E	TBPP	TBPP	TBPP	TBPP	TBPP
<u>Test Condition</u>								
Bearing Temp (°C)	370	370	370	470	470	470	470	470
Lubricant Rate (ml/hr)	2.5	2.5	2.5	2.5	2.5	2.5	2.5	2.5
Test Duration (hr)	20	20	20	4	6	8	6	6
Liquid N <sub>2</sub> Quench (min)	0	20	No	No	No	No	0	5

## 5.4 Analytical Approach

A nonlinear regression of the experimental AES data was performed as the first step in the diffusion analyses. The data were fitted to Equations 3 and 4, using a Marquardt-Lenvenberg algorithm (82) and a commercial software package, Sigma Plot. In performing the regression analyses, the values of  $c^{+\infty}$ ,  $c^{-\infty}$ , and  $d$  were determined from inspection of the experimental data. The value for  $Dt$  was determined through iterations of the Marquardt-Lenvenberg algorithm. Separate analyses were performed for iron and carbon, for each sample set listed in Table 12, as well as for Sample Set 1.

A Boltzman-Matano analysis was also applied as a second approach, to determine  $Dt$  of iron from the data of Sample Set 1. The Boltzman method was applied at the Matano interface,  $x_m = 0$ . The diffusion term,  $Dt$ , was solved for by rearranging Equation 6 in the following form:

$$\text{Eq 16: } Dt = \frac{1}{2} \frac{dx}{dc} \Big|_{x_m=0} \int_0^{\infty} [c^{+\infty} - c_m] dx$$

The reciprocal of the concentration gradient was approximated by:

$$\text{Eq 17: } \frac{dx}{dc} \cong \frac{\Delta x}{\Delta c} \Big|_{x_m=0}$$

and the integral term was calculated by applying the trapezoid rule to the experimental data.

$$\text{Eq 18: } \int_0^{\infty} [c^{+\infty} - c_m] dx \cong c^{+\infty} x_n - \sum_{j=1}^n \frac{x_j - x_{j-1}}{2} [c_j + c_{j-1}]$$

where;

$$\text{Eq 19: } \lim_{x \rightarrow x_n} c_n = c^{+\infty}$$

To solve for the intrinsic diffusion coefficients,  $D_{Fe}$  and  $D_C$ , requires a solution of three unknowns;  $D_{Fe}$ ,  $D_C$ , and  $t$ . Unfortunately, Darken's analysis only provides two equations for the three unknowns. To overcome this obstacle, the following approach was taken:

1. Assume that the Matano interface for iron travels at a velocity equal to the bearing wear rate. This assumption is a necessity for equilibrium under dynamic conditions, as previously discussed.
2. Evaluate Equations 9 and 10 for different ratios of  $K = D_C/D_{Fe}$  from  $K = 0$  to  $K = 1.0$ . Where  $K = 0$  represents the extreme value  $D_C \ll D_{Fe}$ , and  $K = 1.0$  represents the opposite extreme,  $D_C = D_{Fe}$ .

Using this approach, Eq. 9 can be rearranged to determine  $D_{Fe}$  at the Matano interface:

$$\text{Eq 20: } D_{Fe} = \frac{v_m c_T}{\frac{\partial c_{Fe}}{\partial x} + K \frac{\partial c_C}{\partial x}} \Big|_{x=x_m=0}$$

The "age" of the reaction film can be obtained by rearranging Eq. 10:

$$\text{Eq 21: } t = \frac{D_{Fe}}{\frac{c_T}{c_T} [c_C + K c_{Fe}]} \Big|_{x=x_m=0}$$

The minimum value of  $D_{Fe}$  and the maximum value of  $t$  for diffusion, under dynamic conditions, are obtained in the limit where  $K = 0$ .

As a check of the validity of the analytical approach, the flux of iron, carbon, and vacancies were calculated using Eqs. 12-14.

Additionally, the self-diffusion coefficient for iron was calculated as an estimate of the external forces involved in the diffusion process. For isothermal conditions, the self-diffusion coefficient follows an Arrhenius relationship (83):

$$\text{Eq 22: } D^* = D_0 \exp\left(\frac{-E}{RT_K}\right)$$

Values used in the calculation of the self-diffusion coefficient for BCC iron are:  $D_0 = 2.0 \text{ cm}^2/\text{s}$  and  $E = 239 \text{ kJ/mol}$  (84).

## 5.5 Experimental Results

AES depth profiles from Sample Sets 7 and 8 are shown in Figs. 67 (a-b). The specimens in Sample Set 7 were immediately quenched in liquid  $N_2$  and the specimens in Sample Set 8 were quenched, after an additional 20 minutes at test temperature, under static conditions. The profiles obtained on Sample Set 7 indicate that diffusion occurs under dynamic conditions. In comparing Fig. 67 (a) with Fig. 67 (b), there is no appreciable difference between the two, indicating that dynamic conditions, i.e., stress cycles, have a dominant effect in generating the diffusion profiles. The diffusion profiles shown in Figs. 67 (a,b) are also very similar to the diffusion profile of Sample Set 1, previously shown in Fig. 48. The test temperatures for all three sample sets were maintained at 370°C. However, the bearing run times, 96 hours for Sample Set 1 and 20 hours for Sample Sets 7 and 8, are very different. This indicates that the diffusion profile of iron maintains equilibrium with the wear boundary under dynamic conditions, and the Matano interface travels at a velocity equal to the wear rate.

The AES depth profile for the 5P4E deposition film in the bearing track is shown in Fig. 68. The 5P4E lubricant indicates substantial levels of oxygen in the deposition film. The results also indicate that oxygen diffuses in a similar fashion as carbon does with the TBPP lubricant. Although the film is predominately composed of iron and oxygen, there is a thin layer of carbon, approximately 4 nm thick, at the bearing surface. In the Raman analysis, it was shown that oxygen is present in the VPD film as  $\text{Fe}_2\text{O}_3$  and  $\text{Fe}_3\text{O}_4$ . This further supports that the TBPP lubricant serves as an oxidation inhibitor, since Sample Sets 7 and 8 were also conducted at the 370°C bearing temperature for a 20-hour test period.

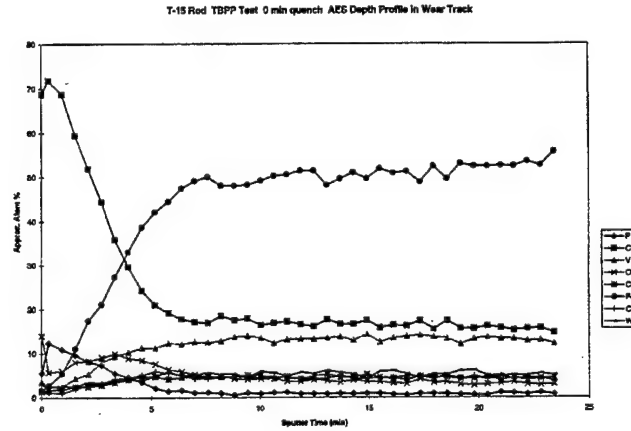
The AES depth profiles for Sample Sets 10-12 are shown in Figs. 69 (a-c). The samples were generated at test conditions of 430°C, for 4-, 6-, and 8-hour test durations, respectively. The diffusion profiles are similar for all three conditions, further supporting that the diffusion profile is maintained under dynamic conditions, regardless of the operating time. Although all of the tests at 430°C are similar, they are different than results obtained at 370°C. Specifically, the slope of the diffusion profile at 430°C is

higher than the slope obtained at 370°C, i.e.,  $Dt(T = 430^\circ\text{C}) < Dt(T = 370^\circ\text{C})$ . This is opposite of the trend expected for diffusion, which is normally driven exponentially by temperature, as previously shown in Equation 22. In addition to lower values of  $Dt$  at 430°C, the depth below the bearing surface to the Matano interface is also less. This is likely a result of the increased wear rates at higher temperatures.

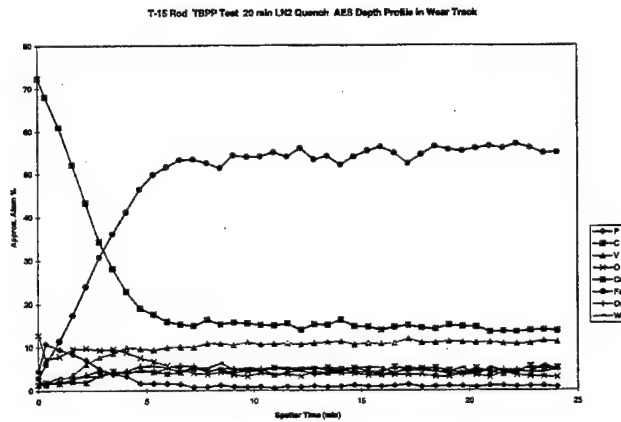
This decreases  $t$  in the  $Dt$  term, which provides some explanation as to why  $Dt(t = 430^\circ\text{C}) < Dt(t = 370^\circ\text{C})$ .

The AES depth profiles for Sample Sets 13 and 14 are shown in Fig. 70 (a,b), respectively. Again, the results are similar to other results at equivalent bearing temperatures, and the post-test contribution of the deposition film is negligible compared to the film generated under dynamic conditions. A photograph of the bearing specimens from Sample Set 14, approximately 30 minutes after the liquid  $N_2$  quench, are shown in Fig. 71. The white coating on the specimens is frost. The cooling rate for Sample Set 14, upon administering the liquid  $N_2$ , is shown in Fig. 72.





(a)



(b)

Figure 67. AES depth profiles for TBPP deposition films at 370°C obtained in the bearing track: (a) Sample Set 7, immediate quench in liquid N<sub>2</sub>, and (b) Sample Set 8, liquid N<sub>2</sub> quench after 20 additional minutes at 370°C and static conditions.

T-15 Rod 5P4E Test 2R2VP21900VT530 AES Depth Profile on Wear Track

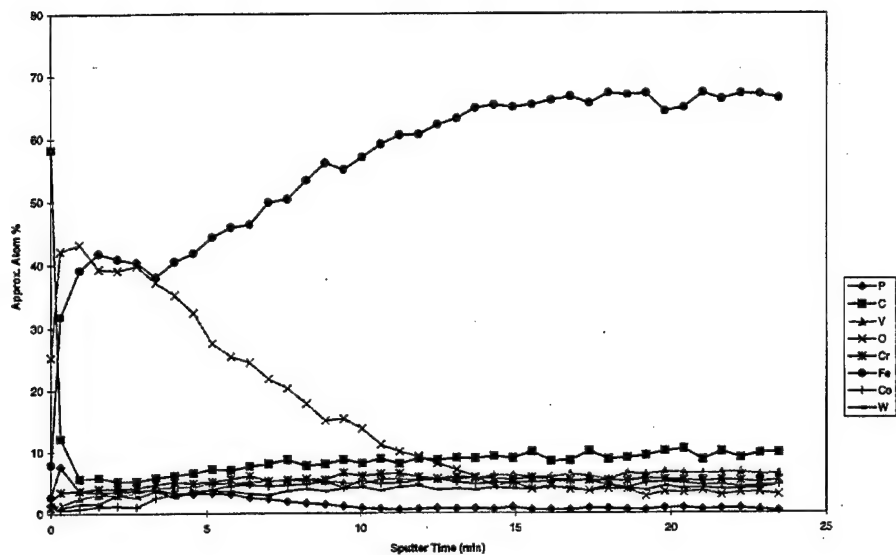
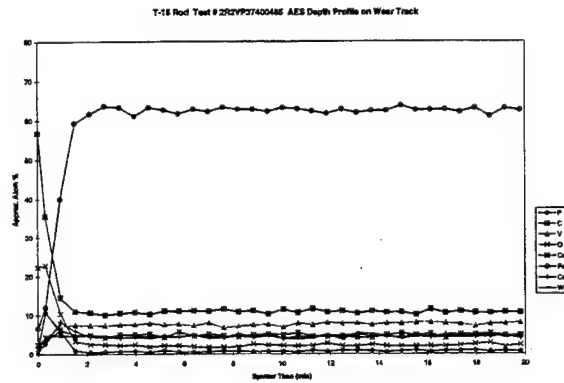
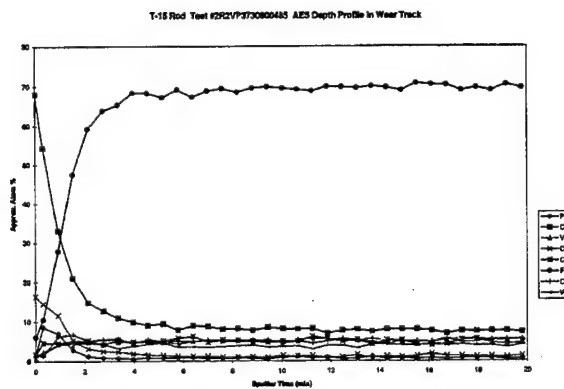


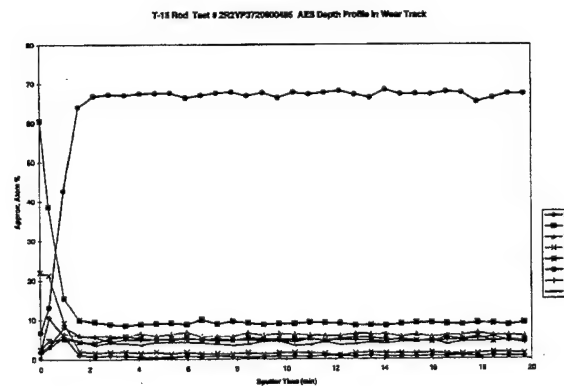
Figure 68. AES depth profile of 5P4E deposition film inside of the bearing track.



(a)



(b)



(c)

Figure 69. AES depth profiles for the TBPP lubricant at 430°C: (a) after 4-hour test; (b) after 6-hour test; and (c) after 8-hour test.

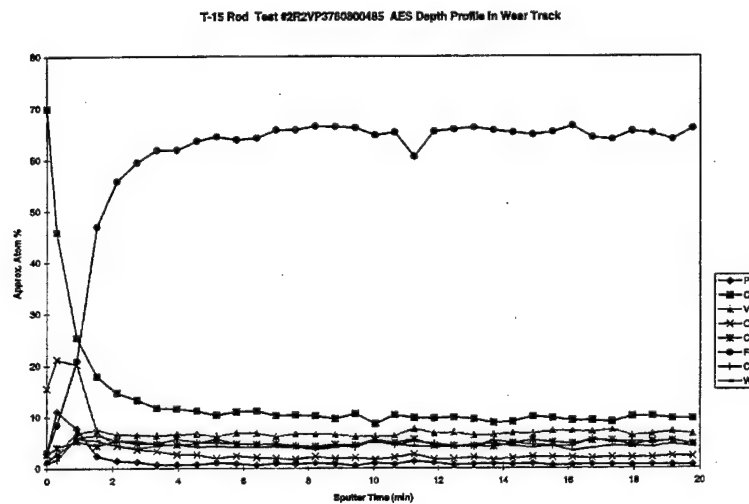
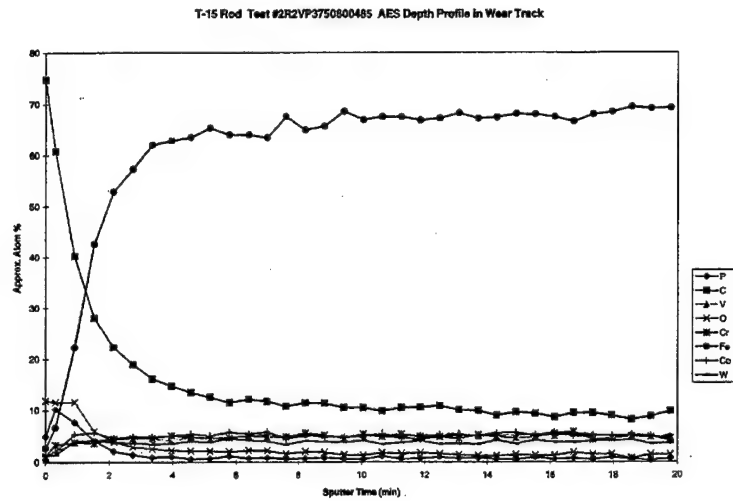


Figure 70. AES depth profile at 430°C: (a) 6-hour test followed by immediate quench in liquid N<sub>2</sub>; (b) 6-hour test followed by 5 minutes under static conditions, followed by liquid N<sub>2</sub> quench.

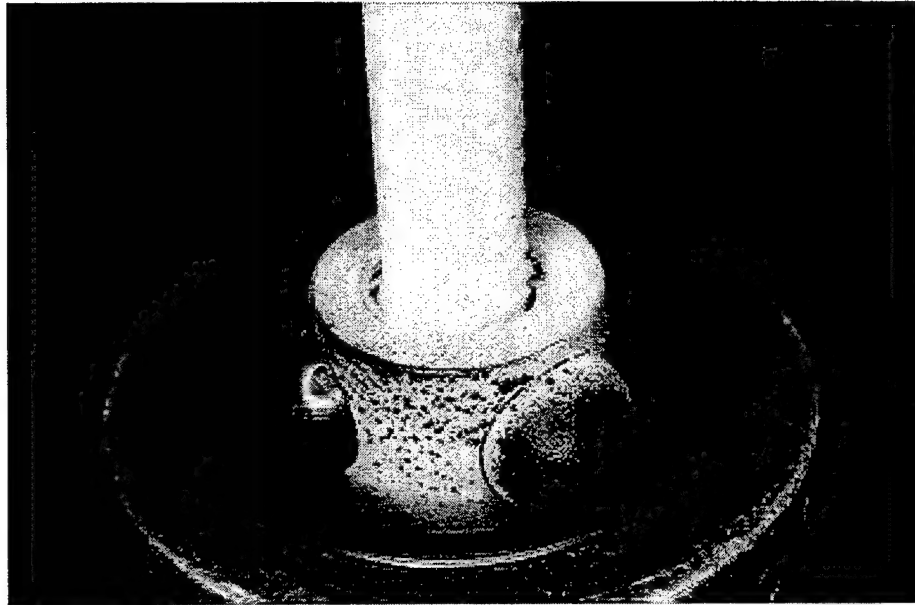


Figure 71. Bearing specimens from Sample Set 14  
approximately 30 minutes after liquid N<sub>2</sub> quench.

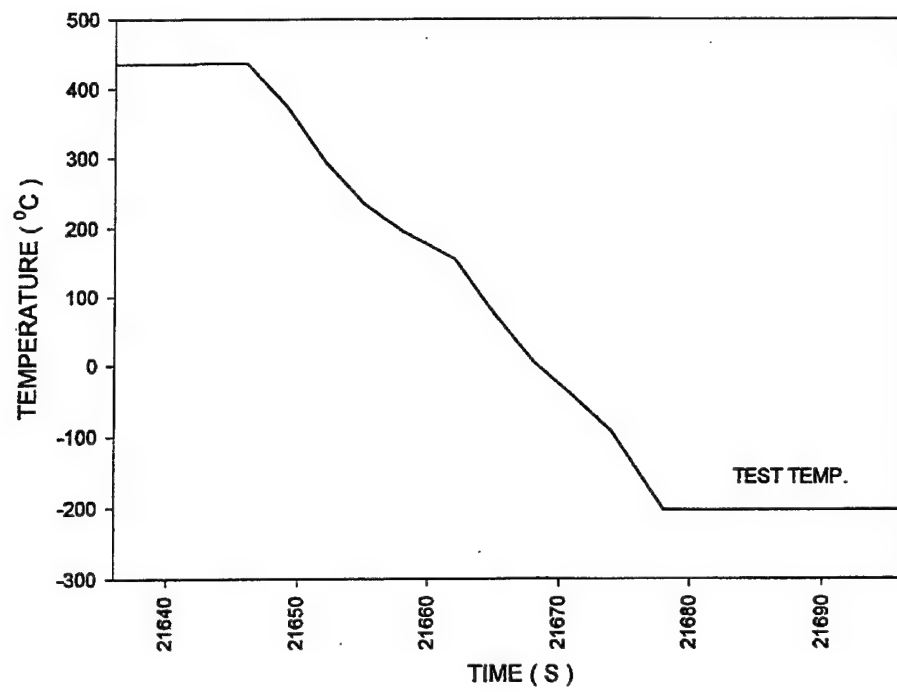


Figure 72. Cooling rate of the bearing specimens with liquid  $N_2$  quench.

## 5.6 Analytical Results

Results of the nonlinear regression for TBPP deposition films are shown in Fig. 73. In general, Equations 3 and 4 provide an excellent fit to the experimental AES data. The coordinate system shown in Fig. 73 was taken relative to the bearing surface for ease in handling the AES data. This was accomplished by setting  $x = x - d_{Fe}$  for the iron diffusion profile, and  $x = x - d_c$  for the carbon diffusion profile. A sample program for calculating the diffusion terms is listed in Appendix B.

The Boltzman-Matano analysis for Sample Set 1 gives a value of  $Dt_{Fe}$  equal to  $107.5 \text{ nm}^2$ . This compares favorably to the value of  $106.8 \text{ nm}^2$ , calculated in the nonlinear regression analyses. For simplicity, the regression values for  $Dt$  were used to calculate the concentrations and their respective gradients in Darken's analysis. The values are listed in Table 15. This approach is justified, based on the quality of the experimental fit and the close approximation of  $Dt$  calculated by the Boltzman-Matano methods. The exact procedure for calculating  $Dt$  via the Boltzman-Matano method, as well as the procedure used to determine  $D_{Fe}$ , are listed in Appendix C.

Results from Darken's analysis for  $K = 0$  to  $K = 1.0$  are summarized in Table 16. In general, the diffusion coefficient for iron was of the order of  $1 \text{ nm}^2/\text{s}$ , regardless of the test condition or the value of  $K$  imposed on Equation 20. The values of the "age" of the deposition film are of the order of 0 to several hundred seconds, depending on the test condition and the value of  $K$ . Based on the wear rate, these values seem reasonable. For example, consider Sample Set 1, where  $\Delta w/\Delta t = 0.0167 \text{ nm/s}$ . This implies that the wear will surpass the Matano interface for iron,  $d_{\text{Fe}} = 32 \text{ nm}$ , in 1916 seconds. Therefore, the "age" of the deposition film must be less than this value. At  $K = 0$  for Sample Set 1,  $t = 387 \text{ s}$ . The  $430^\circ\text{C}$  test temperature produced higher wear rates and smaller values of  $d_{\text{Fe}}$ . Under these conditions, a lower value for the "age" of the deposition film is expected. This trend is seen in the analytical results.

It is interesting to note that for most of the samples listed in Table 16, stable diffusion coefficients are obtained at  $K = 1.0$ . This implies that the Matano interface for iron can still travel at the wear rate,  $\Delta w/\Delta t$ , even though  $D_{\text{Fe}}$  is equal to  $D_{\text{c}}$ . The reason for this anomaly is



shown in Fig. 74. For  $K = 1.0$ , the denominator of Equation 20 is simply the sum of the concentration gradients given by Equations 4 and 5. This sum is related to the flux of vacancies, with regards to the coordinate system traveling with the Matano interface. The Matano interface is able to travel at the imposed wear rate because the sum of the concentration gradient at  $d_{Fe}$  does not go to zero for most of the samples, until  $K$  values slightly larger than 1.0. For Sample Set 1, this occurs at  $K = 1.3$ , where . If the flux of phosphorus and oxygen had been included in the diffusion analyses, the value of  $K$  where would be lower as some of the vacancies are also filled by these elements.

The flux of iron and carbon for Sample Set 1,  $K = 0.10$ , is show in Fig. 75. The flux values were calculated using Equations 12 and 13. As required by Darken's premise of conservation of mass, the net flux of vacancies goes to zero, if expressed in a coordinate system, referenced to the fixed ends of the sample pair.

The self-diffusion coefficients for iron at 370°C and 430°C are  $7.68 \times 10^{-24} \text{ nm}^2/\text{s}$  and  $3.48 \times 10^{-22} \text{ nm}^2/\text{s}$ ,

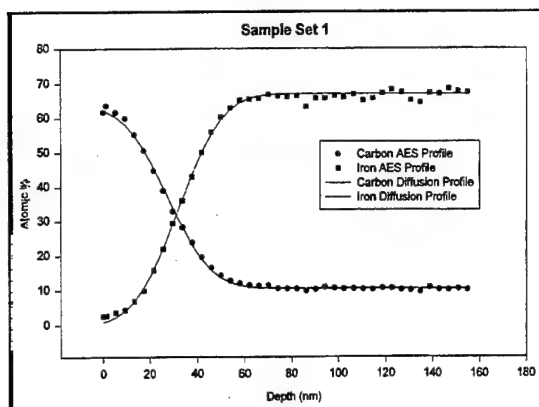
respectively. These values are significantly lower than the diffusion coefficients shown in Table 16. This implies that significant thermodynamic forces are present, consistent with the expressions of Equation 15.

Table 15 - Regression Results for Dt in the Bearing Track

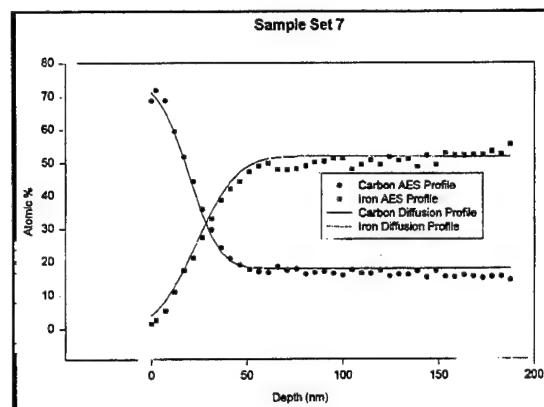
Sample Set	1	7	8	10	11	12	13	14
<u>Iron</u>								
$c^{+\infty}$	67.0	52.0	55.0	67.0	69.0	62.0	65.0	65.0
$c^{-\infty}$	0.0	0.0	2.0	4.0	2.0	4.0	2.0	2.0
d	32.0	24.0	23.6	6.4	8.8	6.4	10.4	9.6
Dt	106.8	141.1	123.8	6.3	22.3	6.3	21.6	13.8
<u>Carbon</u>								
$c^{+\infty}$	10.5	18.0	15.3	9.0	8.5	10.8	10.7	10.1
$c^{-\infty}$	63.0	74.0	75.0	80.0	75.0	70.0	90.0	80.0
d	27.5	20.0	16.4	2.0	6.4	3.0	6.4	3.0
Dt	101.4	76.2	79.5	6.6	21.6	6.5	60.5	12.1
Run Time (hrs)	96	20	20	4	6	8	6	6

Table 16 - Results of Darken's Analysis for  $0 \leq K = D_C/D_{Fe} \leq 1.0$

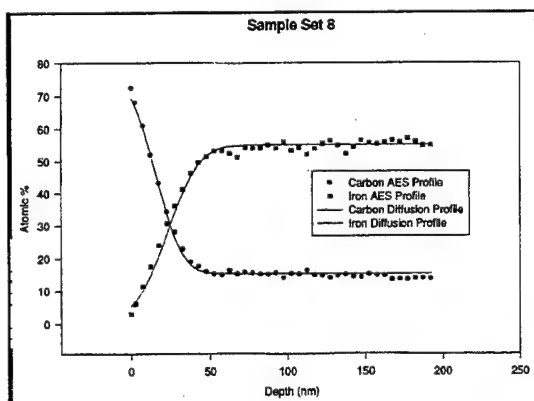
Sample Set	1	7	8	10	11	12	13	14
$\Delta w/\Delta t$ (nm/sec)	0.0167	0.0278	0.0257	0.0785	0.0565	0.0465	0.0810	0.0833
$D_{Fe}$								
K=0.0	0.58	1.46	1.12	0.53	0.91	0.35	1.47	0.86
K=0.1	0.63	1.70	1.25	0.55	1.01	0.37	1.58	0.90
K=0.5	0.94	4.79	2.56	0.70	1.69	0.50	2.23	1.11
K=1.0	2.47	-	-	1.05	10.9	10.88	4.62	1.57
$t(s)$								
K=0.0	387	161	203	36	50	45	27	44
K=0.1	322	130	166	28	41	37	23	36
K=0.5	154	37	62	13	17	18	12	18
K=1.0	43	-	-	6	2	7	5	9



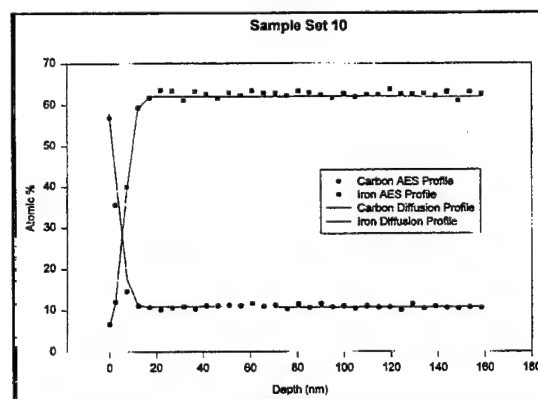
(a)



(b)

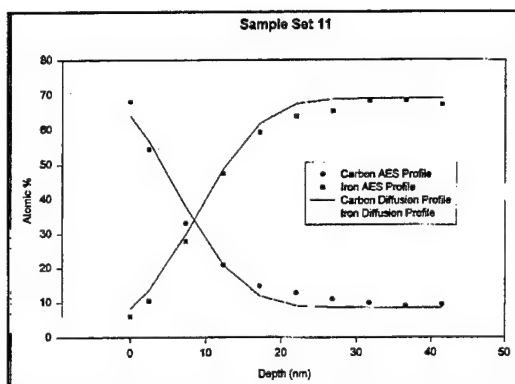


(c)

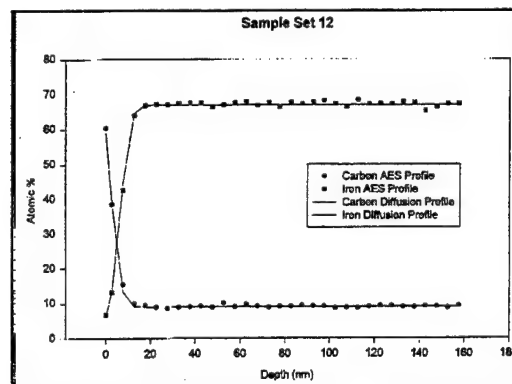


(d)

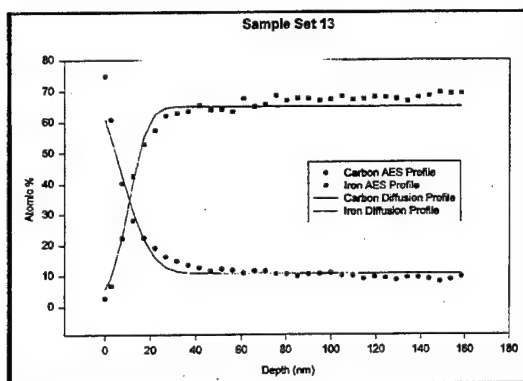
Figure 73. Comparison of regression fits for  $Dt$  with the experimental AES data.



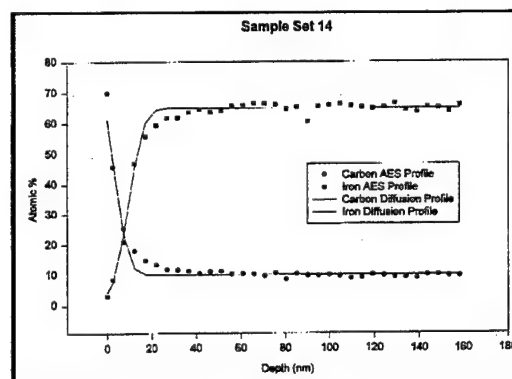
(e)



(f)



(g)



(h)

Figure 73 (Continued). Comparison of regression fits for  $Dt$  with the experimental AES data.

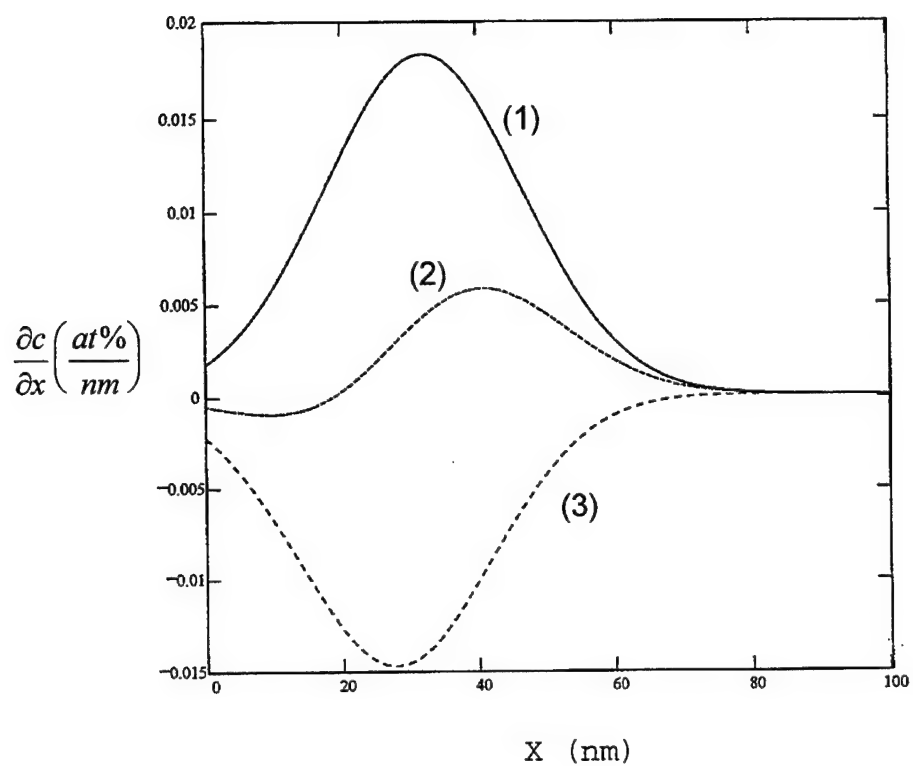


Figure 74. (1) Concentration gradient for iron,  $\frac{\partial c_{Fe}}{\partial x}$ ; (2) concentration gradient for carbon,  $\frac{\partial c_C}{\partial x}$ ; and (3) sum of the concentration gradients,  $\frac{\partial c_{Fe}}{\partial x} + \frac{\partial c_C}{\partial x}$ .

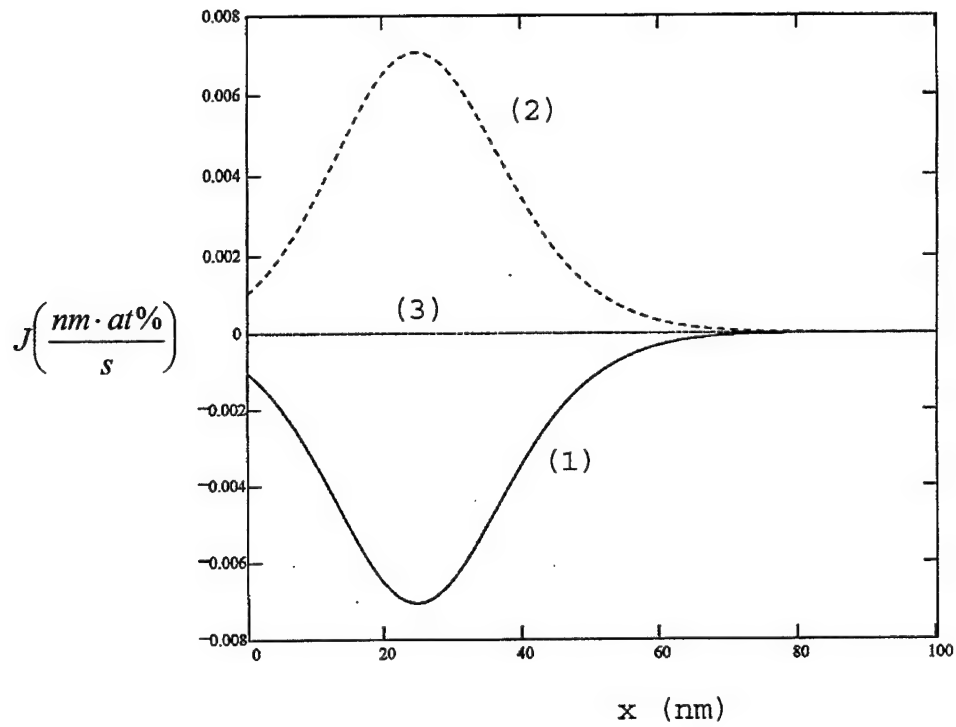


Figure 75. Flux relative to the fixed-end coordinate system:  
 (1) flux of iron,  $J_{\text{Fe}}$ ; (2) flux of carbon,  $J_{\text{C}}$ ; (3) flux of  
 vacancies,  $J_{\text{V}}$ .



## 5.7 Discussion

The diffusion profiles for iron and carbon in VPD films, generated with the TBPP lubricant, can be analyzed using the semi-infinite solution. The diffusion coefficient for iron is of the order of magnitude of  $1 \text{ nm}^2/\text{s}$ . This order of magnitude is six times larger than the self-diffusion coefficient for BCC iron at  $370^\circ\text{C}$ . An even lower self-diffusion coefficient is expected in T15 bearing steel, due to the alloying constituents. Specifically, chromium, tungsten, and vanadium, all have a significant affect on lowering the self-diffusion coefficient in alloyed steel (85). The relatively high diffusion coefficients for iron, indicate that substantial forces are involved in the diffusion process.

Diffusion profiles obtained on specimens immediately quenched in liquid  $\text{N}_2$  are essentially the same as diffusion profiles obtained on specimens quenched after several minutes of additional exposure in a vapor rich atmosphere under static conditions. This result indicates that dynamic effects have a substantial affect on the magnitude of the diffusion coefficient for iron. The most likely explanation

is the significant stress gradients, which exist in the subsurface of the bearing contact (45). Elastic stress gradients act as potential gradients in the flux of atoms (80).

All of the samples generated for a given temperature have similar profiles, regardless of the time of operation of the bearing. This result indicates that the Matano interface travels at a fixed distance from the bearing surface and the velocity of the Matano interface is equal to the bearing wear rate. The self-diffusion coefficient for iron at 430°C is approximately two orders of magnitude larger than the self-diffusion coefficient at 370°C. However, in all cases the diffusion terms,  $Dt$ , calculated for the deposition films were lower at 430°C than values obtained at 370°C. This anomaly can, at least, partly be explained by the higher wear rates at elevated temperatures. A higher wear rate effectively reduces the "age" of the deposition film, in turn reducing the  $Dt$  term by reducing  $t$ . Additionally, the modulus of elasticity and Poisson's ratio remain relatively unchanged in the temperature range of 370°C to 430°C. This infers that the stress gradients also remain unchanged for a given load and geometry over a fairly wide temperature range. If the

diffusion coefficient  $D_{Fe}$  is substantially driven by stress gradients, then increasing the temperature will have little effect on increasing the value of  $Dt$ .

Diffusion profiles for VPD films produced with the TBPP lubricant are different than the profile obtained with the 5P4E lubricant for equivalent test conditions. With the TBPP lubricant, the primary elements undergoing diffusion are iron and carbon; with the 5P4E lubricant, the primary elements undergoing diffusion are iron and oxygen. In both cases, the subsurface stress gradients are essentially the same, which explains the diffusion of iron from the substrate. At the boundary between the vapor and deposition film, the diffusion mechanisms are different, suggesting that the lubricant chemistry also plays an active role in the surface diffusion. Cation diffusion is thought to be the contributing factor for both lubricants. With the TBPP deposition film the reacting ions include;  $PO_4^{3-}$ ,  $HPO_3^{2-}$ , and phosphorus anions. For 5P4E, the reacting anions are  $O^{2-}$ . Carbon diffuses in the TBPP deposition film, due to crosslinking of the of the phosphate structure, which immobilizes a substantial amount of the phosphorus. Oxygen is not bound by this constraint in the 5P4E deposition film and is free to travel in a similar

manner as carbon does in the TBPP deposition film. It is also known, that the diffusion of  $\text{Fe}^{2+}$  cations is greatly facilitated by nonstoichiometric ionic structures (86). For example, the presence of  $\text{Fe}^{3+}$ , or phosphate mixed with phosphite and phosphide anions, necessarily creates holes, which supply additional sites for the vacancy diffusion mechanism. Examples of this phenomena are cited in the formation of iron oxide and FeS films (86).

While diffusion has not been identified as a mechanism involved in VPD lubrication or boundary film lubrication with phosphorus additives in previous efforts, critical aspects of the cation diffusion mechanism are supported by prior research of Klaus, et al. (68), and Tung, et al. (87). Specifically, there are three criteria considered necessary for a stable cation diffusion film:

1. For a stable film to exist, it is a requirement that the composition vary throughout the film (88). In the oxidation of iron, this is normally achieved with three layers of iron oxides;  $\text{FeO}$ ,  $\text{Fe}_3\text{O}_4$ , and  $\text{Fe}_2\text{O}_3$  (88). This is analogous to the results found by Klaus on iron foils exposed to TCP vapor, under static conditions

(68). Klaus found that  $\text{FePO}_4$  exists at the vapor boundary,  $\text{Fe}_2\text{P}$  and  $\text{Fe}_5\text{C}_2$  in the intermediate layer, and  $\text{Fe}_3\text{P}$  and  $\text{Fe}_3\text{C}$  at the substrate boundary.

2. Additionally, for cation diffusion to occur, electron transfer must also occur. Tung, et al., (87) has shown that an aryl phosphate ester, dilauryl hydrogen phosphate, can be electrodeposited on iron piston rings. AES depth profiles of the electrodeposited films grown by Tung, et al., are similar to the profiles obtained with the TBPP lubricant. Tung proposed that hydrogen ions serve as the receptor for electrons in the oxidation/reduction reaction. The decomposition of the vapor lubricants to form amorphous carbon indicates that at some point in the vapor deposition reactions, there was an ample supply of hydrogen ions.

3. Additionally, Klaus, et al., (73) have found that deposition rates, produced by TCP vapor on 316 stainless steel, progress rapidly at first and decrease with time. Klaus attributed this to a catalytic effect

between iron and the TCP vapor. Klaus' graphs, depicting the amount of deposit vs. time, are also parabolic in nature. This is consistent with the results expected for cation diffusion (88), as the iron cations have increased difficulty in reaching the anions, to balance the electric charge in thicker films. Klaus also found that deposition films generated with TCP vapor and quartz did not possess this property, and grew in a near linear fashion (68).

In summary, the diffusion mechanisms involved in the formation of a VPD film in the bearing track appears to be a two-step process. Elastic stress gradients supply the initial flux of iron atoms toward the bearing surface; as the atoms approach the surface, electro-chemical reactions produce the actual deposition film.

## CHAPTER 6

### HIGH SPEED BEARING TESTS

The TBPP, TBPP/TBP, and X-1P lubricants were selected as the candidate lubricants based on tests results generated in Chapters 2 and 3. The objective of the experiment was to achieve stable operation of rolling element bearings, operating at bearing temperatures up to 500°C, speeds up to 1.3 MDN, and applied thrust loads up to 1800 N. The maximum bearing temperature and thrust load were dictated by the limits of the High Speed Bearing Tester.

## 6.1 Test Apparatus and Procedure

A cross section of the High Speed Bearing Tester is shown in Fig. 76. The test bearing is mounted on a shaft, driven by an integral air turbine. The rotational speed of the bearing is controlled by varying the air pressure to the air turbine.

The bearing environment was heated by three 1000 watt band heaters, and eight 250 watt cartridge heaters. A thermocouple, mounted to the axial face of the bearing outer race, was used to measure the bearing temperature. Two additional thermocouples were used to control the environmental temperature. Locations of the thermocouples are shown in Fig. 76. The bearing was heated under static conditions, prior to starting the test, to obtain the desired test temperature. The lubricant delivery air was started 40 minutes, prior to test, to mitigate the effect of the delivery air on the initial bearing temperature. The lubricant was added to the delivery air, approximately 10 minutes prior to test.

Thrust load was applied to the bearing through an annulus containing the bearing outer race. Rotation of the



annulus was restricted by a moment arm connected to a load transducer. The applied moment, transferred from the outer race to the load transducer, was used to calculate the bearing torque. The mass of the annulus is 2.39 kg, which contributes a 23.4 N radial load to the bearing. Additionally, vibration of the annulus contributes dynamic forces and applied moments to the bearing, which are not accounted for in the reported bearing loads.

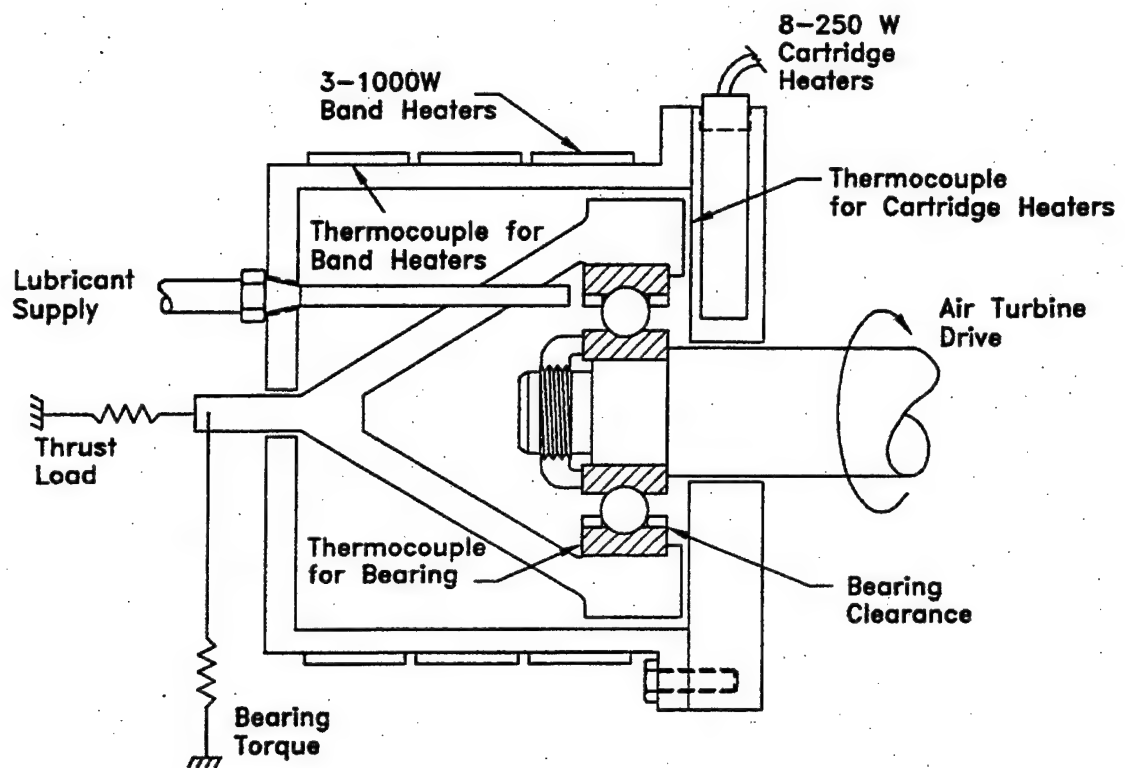


Figure 76. Cross section of the High Speed Bearing Tester

## 6.2 Lubricant Delivery

In the initial high speed bearing tests, the candidate lubricants were supplied to the bearing, using the vapor delivery system described in Chapter 2. The lubricants were delivered at a rate of 5 ml/hr, in an air stream flowing at 283 l/hr. The delivery air temperature was maintained at 325°C for all of the vapor lubrication tests.

Additionally, bearing tests were performed with the candidate lubricants delivered as oil-mists. In these tests, the candidate lubricants were supplied at a rate of 13 ml/hr, in an air stream flowing at 400 l/hr. These delivery rates were arbitrarily chosen based on rates previously used with a 3 cSt polyol-ester lubricant, during test rig checkout. At room temperature, the TBPP and X-1P lubricants proved difficult to mist, due to lubricant viscosity. To overcome this problem, the lubricants were heated to 100°C, prior to misting. The room temperature viscosity of the TBPP/TBP lubricant was sufficiently low to generate an oil-mist without heating the lubricant. Viscosities of the test lubricants at 100°C are listed in Table 7. The delivery air in the oil-mist tests was not preheated. Consequently, the

lubricant/air mixture entering the bearing in the oil-mist tests was approximately 300°C cooler than the mixture used in the vapor phase lubrication tests.

### **6.3 Bearing Geometry, Cage Selection, and Material Properties**

The internal geometry of the test bearings is summarized in Table 17. The bearing envelope geometry conforms to the AFBMA standard for 206 size bearings. The bearings were machined to an ABEC 5 tolerance, which is considered a precision class ball bearing. T15 tool steel was selected as the bearing race material, based on the results discussed in Chapters 2 and 3. Some of the T15 bearings were coated with thin dense chrome (TDC), to potentially address oxidation of the steel at elevated temperatures. The rolling elements were made from NBD 200  $\text{Si}_3\text{N}_4$  ceramic. The lower density of  $\text{Si}_3\text{N}_4$  presents significant advantages in reducing inertial forces in high speed bearings. Material properties for T15 tool steel and NBD 200  $\text{Si}_3\text{N}_4$  ceramic are listed in Table 18.

Outer-land riding, silver plated AISI 4340 cages were used in the vapor delivery tests. However, this approach led

to significant wear at the cage-land surfaces when the bearing speed exceeded 0.9 MDN. Initially, wear of the cage-land was attributed to loss of the cage diametral clearance. As an alternative solution, inner-land riding, silver plated 4340 cages were evaluated in the vapor lubrication tests. However, significant wear at the cage-land surface still occurred.

As a third option, outer-land riding cages were fabricated from a carbon matrix, carbon fiber composite (C-C). The C-C composite was initially prepared as a tube 15 cm long, with fibers oriented in the axial and circumferential direction. Cages were then machined to the final dimensions from sections of the tube and redensified, using a chemical vapor infiltration process. Depending on processing and heat treatment temperatures (89), C-C composites tend to produce graphitic structures, with the basal plane oriented along the fiber axis (90). This feature provides self-lubricating properties at the land surfaces, with the fiber orientation described above. However, unlike most self-lubricating materials, C-C composites produce low amounts of wear under sliding conditions (91). Maintaining low wear rates is critical in high speed bearing cages, to maintain balance and

critical dimensions. The C-C cages were introduced in the test matrix simultaneously with the introduction of the oil-mist delivery. The objective of both additions was to reduce wear at the cage-land surface, while increasing the bearing speed to values above 1 MDN. These are the first known tests to evaluate C-C cages in rolling element bearings.

Material properties of the C-C composite and AISI 4340 steel are listed in Table 18. The lower density of C-C composite is particularly beneficial in high speed bearings to reduce inertial and dynamic collision forces. To compensate for the lower strength and lower elastic moduli of the C-C composite, the cage width was increased and two balls were removed from the ball complement.

---

Table 17. - Test Bearing Geometry

---

Class: 206, ABEC 5, Outer Land Guided Cage

Contact Angle	24°
Outer Race Curvature	0.515
Inner Race Curvature	0.527
Pitch Diameter (m)	$4.618 \times 10^{-2}$
Radial Clearance (m)	$6.10 \times 10^{-5}$
End Play (m)	$3.05 \times 10^{-4}$
Ball Diameter (m)	$9.52 \times 10^{-3}$
Cage Land Clearance (m)	$2.54 \times 10^{-4}$
Cage Width (m)	
4340	$1.45 \times 10^{-2}$
C-C	$1.60 \times 10^{-2}$
No. of Balls	
4340	13
C-C	11

---

Table 18. - Bearing Material Properties at 500°C

Material Direction	4340	C-C $\theta, x$	C-C $r$	T15	Si <sub>3</sub> N <sub>4</sub>
Yield Strength (Mpa)	500	310	5	1300	NA*
Elastic Modulus (Gpa)	170	100	13	175	320
Poisson's Ratio	0.30	0.05	NA*	0.29	0.26
Coeff. of Thermal Expansion ( $\mu\text{m}/^\circ\text{C}$ )	15.0	0	0	11.0	2.9
Thermal Conductivity (w/m.k)	34	30	5	25	21
Density ( $\text{kg}/\text{m}^3$ )	7750		1600	8190	3160

\* Not available.



#### 6.4 Vapor Delivery Test Results

Results, from a vapor lubricant delivery test are shown in Fig. 77. After a period of 2 hours, the bearing obtained steady-state conditions, with a mean bearing torque value of 0.08 N-m. The temperature rise in the bearing, from static conditions to steady-state conditions at 30,000 rpm, was 130°C. A total of 18.3 hours of operation was accumulated on the bearing over six consecutive tests. This was the longest and most successful of the vapor delivery tests. At bearing speeds above 30,000 rpm, vapor lubricated bearings demonstrated short periods of stable operation, followed by an abrupt rise in bearing torque. Post-test inspection always showed significant wear at the cage-land interface for both outer-land and inner-land riding cages. At speeds below 1 MDN, moderate wear was found in the cage-land contact. A photograph of the cage, from the vapor lubrication test described above, is shown in Fig. 78. The silver plating is oxidized on the noncontacting surfaces. EDS analysis of the cage indicated that the silver plating was removed from the cage-land surface.

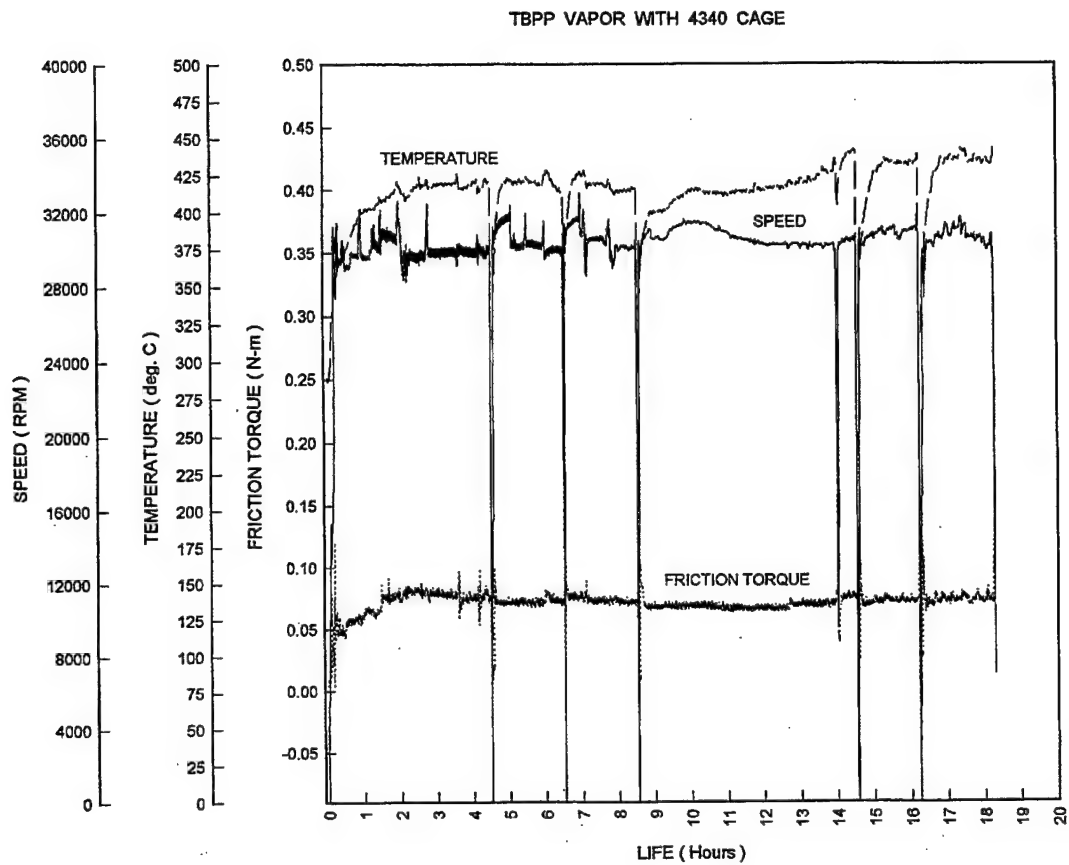


Figure 77. TBPP vapor delivery test. Test conditions:  
silver plated 4340 cage; 445 N applied thrust load.

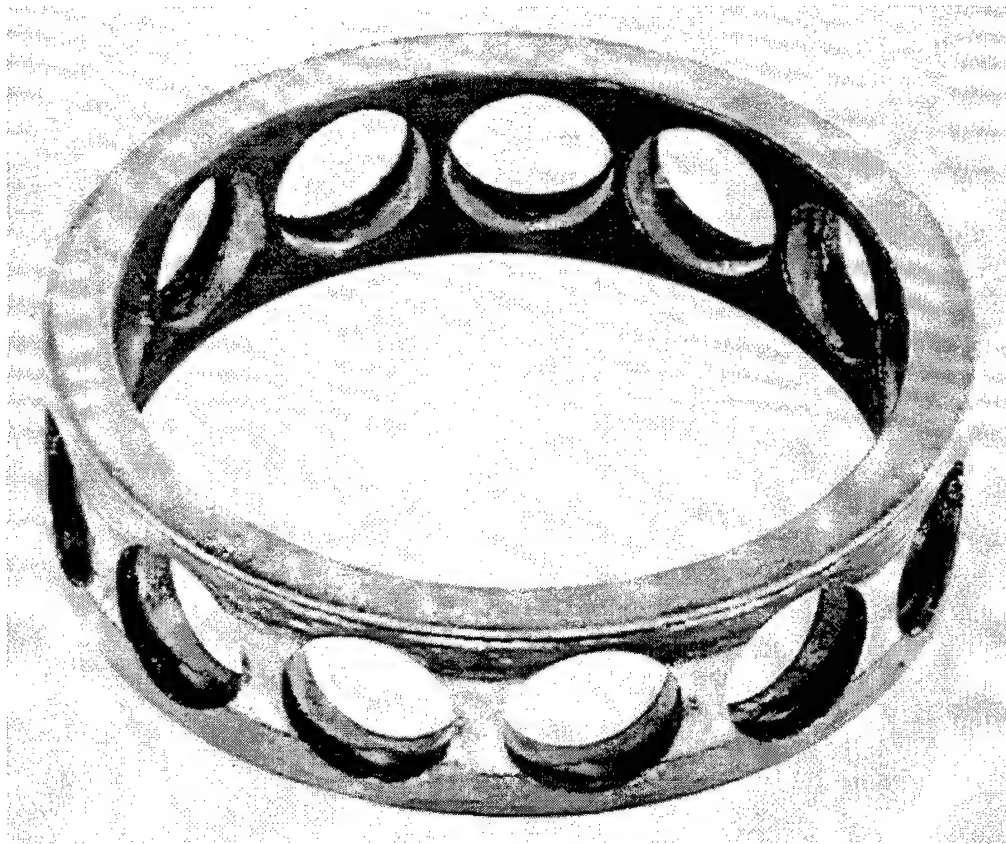


Figure 78. AISI 4340 caged used in the vapor delivery test. The silver is removed from the land surfaces. The silver plating on the noncontacting surfaces is heavily oxidized.

### 6.5 TBPP/TBP Bearing Temperature Tests

Temperature tests with the TBPP/TBP lubricant delivered as an oil-mist are shown in Fig. 79. The TBPP/TBP lubricant was able to lubricate the bearing from room temperature to at least 475°C. At the final test temperature, the band heaters shorted and a circuit breaker disconnected electrical power to the heating system. To obtain some data at the final temperature, the test was started and suspended when the bearing temperature cooled to 375°C. Overall, the lowest mean bearing torque was obtained at bearing temperatures below 150°C and at temperatures above 375°C. Similar results were found with the TBPP/TBP lubricant in Bearing Temperature Tests described in Chapter 3. Also from Fig. 79, the temperature rise to reach steady-state conditions, decreased with increasing environmental temperature. This effect is attributed to convective heat transfer with the oil-mist delivery system. Post-test inspection of the bearing indicates that moderate oxidation of the T15 bearing surface occurred. The oxidation is largely attributed to the final test temperature. Several hours of heating were required to achieve the initial bearing temperature of 475°C.

Additionally, this heating period was performed without applying the lubricant to the bearing. Based on the results in Chapter 4, oxidation of the bearing surface would have been substantially reduced, if the lubricant mist was applied during this initial heating period. A hardness check of the bearing races showed the hardness decreased from an initial value of  $R_c$  63 to  $R_c$  56 after testing, indicating that the T15 steel was susceptible to retempering at  $475^{\circ}\text{C}$ .

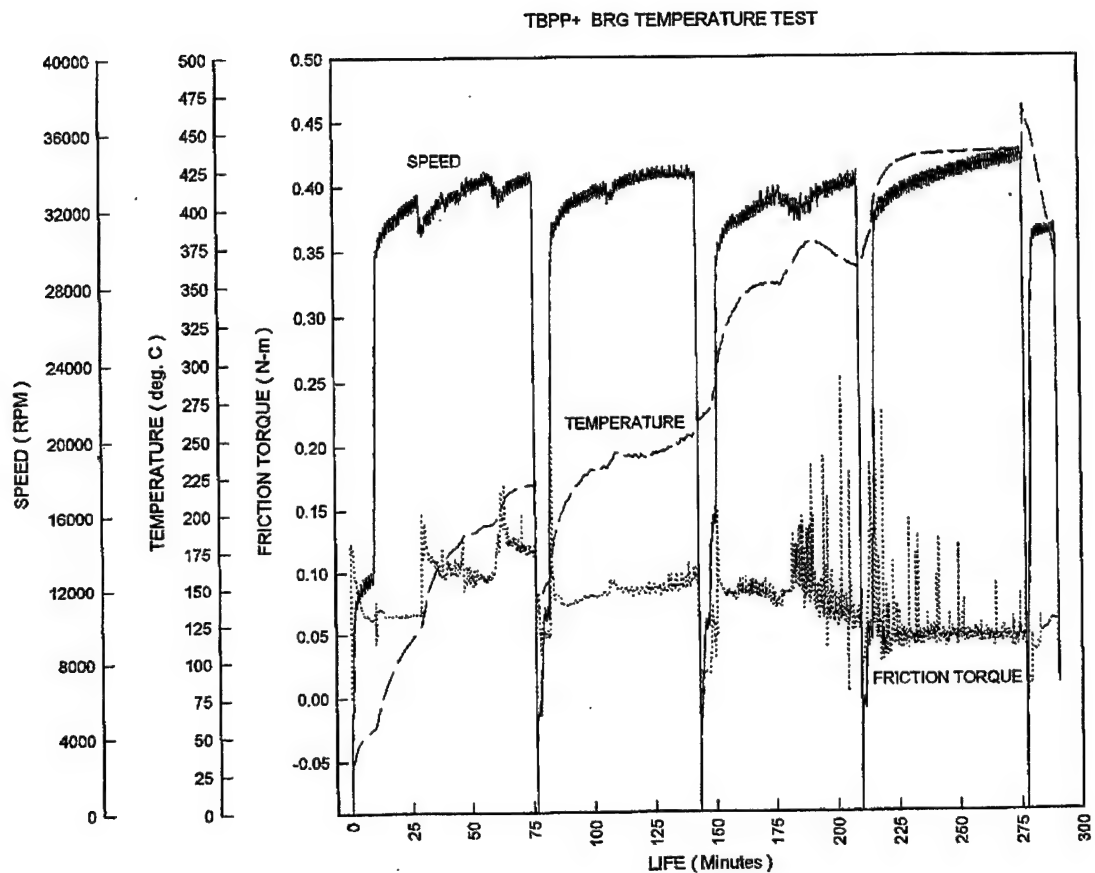


Figure 79. Temperature test results for the TBPP/TBP lubricant delivered as an oil-mist. Test conditions: C-C cage; 445 N applied thrust load; uncoated bearing cages.

## 6.6 TBPP/TBP Load Tests

Results with the TBPP/TBP lubricant, delivered as an oil-mist to a test bearing operating at three different loads, are shown in Fig. 80. At an initial bearing temperature of 375°C with 445 N of applied thrust load, the bearing reached steady-state conditions with a mean torque value of 0.05 N-m and bearing temperature increase of 75°C, essentially the same as found in the TBPP/TBP temperature test under similar conditions. Increasing the thrust load to 900 N, resulted in a steady state mean bearing torque of 0.09 N-m, over a 60-minute period. However, when the bearing thrust load was increased to 1335 N, the bearing torque abruptly increased after 7 minutes of operation. Inspection of the bearing after testing revealed surface damage in the outer race bearing track. The appearance of the damaged area is similar to the micropitting encountered in the ball-on-rod tests, in areas associated with high tensile and shear stress.

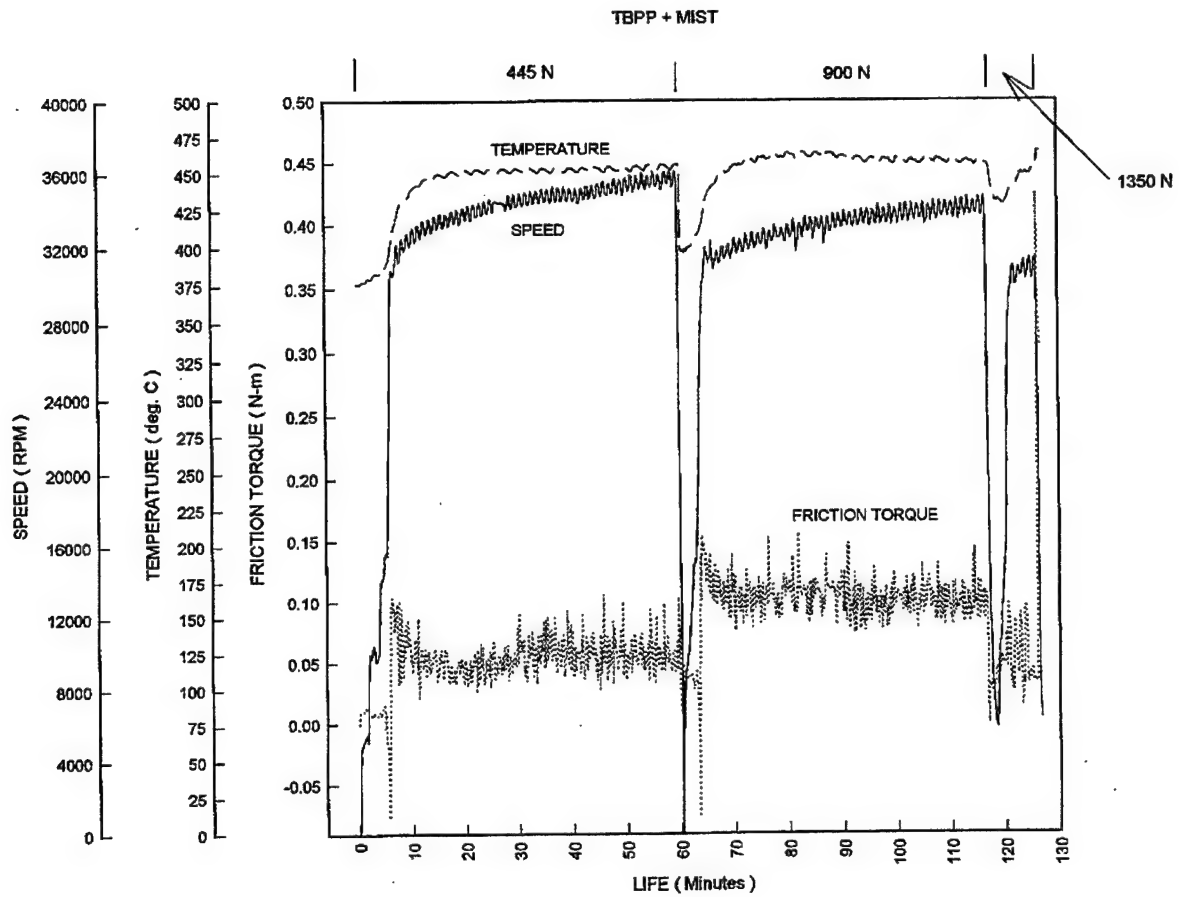


Figure 80. Load test results for the TBPP/TBP lubricant delivered as an oil-mist. Test conditions: C-C cage; 445 N, 900 N, and 1350 N applied thrust loads, uncoated bearing races.



### 6.7 TBPP Load Tests Without TDC

Results for the TBPP load test without the TDC coating are shown in Fig. 81. The bearing reached steady-state conditions, shortly after reaching the desired test speed of 30,000 rpm, with the initial load setting of 445 N. The mean value of the bearing torque was 0.08 N-m, with a bearing temperature rise of 50°C. The shaft speed gradually increased during the test to a speed of 34,000 rpm over a period of 150 minutes. Afterwards, the bearing speed was decreased and the thrust load increased to 1800 N. The bearing maintained a mean bearing torque value of 0.13 N-m, with an overall bearing temperature rise of 90°C at the 1800 N load condition. Approximately 140 minutes of additional test time was accumulated on the bearing at thrust loads of 1800 N , shaft speeds of 36,000 rpm, and bearing operating temperatures of 480°C.

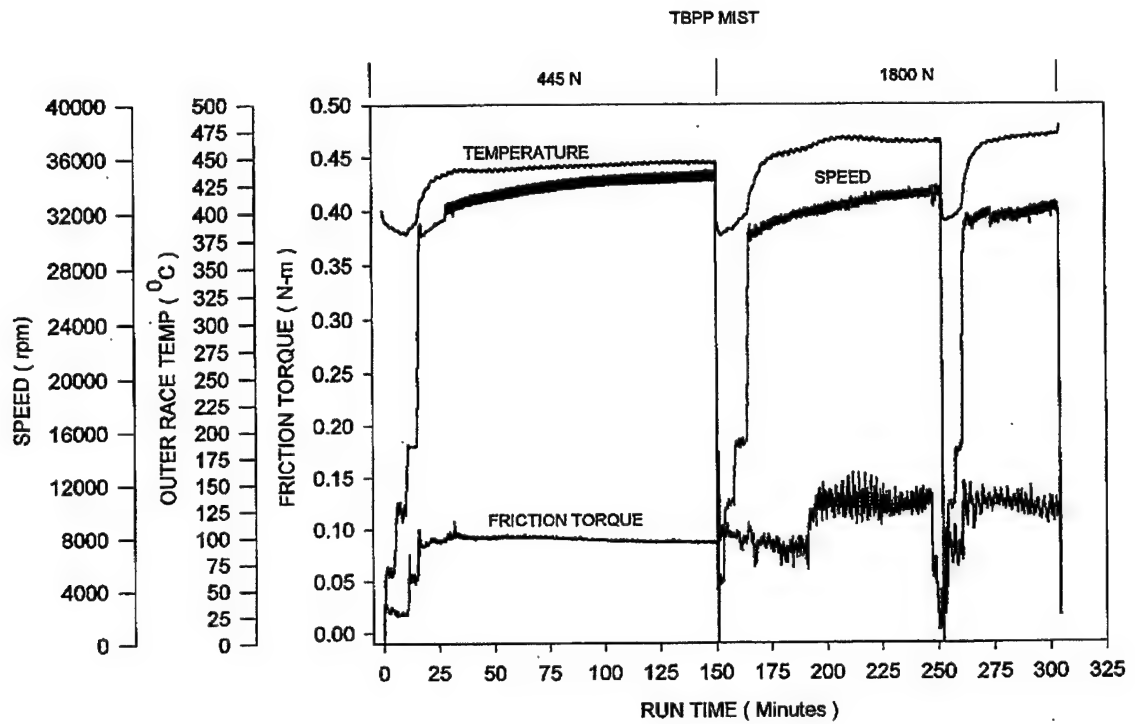


Figure 81. Load test results for the TBPP lubricant delivered as an oil-mist. Test conditions: C-C cage; 445 N and 1800 N applied thrust loads; TDC applied to bearing races.

## 6.8 TBPP Load Tests With TDC

Results with a TDC coated bearing are shown in Fig. 82. The initial temperature of the bearing was 390°C. At the 445 N thrust load, the bearing obtained an initial steady-state bearing torque of 0.11 N-m, 0.02 N-m higher than the uncoated bearing. Over a period of 200 minutes, the bearing torque decreased to a value of 0.09 N-m, the same as the uncoated bearing. The bearing outer race temperature also decreased with time, reaching a final value of 445°C. At 1800 N of applied thrust load, the bearing maintained steady-state conditions, with a bearing torque of 0.12 N-m and 455°C bulk outer race temperature. Under the 1800 N load condition, the TDC coated bearing produced a more stable torque than the uncoated bearing. The TDC coated bearings have a multicolored surface layer after testing, compared to a dull gray appearance obtained with the uncoated bearings. This indicates that the TDC did have a positive impact on reducing oxidation of the bearing steel. However, EDS analysis of the bearing track performed after test, indicates that the TDC coating was not present in the track after test. Based on the torque measurements in Fig. 82, the coating probably wore

away during the 100- to 200-minute period at the 445 N thrust load. The high load test shows a similar decrease in bearing torque, as seen in the 445 N test. This is attributed to additional wear of the TDC coating, due to the shift in contact angle under the higher thrust load condition.

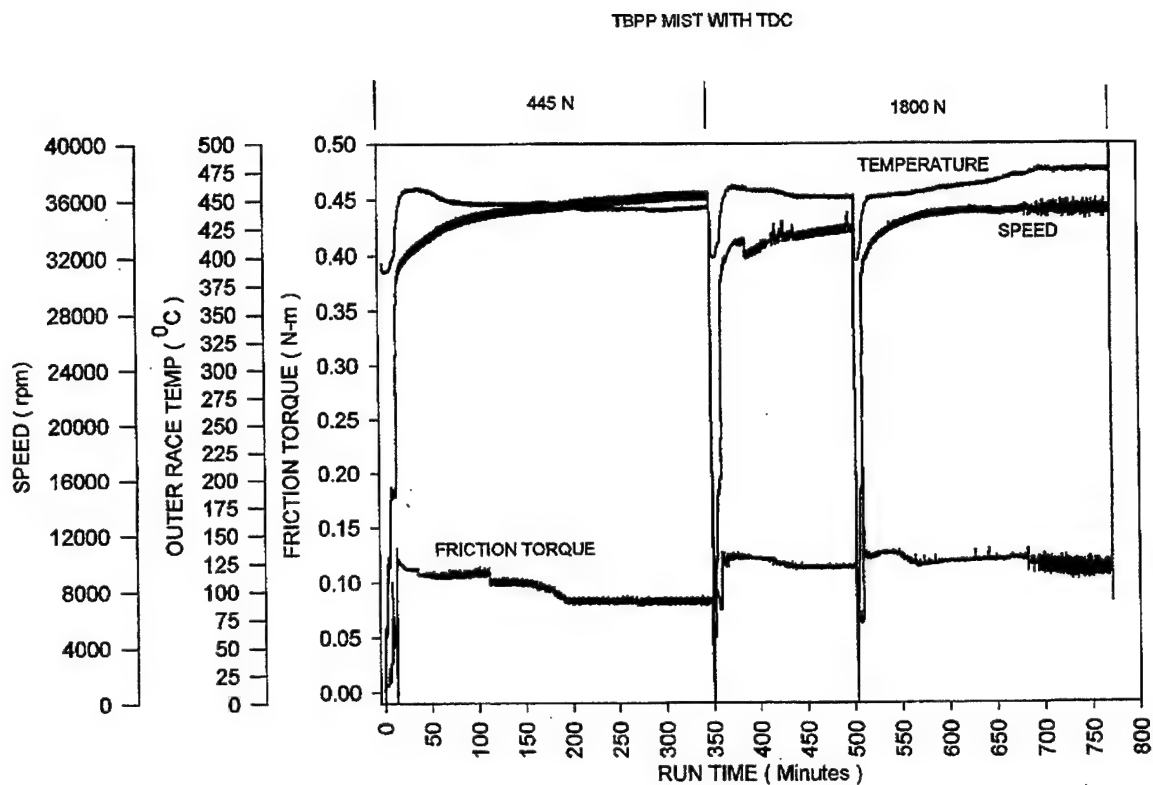


Figure 82. Load test results for the TBPP lubricant delivered as an oil-mist. Test conditions: C-C cage; 445 N and 1800 N applied thrust loads; TDC applied to the bearing races.

## 6.9 X-1P Load Tests

Results for the X-1P cyclophosphazine, delivered as an oil-mist, are shown in Fig. 83. The bearing obtained a steady state operating torque of 0.12 N-m, with a bearing temperature rise of 95°C. The 1800 N applied thrust load test was not attempted, due to the higher bearing torque, compared to the TBPP test results.

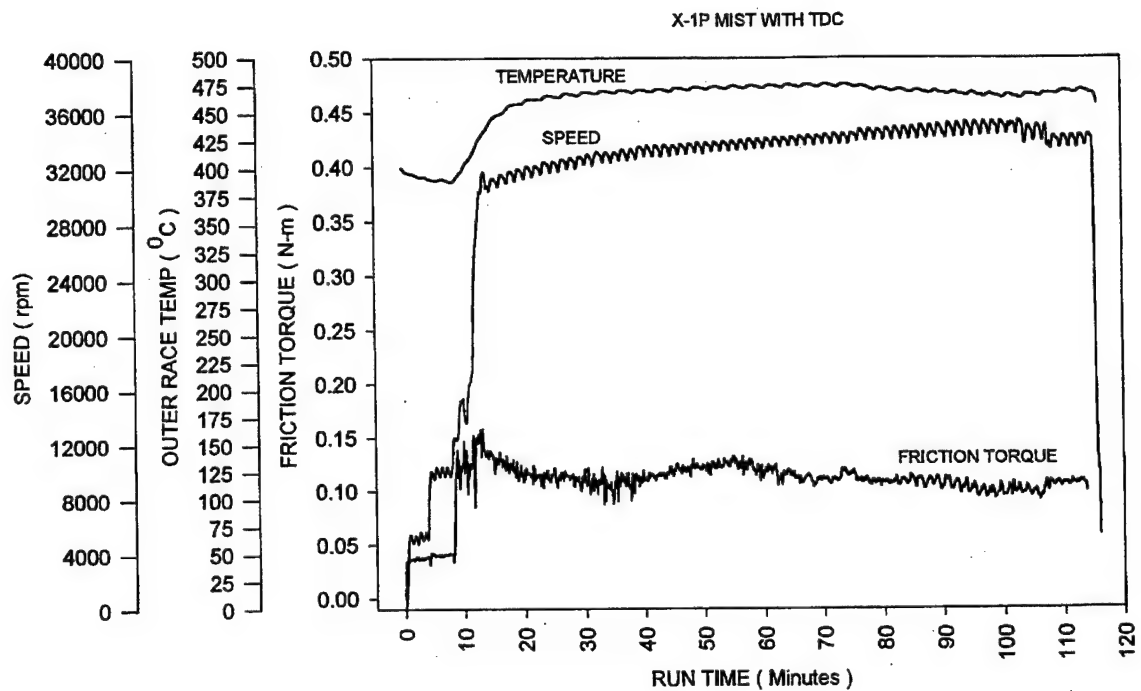


Figure 83. X-1P lubricant delivered as an oil-mist. Test conditions: C-C cage; 445 N applied thrust load; TDC applied to the bearing races.

### 6.10 Bearing Cage Results

Over 32 hours of test time was accumulated on a single C-C bearing cage. Twenty-four hours of the testing are accounted for in Figs. 79-83. Visual inspection of the cage, after each test, showed a highly polished surface at the sliding surfaces. Using profilometry measurements and the total accumulated operating time, the calculated land wear rates for the C-C cage is  $6.651 \times 10^{-10}$  m<sup>3</sup>/hr, compared to a wear rate of  $1.617 \times 10^{-9}$  m<sup>3</sup>/hr for the AISI silver plated cage, used in the vapor lubricated test shown in Fig. 47. The ball pocket wear rate for the C-C cage is  $4.436 \times 10^{-10}$  m<sup>3</sup>/hr compared to a ball pocket wear rate of  $5.726 \times 10^{-10}$  m<sup>3</sup>/hr for the AISI 4340 cage. The C-C cage with the uncoated T15 bearing after the 1800 N thrust load test is shown in Fig. 84.





Figure 84. Uncoated T15 bearing races,  $\text{Si}_3\text{N}_4$  rolling elements, and the C-C composite cage. The races and rolling elements are from the TBPP thrust load test. The C-C cage was used in all of the oil-mist delivery tests.

### 6.11 Test Summary

The bearing test results are summarized in Table 19.  
The total power loss was calculated using Equation 23 (93):

$$\text{EQ 23: } Q = M\omega$$

The total power loss represents the heat input into the bearing due to frictional losses.

Table 19. - Summary of the High Speed Bearing Test Results

	N	L	T	$\Delta T$	M	Q
<u>TBPP Vapor</u>	30,000	445	285	130	0.08	251
<u>TBPP/TBP Mist</u>	33,500	445	25	475	0.12	421
	33,500	445	130	120	0.08	281
Temp. Test	33,000	445	260	110	0.07	173
	30,000	445	475	-	0.05	157
	35,000	445	375	75	0.06	220
Load Test	34,000	900	390	70	0.11	392
	31,300	1335	430	-	0.05	162
<u>TBPP Mist</u>	33,000	445	380	60	0.08	276
	31,000	1800	380	80	0.13	422
TDC	36,000	445	380	60	0.08	302
	35,000	1800	400	60	0.12	440
<u>X-1P</u>	34,000	445	390	80	0.13	462

## 6.12 Discussion

The results indicate that ball bearings can achieve steady-state operation under high speed, high temperature, and high load conditions, using organophosphate and cyclophosphazine lubricants delivered from the vapor phase and as oil-mists. Most of the test temperatures reported are well above the temperature limits expected for even the best synthetic liquid lubricants (i.e., 320°C for polyphenyl and perfluorallylethers). Additionally, the bearing performance obtained at the combined conditions of speed, load, and temperature are substantially better than previous bearing tests, using powder lubricant delivery (1-4), solid lubricant cages (5-8), or vapor phase lubrication via jet fuel with triisopropyl phosphite additives (9). The relative success in the bearing testing is attributed to the properties of the deposited film, discussed in Chapter 4, the addition of oil-mist delivery, and the use of the C-C composite bearing cage.

The oil-mist delivery technique has several advantages over the vapor delivery technique. The increased momentum of the air-borne oil-mist particle, compared to a vapor particle, provides better penetration of the pressure

differential created in high speed bearings. Additionally, oil-mist lubricants can be carried in much cooler air than vapor delivered lubricants. The cooler delivery air provides a significant advantage in convective heat transfer.

The cage-land wear problem with AISI 4340 cages is attributed to the lubrication method, combined with high temperature, and high speed conditions. The decreased momentum of vapor and oil-mist lubrication, compared to liquid lubrication, makes it difficult for the lubricant to enter the narrow gap defined by the cage diametral clearance. Secondly, what little lubricant enters this gap, does not have sufficient hydrodynamic lift to support the cage on a lubricant film, under high sliding conditions. The C-C cage was able to overcome this problem, due to its inherently low coefficient of friction. Additionally, the low wear rates obtained with the C-C composite allowed the cage to maintain critical dimensions and cage balance at 32 hours of operation. Additional benefits are also realized with C-C composite cages, in terms of reducing bearing dynamic forces and improving thermal management of the bearing heat generation.

Of the lubricants tested, the TBPP in the neat condition proved to be the best high temperature lubricant under high thrust load bearing conditions. In the Material Evaluation performed in Chapter 2, TBPP was the only lubricant to survive five 96 hour endurance tests at 3.34 and 3.65 GPa of applied stress with all suspensions. Additionally, this lubricant demonstrated the lowest friction over the widest temperature range, in the Bearing Temperature Test described in Chapter 3. Similar results were found with the TBPP delivered as an oil-mist in the high speed bearing tests.

## CHAPTER VII

### CONCLUSIONS

In Chapter 2, a material evaluation was conducted to examine several classes of high temperature synthetic lubricants as candidate vapor phase lubricants, in combination with several candidate high temperature bearing materials. The results indicate that the choice of lubricant was the most influential design variable in terms of bearing friction, wear, and life. Specific lubricants tested in the material evaluation were: a blend of tertiary-butyl phenyl phosphate molecules (TBPP); a blend of cyclophosphazene molecules (X-1P); a 2 cSt unformulated polyalphaolefin (PAO); and the PAO fluid blended with 15 percent TBPP (PAO/TBPP). At a 370°C bearing temperature, the PAO/TBPP lubricant gave lower friction and wear rates than the other candidate lubricants. However, bearing temperature tests conducted in Chapter 3 showed that this lubricant was limited to bearing temperatures of 480°C, well

below the temperature limits obtained with the TBPP, X-1P, or the TBPP blended with 15 percent tributyl phosphate (TBPP/TBP). The lower operating temperature with the PAO/TBPP lubricant is credited to a lower concentration of phosphate radicals, as well as the lower thermal stability of the PAO molecule. The nonphosphorus lubricants also demonstrated much lower operating temperatures than the organophosphorus lubricants in Chapter 3. These early tests began to show the importance of phosphorus in high temperature vapor phase deposition (VPD) lubrication.

It was also shown in Chapter 2, that highly polished surfaces were found in the bearing tracks of specimens, lubricated with the PAO/TBPP and TBPP lubricants. The surface finish obtained, 0.01  $\mu\text{m}$  translates into one order of magnitude improvement in the ratio of the lubricant film thickness to the surface finish of the bearing. This polishing effect, with the PAO/TBPP and TBPP, makes high temperature bearings much more tolerant of thin film lubrication, as it is easier to minimize metal to metal contact, with a highly polished surface.



It was also noted in Chapter 2 that corrosion pitting was associated with the TBPP lubricant. The corrosion is attributed to electrochemical reactions between phosphate ions and the ferrous alloy substrate. Additionally, the corrosion pitting was most pronounced in regions associated with high tensile and shear stress.

Chapter 3 presents useful information required to successfully design mechanical systems operating with VPD lubrication. The TBPP offers the lowest friction, over the widest temperature range of the lubricants evaluated. The TBPP/TBP provides the best temperature-viscosity characteristics of the VPD lubricants containing phosphorus. However, this lubricant shows a substantial increase in friction, as the bearing lubrication mode transitions from vapor phase condensation (VPC) to VPD. As an alternative approach, a solid lubricant coating was introduced to handle starting conditions for cold weather conditions. This approach proved to be successful in protecting the bearing surface, until the vapor lubrication mode became active. Additional cold-starts on the same bearing track were successfully conducted, using the vapor deposition film left

from a previous test; i.e., the VPD film behaves in a similar manner as the solid lubricant coating. Of the lubricants tested, the X-1P demonstrated the highest bearing temperature capability, with sustained operation at 650°C. It was also shown, that surfaces can be lubricated with the TBPP or X-1P lubricants, with carrier air temperatures of 316°C to 538°C, with only minor changes in bearing friction. This property is particularly important for gas turbine engines, where the lubricant might be carried via bleeding air from the compressor. Depending on flight conditions, the temperature of compressor air can vary considerably. It was also shown, that the delivery rate of lubricant to the bearing surface is a critical variable, in optimizing the bearing performance for the lowest friction and lowest wear rate. The optimum delivery rate also increases with bearing temperature. A reasonable explanation is provided by the diffusion mechanisms explored in Chapter 5. At lower than the optimum concentration, there is insufficient lubricant to generate the VPD film. The lubricant film thickness is lower and the bearing substrate becomes more prone to oxidation. If the delivery rate is too high, there is an

over consumption of iron cations, with higher levels of iron at the vapor interface. In essence, chemical reaction rates with lubricants containing phosphorus have a significant effect on the bearing wear rate.

In Chapter 4, specimens from Chapters 2 and 3 were investigated, using various analytical surface techniques. The results indicate the TBPP and X-1P lubricants generate deposition films, containing phosphate with substantial amounts of graphite of short range order. The predominant P-O-P band, detected by Fourier transform infrared microscopy, indicates crosslinking of phosphate ions occurs in the formation of the VPD film. Analysis of  $\text{Si}_3\text{N}_4$  rolling elements from the TBPP and X-1P specimens did not show the presence of phosphates or substantial amounts of graphite on the surface, indicating that chemical reactions are involved in the deposition of vapor lubricant films on ferrous materials with the lubricants containing phosphorus. VPD films, generated with the 5P4E lubricant, indicate that small amounts of graphite and iron oxides are present in the deposition film. One explanation, for the relatively poor performance of the 5P4E as a VPD lubricant, is the presence

of iron oxides found on the bearing surface. Iron oxides, and particularly  $\text{Fe}_2\text{O}_3$ , are known to be abrasive in tribo-contacts (71). Therefore, a specific advantage of the lubricants containing phosphorus is their ability to serve as antioxidants for the bearing substrate and for the graphite in the VPD lubricating film. Phosphates are known to possess this property in other applications (69,70). Although low levels of oxygen were normally found in the VPD deposition film generated with the TBPP lubricant, very high levels of oxygen were detected in regions associated with corrosion pitting. Cross sections of corrosion pits indicate that the damage transcends to depths of at least 10  $\mu\text{m}$  into the bearing substrate. Of the components detected on the surface, graphite is the only known component to have lubricating properties.

Auger electron spectroscopy (AES) depth profiles, analyzed in Chapter 5, indicate the semi-infinite solution for diffusion can be used to further investigate VPD films, generated with the TBPP lubricant. Using Darken's analysis, and setting the velocity of the Matano interface equal to the bearing wear rate, diffusion coefficients of the order

of  $1 \text{ nm}^2/\text{s}$  are obtained for iron, at bearing temperatures of  $370^\circ\text{C}$  and  $430^\circ\text{C}$ . This is six orders of magnitude larger than the self-diffusion coefficient of body centered cubic (BCC) iron at  $370^\circ\text{C}$  and four order higher than the value at  $430^\circ\text{C}$ . This result indicates that substantial forces are present in the preferential flux of iron atoms and/or cations towards the surface of the bearing, and that these forces are not predominately temperature driven. By comparing specimens immediately quenched in liquid  $\text{N}_2$ , with specimens quenched after additional exposure to the TBPP vapor under static conditions, it is apparent that dynamic conditions contribute significantly to the diffusion rate. The most prominent dynamic conditions are the substantial stress gradients, which exist in the subsurface of the bearing contact. Also, very little difference was found in the AES profiles for surfaces generated for different bearing run times. This result indicates that the Matano interface, travels at a fixed distance from the bearing surface under dynamic conditions, and lends further support to the use of Darken's analysis in the analytical approach.

In AES depth profiles of the 5P4E deposition film, oxygen is the primary element diffusing to fill the voids created by the flux of iron from the bearing substrate; whereas carbon is the primary element traveling to fill the iron voids in the TBPP deposition film. In both cases, cation diffusion is thought to also play an important role in the diffusion mechanism. In the case of 5P4E VPD films, oxygen anions attract the iron cations, which accounts for the iron oxides detected on the bearing surface. For the TBPP VPD films, phosphorus anions are thought to attract iron cations. The P-O-P structure, being highly cross-linked, indicates that a substantial portion of the phosphorus is not free to diffuse in the bearing substrate. Carbon fulfills the role of balancing voids, to create a stable film in VPD films generated with the phosphorus containing lubricants. The diffusion mechanism certainly adds to the tenacity of the lubricating film on bearing surfaces.

The full-scale bearing tests in Chapter 6 indicate that steady-state operation of bearings can be achieved at bearing speeds above 1 MDN ( $\text{MDN} = 10^{-6} \times \text{shaft diameter in}$

mm x shaft speed in rpm), and bearing temperatures of at least 475°C. This is the first time that bearings have achieved stable operation in the temperature range of 350°C to 475°C, at these bearing speed conditions. The addition of carbon-carbon composite bearing cages and oil-mist delivery of the TBPP lubricant substantially contributed to this accomplishment. Both additions assist in managing the heat generation in high speed bearings.

## CHAPTER 8

### FUTURE WORK

Additional work required to characterize VPD lubrication in rolling element bearings includes; traction measurements, film thickness measurements using optical interferometry, bearing analyses using a bearing dynamics computer code, thermal modeling using finite element analysis, and demonstration in a gas turbine engine. All of this work is in progress, and will be reported in future papers.



## 9. REFERENCES

1. Macks, E.F., Nemeth, Z.N., Anderson, W.J., "Preliminary Investigation of Molybdenum Disulfide - Air-Mist Lubrication of Roller Bearings Operating to DN Values of  $1 \times 10^6$  and Ball Bearings Operating to Temperatures of  $1000^\circ\text{F}$ ," NACA RM ES1 631 (1951).
2. Anderson, W.J., "Advanced Bearing Technology," NASA SP-38 (1965), Eds. Bisson, E.E., Anderson W.J., pp 309-370.
3. Wilson, D.S., "Powdered and Gaseous Lubricants for Use in Ball Bearings at Temperatures from Room Temperature to  $1200^\circ\text{F}$ ," ASD-TDR-62-465 (1962), Eds. Beane, G.A., Berkey, K.L., pp 201-209.
4. Wallerstein, S., "Application of a Gas Powder Lubrication System to a Gas Turbine Engine," AFAPL-TR-65-43 (1965).
5. Devine, M.J., Lamson, E.R., Bowen, J.H., "The Lubrication of Ball Bearings with Solid Films," ASME 61-UBS-11, (1961).
6. Dayton, R.D., "Experimental Investigation of Ag-Hg-WTFe-MoSe<sub>2</sub> Solid Lubricated Ball Bearings for High Speed, High Temperature, and High Load Applications," AFAPL-TR-71-100 (1971).
7. Boes, D., "Development of Light Weight Solid Lubricated Bearing Retainers," Air Force AFAPL-TR-78-72 (1978).
8. Gardos, M.N., "Solid Lubricated Rolling Element Bearings Final Report," AFWAL-TR-83-4129 (1984).
9. Coit, R.A., Sorem, S.S., Armstrong, R.L., Converse, C.A., "Research in High Temperature Bearing Lubrication in the Absence of Liquid Lubricants," WADC TR-370 Part III (1957).

10. Graham, E.E., and Klaus, E.E., "Lubrication from the Vapor Phase at High Temperatures," ASLE Trans., **29**, pp 229-234 (1985).
11. Gunsell, S., "Development and Evaluation of a High-Temperature Lubrication System," PhD Dissertation, Pennsylvania State University (1986).
12. Klaus, E.E., Jeng, G.S., Duda, J.L., "A Study of Tricresyl Phosphate as a Vapor Delivered Lubricant," Lubr. Eng., **45**, pp 717-723 (1989).
13. Maki, J.F., Graham, E.E., "Vapor Phase Deposition on High Temperature Surfaces," Trib. Trans., **33**, 4, pp 595-603 (1990).
14. Maki, J.F. Graham, E.E., "Formation of Solid Films from the Vapor Phase on High Temperature Surfaces," Lubr. Eng., **47**, pp 199-206 (1991).
15. Groenewig, M., Hakim, N., Barber, G.C., Klaus, E.E., "Vapor Delivered Lubrication for Diesel Engines - Cylinder Kit Rig Simulation," Lubr. Eng., **47**, pp 1035-1039 (1991).
16. Graham, E.E., Nesarikar, A., Forster, N.H., Givan, G.D., "Vapor Phase Lubrication of High Temperature Bearings," Lubr. Eng., **49**, 9, pp 713-718 (1993).
17. Rao, A.M.N., "Identification of an Alternative Lubricant for Vapour Phase Lubrication," M.S. Thesis, Cleveland State University, (1993).
18. Hanayaloglu, B., Fedor, D.C., Graham, E.E., "Vapor Phase Lubrication of a Ni Base Superalloy," Lubr. Eng., **51**, 3 (1994).
19. Hanyaloglu, B., and Graham, E.E., "Vapor Phase Lubrication of Ceramics," Lubr. Eng., **50**, 10, pp 814-820 (1994).
20. Klaus, and E.E. Duda, J.L., "Vapor Phase Lubrication Development for Engines," SAE Publ. SP-256, pp 541-550 (1991).

21. Wedeven, L.D., "Development of Variable (VP) Lubrication with Condensed Vapors," presented at the 1993 STLE Annual Conference.
22. Lauer, J.L. and Bunting, B.G., "Catalytic Generation of Lubricants from Carbonaceous Gases on Surfaces Undergoing Friction at High temperatures," SAE Publ. SP-738, pp 51-60 (1988).
23. Lauer, J.L. and Dwyer, S.R., "Tribochemical Lubrication of Ceramics by Carbonaceous Vapors," Trib. Trans., **34**, 4, pp 521-528 (1991).
24. Marino, M.P., and Placek, D.G., "Phosphate Esters," CRC Handbook of Lubrication and Tribology Vol III, CRC Press, Inc., Ed. Booser, R.R., pp 269-286 (1994).
25. Nader, B.S., Kar, K.K., Morgan, T.A., Pawloski, C.E., Dilling, W.L., "Development and Tribological Properties of New Cyclotriphosphazene High Temperature Gas Turbine Engines," Trib. Trans., **35**, 1, pp 37-44 (1992).
26. Johnson, M.K., "Organophosphates and Delayed Neuropathy - Is NTE Alive and Well?" Toxic. and Appl. Pharm., **102**, pp 385-399 (1990).
27. Johannsen, F.R., Wright, P.L., Gordon, D.E., Levinkas, G.J., Radue, R.W., Graham, P.R., "Evaluation of Delayed Neurotoxicity and Dose-Response Relationships of Phosphate Esters in the Adult Hen," Toxic. and Appl. Pharm., **41**, pp 291-304 (1977).
28. Wright, R.L., "The Gas Phase Decomposition and Trimethylolpropane Phosphate Neurotoxin Formation Potential of Tricresyl and t-Butylphenyl Phosphates," PhD Dissertation, University of Dayton (1995).
29. Centers, P.W., "Potential Neurotoxin Formation in Thermally Degraded Synthetic Ester Turbine Lubricants," Arch. Toxicol., pp 679-680 (1992).
30. Kotkoskie, L.A., Freeman, C. Loeb, W., McConnell, R.F., Weiner, M.L., "Evaluation of the Acute Delayed Neurotoxicity

of Durad 200B<sup>R</sup> Triaryl Phosphate in the Domestic Hen," The Toxicologists, **12**, p 280 (1992).

31. Latenderse, J.R., Brooks, C.L., Capen, C.C., "Pathological Effects of Butylated Triphenyl Phosphate - Based Hydraulic Fluid and Tricresyl Phosphate on the Adrenal Gland, Ovary, and Testis in the Fischer - 344 Rat," Toxic. Pathology, **22**, 4, pp 341-352 (1994).

32. Latendresse, J.R., Azhar, S., Brooks, C.L., Capen, C.C., "Pathogenesis of Cholesteryl Lipidosis of Adrenocortical and Ovarian Interstitial Cells in F344 Rats Caused by Tricresyl Phosphate and Butylated Triphenyl Phosphate," Toxic. and Appl. Pharm., **122**, pp 281-289 (1993).

33. Singler, R.E., and Bieberich, M.J., "Synthetic Lubricants and High Performance Functional Fluids - Phosphazenes," Army ARL-TR-45 (1993).

34. Choa, S.H., Ludema, K.C., Potter, G.E., DeKoven, B.M., Morgan, T.A., Kar, K.K., "A Model for the Boundary Film Formation and Tribological Behavior of Phosphazene Lubricant on Steel," Trib. Trans., **38**, 4, pp 757-768 (1995).

35. Shankwalker, S.G. Placek, D.G., "Oxidation and Weight Loss Characteristics of Commercial Phosphate Esters," Ind. Eng. Chem. Res., **31**, 7, pp 1810-1813 (1992).

36. Godfrey, D.G., "The Lubrication Mechanism of Tricresyl Phosphate on Steel," ASLE Trans., **8**, pp 1-11 (1965).

37. Beiber, H.E., Klaus, E.E., Tewksbury, E.J., "A Study of Tricresyl Phosphate as an Additive for Boundary Lubrication," ASLE Trans., **11**, pp 155-161 (1968).

38. Morales, W., Hanyaloglu, B., Graham, E.E., "Infrared Analysis of Vapor Phase Deposited Tricresyl Phosphate (TCP)," NASA TM-106423 (1994).

39. Glover, D., "A Ball-Rod Rolling Contact Fatigue Tester," ASTM SP-771, pp 107-124 (1982).

40. Trivedi, H.K., Gerardi, D.T., Forster, N.H., Rosado, L., Givan, G.D., "A Modified Ball-on-Rod Contact Fatigue (RCF)

Tester for Accelerated Testing of Candidate Lubricants and Bearing Materials," SAE Publ. SP-1069, pp 83-90 (1995).

41. Box, G.E.P., Hunter, W.G., Hunter, S.J., Statistics for Experimenters, John Wiley & Sons, New York (1978), pp 374-412.

42. Neter, J., Wasserman, W., Kutner, M.H., Applied Linear Statistical Models, Irwin, Inc., Boston, pp 818-836 (1990).

43. Neter, J. Wasserman, W., Kutner, M.H., Applied Linear Statistical Models, Irwin, Inc., Boston, pp 580-585 (1990).

44. Box, G.E.P., Hunter, W.G., Hunter, S.J., Statistics for Experimenters, John Wiley & Sons, New York, pp 232-234 (1978).

45. Timoshenko, S. and Goodier, J.N., Theory of Elasticity, McGraw-Hill Book Co., Inc., New York, pp 376-381 (1951).

46. Beeck, O., J. Applied Phys., **12**, 512 (1941).

47. Hatton, R.E., "Phosphate Esters," Chapter 4, Synthetic Lubricants, Reinhold Publ. Co., London, Eds. Gunderson, R.C., Hart, A.W., pp 119-121 (1962).

48. Klaus, E.E. and Fenske, M.R., Preprints Petroleum Division of ACS, **1**, **3**, p 58 (1956).

49. Mahoney, C.L. and Barnum, E.R., "Polypheyl Ethers," Chapter 11, Synthetic Lubricants, Reinhold Publ. Co., London, Eds. Gunderson, R.C., Hart, A.W., pp 423-438 (1962).

50. Hatton, R.E., "Phosphate Esters," Chapter 4, Synthetic Lubricants, Reinhold Publ. Co., London, Eds. Gunderson, R.C., Hart, A.W., pp 132-133 (1962).

51. Jones, W.R., "Properties of Perfluoropolyethers for Space Applications," Trib. Trans., **38**, **3**, pp 557-564 (Date).

52. "Standard Test Method for Kinematic Viscosity of Transparent and Opaque Liquids (and the Calculation of Dynamic Viscosity)," **05.01**, ASTM, Philadelphia, PA, pp 170-175 (1990).

53. "Viscosity-Temperature Charts for Liquid Petroleum Products," 05.01, ASTM, Philadelphia, PA, pp 140-144 (1990).
54. Klaus, E.E., Phillips, J., Lin, S.C., Wu, N.L., Duda, J.L., "Structure of Films Formed During the Deposition of Lubrication Molecules on Iron and Silicon Carbide," Trib. Trans., 33, 1, pp 25-32 (1990).
55. Colthup, N.B., Daly, L.H., Wiberly, S.E., Introduction to Infrared and Raman Spectroscopy, Academic Press, Inc., Boston, pp 217-218 (1990).
56. Corbridge D.E.C. and Lowe, E.J., "The Infra-red Spectra of Some Inorganic Phosphorus Compounds," The Structural Chemistry of Phosphorus, Elsevier Scientific Publ. Co., New York, pp 493-502 (1974).
57. Colthup, N.B., Daly, L.H., Wiberly, S.E., Introduction to Infrared and Raman Spectroscopy, Academic Press, Inc., Boston, p. 363 (1990).
58. Colthup, N.B., Daly, L.H., Wiberly, S.E., Introduction to Infrared and Raman Spectroscopy, Academic Press, Inc. Boston, pp 289-325 (1990).
59. Sommer, A.J., Miami University, OH, private communication.
60. Colthup, N.B., Daly, L.H., Wiberly, S.E., Introduction to Infrared and Raman Spectroscopy, Academic Press, Inc. Boston, pp 11-15 (1990).
61. Colthup, N.B., Daly, L.H., Wiberly, S.E., Introduction to Infrared and Raman Spectroscopy, Academic Press, Inc., Boston, p.366 (1990).
62. Nakamizo, M., Kammereck, R., Walker, P.L., "Laser Raman Studies of Carbons," Carbon, 12, pp 259-267 (1974).
63. Nakamizo, M., Tamai, K., "Raman Spectra of the Oxidized and Polished Surfaces of Carbon," Carbon, 22, pp 197-198 (1984).

64. Hamilton, J.C., Mills, B.E., Benner, R.E., "Depth Profiling of Metal Oxides Using Raman Spectroscopy with Ion Bombardment," Appl. Phys. Lett., **40**, pp 499-501 (1982).
65. Shewmon, P.G., Diffusion in Solids, The Minerals, Metals & Materials Society, 2nd Ed., pp 19-24 (1989).
66. Borg, R.J. and Dienes, G.J., An Introduction to Solid State Diffusion, Academic Press, Inc., San Diego, CA, pp 15-18 (1988).
67. Corbridge, D.E.C., Phosphorus - An Outline of It's Chemistry, Biochemistry and Technology, Elseveir, Amsterdam (1990), pp 210-211.
68. Klaus, E.E., Phillips, J., Lin, S.C., Wu, N.L., Duda, J.L., "Structure of Films Formed During the Decomposition of Lubrication Molecules on Iron and Silicon Carbide," Trib. Trans., **33**, pp 25-32 (1990).
69. McKee, D.W., Spiro, C.L., Lamby, E.J., "The Inhibition of Graphitic Oxidation by Phosphorus Additives," Carbon, **22**, pp 285-290 (1984).
70. Corbridge, D.E.C., Phosphorus An Outline of It's Chemistry, Biochemistry and Technology, Elseveir, Amsterdam (1990) p 269.
71. Bailey, C.H. and Sorem, S.S., "Research in High Temperature Bearing Lubrication in the Absence of Liquid Lubricants," WADC TR-370, Part I (1956).
72. Evans, U.R., An Introduction to Metallic Corrosion, Edward Arnold Ltd, London (1963) p 16.
73. Rausch, W.R., The Phosphating of Metals, ASM International, Metals Park, OH, pp 194-198 (1990).
74. Shewmon, P.G., Diffusion in Solids, The Minerals, Metals & Materials Society, 2nd Ed., pp 12-15 (1989).

75. Borg, R.J. and Dienes, G.J., An Introduction to Solid State Diffusion, Academic Press, Inc., San Diego, CA, p 3 (1988).
76. Shewmon, P.G., Diffusion in Solids, The Minerals, Metals & Materials Society, 2nd Ed., p 47 (1989).
77. Borg, R.J. and Dienes, G.J., An Introduction to Solid State Diffusion, Academic Press, Inc., San Diego, CA, pp 173-184 (1988).
78. Shewmon, P.G., Diffusion in Solids, The Minerals, Metals & Materials Society, 2nd Ed., pp 131-148 (1989).
79. Shewmon, P.G., Diffusion in Solids, The Minerals, Metals & Materials Society, 2nd Ed., pp 34-37 (1989).
80. Shewmon, P.G., Diffusion in Solids, The Minerals, Metals & Materials Society, 2nd Ed., pp 30-32 (1989).
81. Lipscomb, J.C., "Vapor Phase Lubricant Toxicity," Armstrong medical Research laboratory, Presentation (1996).
82. Press, W.H., Teukolsky, S.A., Vetterling, W.T., Flannery, B.P., Numerical Recipes, Cambridge University Press, University of Cambridge, 2nd Ed., pp 675-683 (1992).
83. Borg, R.J. and Dienes, G.J., An Introduction to Solid State Diffusion, Academic Press, Inc., San Diego, CA, p 60 (1988).
84. Shewmon, P.G., Diffusion in Solids, The Minerals, Metals & Materials Society, 2nd Ed., p 89 (1989).
85. Krishtal, M.A., Diffusion Processes in Iron Alloys, U.S. Department of Commerce, Springfield, VA, pp 139-142 (1970).
86. Borg, R.J. and Dienes, G.J., An Introduction to Solid State Diffusion, Academic Press, Inc., San Diego, CA, pp 111-116 (1988).
87. Tung, S.C., Smolenski, D.J., Wanng, S.S., "Determination of Differences in Tribological Behavior and Surface



Morphology Between Electrodeposited and Traditional Phosphate Coatings," Thin Solid Films, **200**, pp 247-261 (1991).

88. Evans, U.R., An Introduction to Metallic Corrosion, Edward Arnold Ltd, London, p 39 (1963).

89. Savage, G., Carbon-Carbon Composites, Chapman and Hall, London (1993), p 375.

90. Rand, B., "Matrix Precursors for Carbon-Carbon Composites," Chapter 3, Essentials of Carbon-Carbon Composites, Royal Society of Chemistry, Cambridge (1993), Ed. Thomas, C.R., p 77.

91. Savage, G, Carbon-Carbon Composites, Chapman and Hill, London (1993), p 375.

92. McEnaney, B, and Mays, T., "Relationships Between Microstructure and Mechanical Properties in Carbon-Carbon Composites," Chapter 6, Essentials of Carbon-Carbon Composites, Royal Society Chemistry, Cambridge (1993), Ed. Thomas, C.R., pp 170-171.

93. Harris, T.A., Rolling Bearing Analysis, John Wiley and Sons Inc., New York, NY (1966), p 454.

Appendix A  
Hertzian Stress Calculations

# Hertzian Stress Solution for the Ball on Rod Tester

$$\nu := 0.29$$

$\nu$  = Poisson's ratio

$$E := 29 \cdot 10^6$$

$E$  = Modulus of Elasticity (lbs/in<sup>2</sup>)

$$R_{1x} := \frac{.375}{2}$$

$R_{1x}$  = Radius of the rod in the rolling direction (in)

$$R_{1y} := 99999$$

$R_{1y}$  = Radius of the rod transverse to rolling (in)

$$R_{2x} := .250$$

$R_{2x}$  = Radius of the ball in the rolling direction (in)

$$R_{2y} := .250$$

$R_{2y}$  = Radius of the ball transverse to rolling (in)

$$L := 56.33$$

$L$  = Load between the ball and rod (lbs)

$$A := \frac{1}{2} \cdot \left( \frac{1}{R_{1x}} + \frac{1}{R_{1y}} + \frac{1}{R_{2x}} + \frac{1}{R_{2y}} \right)$$

$$B := \frac{1}{2} \cdot \left[ \left( \frac{1}{R_{1x}} - \frac{1}{R_{1y}} \right)^2 + \left( \frac{1}{R_{2x}} - \frac{1}{R_{2y}} \right)^2 + 2 \cdot \left( \frac{1}{R_{1x}} - \frac{1}{R_{1y}} \right) \cdot \left( \frac{1}{R_{2x}} - \frac{1}{R_{2y}} \right) \right]^{0.5}$$

$$k_1 := \frac{1 - \nu^2}{\pi \cdot E}$$

$$k_2 := \frac{1 - \nu^2}{\pi \cdot E}$$

$$\theta := \arccos\left(\frac{B}{A}\right) \cdot \frac{180}{\pi}$$

$$\theta = 66.42188716$$

$$m := \frac{(1.284 - 1.378) \cdot (\theta - 65)}{(70 - 65)} + 1.378$$

$$m = 1.35126852$$

$$n := \frac{(.802 - .759) \cdot (\theta - 65)}{(70 - 65)} + .759$$

$$n = 0.77122823$$

$$a = \text{Semi-Major Axis} \quad a := m \cdot \left[ \frac{3 \cdot \pi \cdot L \cdot (k_1 + k_2)}{4 \cdot A} \right]^{\frac{1}{3}} \quad a = 0.00995862$$

$$b = \text{Semi-Minor Axis} \quad b := n \cdot \left[ \frac{3 \cdot \pi \cdot L \cdot (k_1 + k_2)}{4 \cdot A} \right]^{\frac{1}{3}} \quad b = 0.00568382$$

$$P = \text{Maximum Hertzian Stress} \quad P := \frac{3 \cdot L}{2 \cdot \pi \cdot a \cdot b} \quad P = 4.75162206 \cdot 10^5$$

$$\beta := \frac{b}{a} \quad e := \frac{\sqrt{a^2 - b^2}}{a}$$

Shear stress at the end of the major axes =  $\tau$

$$\tau := (1 - 2 \cdot \nu) \cdot P \cdot \frac{\beta}{e^2} \cdot \left( 1 - \frac{\beta}{e} \cdot \operatorname{atan} \left( \frac{e}{\beta} \right) \right) \quad \tau = 5.58111334 \cdot 10^4$$

Kinematic Relations

$$N = \text{rod rpm} \quad N := 3600$$

$$\omega = \text{rod angular vel (rad/s)} \quad \omega := \frac{N \cdot 2 \cdot \pi}{60} \quad \omega = 376.99111843$$

$$v = \text{surface velocity (in/s)} \quad v := \omega \cdot R_{1x} \quad v = 70.68583471$$

$$\Psi = \text{stress cycles/rev of the rod} \quad \Psi := 2.63$$

$$\text{Time between stress cycles, } t_1 \quad t_1 := \frac{\Psi}{\omega} \quad t_1 = 0.00697629$$

$$\text{Time spent in the stress contact} = t_2 \quad t_2 := \frac{b}{v} \quad t_2 = 8.04095926 \cdot 10^{-5}$$

Appendix B

Nolinear Regression Calculations

Sigma Plot files used to fit and plot AES profile data to diffusion eq.

Carbon Diffusion fit calculations:

```
[Parameters]
b=29
[Variables]
a=col(8)
y=col(4)
[Equations]
terf(x)=1/(1+.47047*x)
erf(x)=1-(.3480242*terf(x)-.0958798*terf(x)^2+.7478556*terf(x)^3)*exp(-x^2)
erf1(x)=if(x<0,-erf(-x),erf(x))
f=26.5*(1-erf1((a-27.5)/b))+10.5
fit f to y
```

Carbon diffuion calculations:

```
d=col(8)
terf(x)=1/(1+.47047*x)
erf(x)=1-(.3480242*terf(x)-.0958798*terf(x)^2+.7478556*terf(x)^3)*exp(-x^2)
erf1(x)=if(x<0,-erf(-x),erf(x))
f=26.5*(1-erf1((d-27.5)/20.15))+10.5
put f into col(9)
```

Iron fit calculations:

```
[Parameters]
b=25
[Variables]
a=col(8)
y=col(7)
[Equations]
terf(x)=1/(1+.47047*x)
erf(x)=1-(.3480242*terf(x)-.0958798*terf(x)^2+.7478556*terf(x)^3)*exp(-x^2)
erf1(x)=if(x<0,-erf(-x),erf(x))
f=33.5*(1+erf1((a-32)/b))
fit f to y
```

Iron diffusion calculations:

```
d=col(8)
terf(x)=1/(1+.47047*x)
erf(x)=1-(.3480242*terf(x)-.0958798*terf(x)^2+.7478556*terf(x)^3)*exp(-x^2)
erf1(x)=if(x<0,-erf(-x),erf(x))
f=33.5*(1+erf1((d-32)/20.71))
put f into col(10)
```

Appendix C

Diffusion Calculations

# Concentration profile analysis from experimental AES data

$x := 0..100$

$x = \text{distance in (nm)}$

Fe input data      C input data

$Dt_{\text{Fe}} := 106.8$

$Dt_{\text{C}} := 101.4$

$Dt = \text{Diffusion Coeff.} \cdot \text{time from exp. data (nm}^2\text{)}$

$Cs_{\text{Fe}} := 0.67$

$Cs_{\text{C}} := 0.63$

$Cs = \text{Concentration of Fe at } x = +\infty \text{ \& C at } x = -\infty \text{ (At\%)}$

$Co_{\text{Fe}} := 0$

$Co_{\text{C}} := 0.105$

$Co = \text{Concentration of Fe at } x = +\infty \text{ \& C at } x = -\infty \text{ (At\%)}$

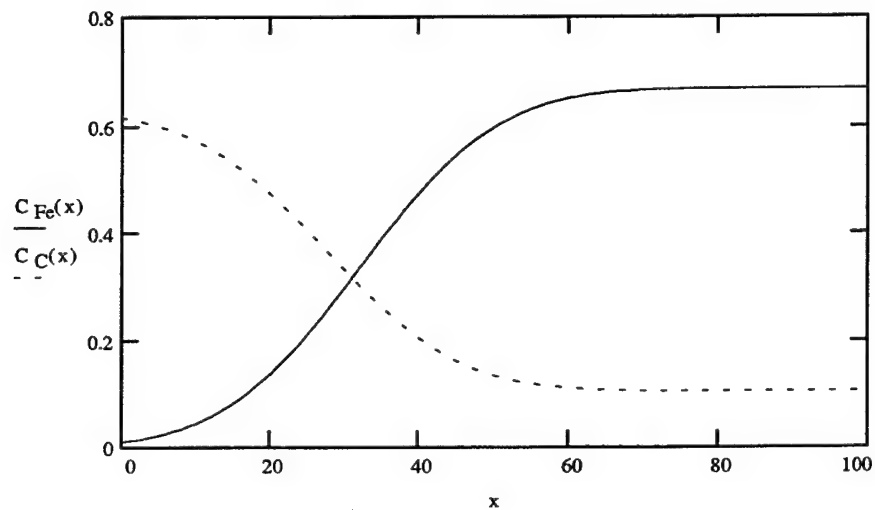
$d_{\text{Fe}} := 32.0$

$d_{\text{C}} := 27.5$

$d = \text{distance to the Matano interface (nm)}$

$$C_{\text{Fe}}(x) := \frac{Cs_{\text{Fe}}}{2} \cdot \left( 1 + \operatorname{erf} \left( \frac{x - d_{\text{Fe}}}{2 \cdot \sqrt{Dt_{\text{Fe}}}} \right) \right)$$

$$C_{\text{C}}(x) := \frac{Cs_{\text{C}} - Co_{\text{C}}}{2} \cdot \left( 1 - \operatorname{erf} \left( \frac{x - d_{\text{C}}}{2 \cdot \sqrt{Dt_{\text{C}}}} \right) \right) + Co_{\text{C}}$$



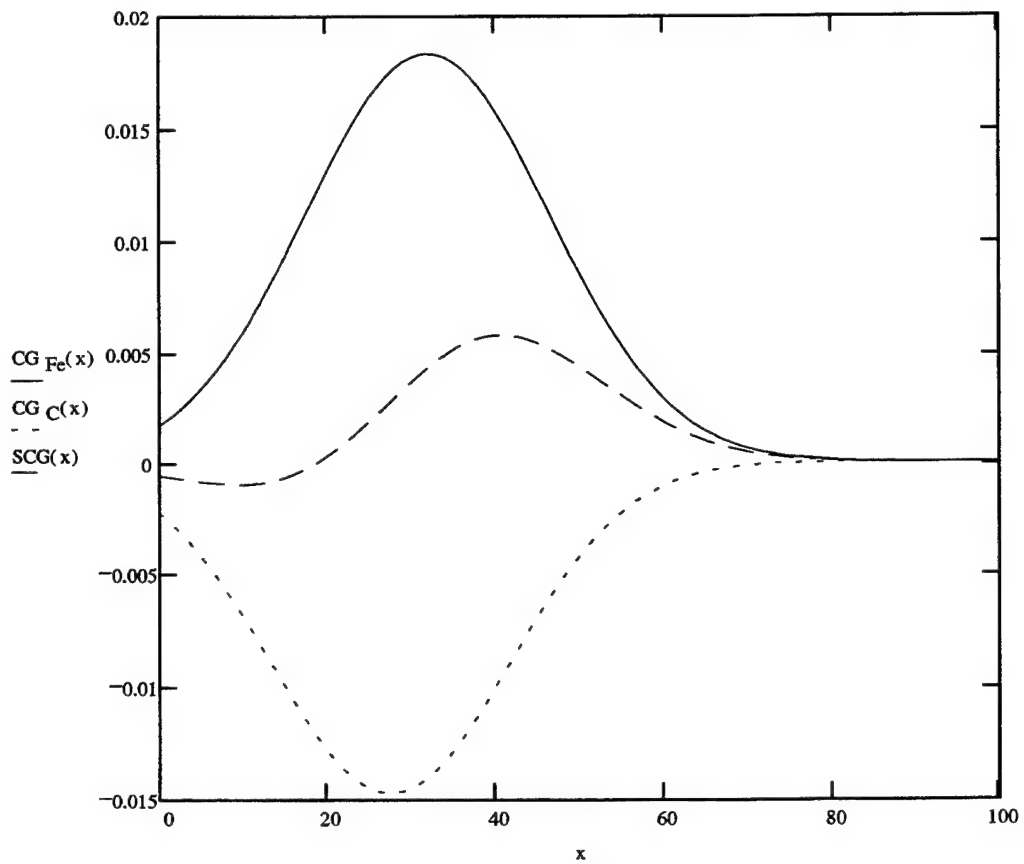


Concentration Gradient;  $CG = dC/dx$  (atomic%/nm)

$$CG_{Fe}(x) := \frac{Cs_{Fe}}{2 \cdot \sqrt{\pi \cdot Dt_{Fe}}} \cdot \exp \left[ -\frac{(x - d_{Fe})^2}{4 \cdot Dt_{Fe}} \right] \quad CG_C(x) := -\frac{(Cs_C - Co_C)}{2 \cdot \sqrt{\pi \cdot Dt_C}} \cdot \exp \left[ -\frac{(x - d_C)^2}{4 \cdot Dt_C} \right]$$

Sum of the Concentration Gradients:  $SGV = CG_{Fe} + CG_C$

$$SCG(x) := CG_{Fe}(x) + CG_C(x)$$



## Botzman-Matano Analyses

The following equation imports the experimental AES data

$A := \text{READPRN}(\text{aes2a})$

$A =$

	0	1	2	3	4	5
0	0	0.9	61.781	18.672	1.968	2.665
1	0.16	4.92	63.653	12.488	2.178	2.753
2	0.66	8.906	61.647	9.993	1.804	3.636
3	1.17	9.789	59.913	9.728	2.256	4.297
4	1.67	10.781	55.237	10.913	2.137	6.92
5	2.18	10.507	50.619	11.673	3.238	9.951
6	2.69	9.947	44.749	12.707	2.782	15.796
7	3.19	8.406	38.939	12.999	3.702	21.944
8	3.7	7.266	32.842	11.982	4.571	29.328
9	4.2	5.736	28.194	11.663	4.393	36.001
10	4.71	4.85	23.77	9.956	4.539	42.87
11	5.21	3.538	19.568	8.072	4.791	50.016
12	5.72	2.313	16.578	6.917	4.273	55.909
13	6.22	1.332	14.28	4.949	5.161	60.265
14	6.73	1.168	12.783	4.463	4.665	62.909

$A(j,0)$  = Sputter time (s)

$A(j,1)$  = At % P

$A(j,2)$  = At % C

$A(j,3)$  = At % O

$A(j,4)$  = At % Cr

$A(j,5)$  = At % Fe

$X := A^{<0>}.8$        $X$  = depth (nm)

$C := \frac{A^{<2>}}{100}$        $C$  = At % of C

$Fe := \frac{A^{<5>}}{100}$        $Fe$  = At % of Fe

$n := 38$        $n$  = number of rows in matrix  $A$  to obtain the concentration at  $x = \infty$

$k := 9$

$k$  = row following the Matano interface.

$m$  = Concentration Gradient;  $\Delta Fe / \Delta x$  at  $x = dFe$

$$m := \frac{(Fe_k - Fe_{k-1})}{X_k - X_{k-1}} \quad m = 0.017$$

The following equation calculates the integrand in the Boltzman-Matano Method using the trapezoid rule for numerical integration. The area of interest is  $C_s^*(X_n - d_{Fe}) - Fe^*(X_n - d_{Fe})$ .

$$I := C_s Fe \cdot \left[ \left[ X_n - (d_{Fe}) \right] \right] - \sum_{j=k}^n \frac{X_j - X_{j-1}}{2} \cdot ((Fe_j + Fe_{j-1})) - \frac{X_k - d_{Fe}}{X_k - X_{k-1}} \cdot \frac{Fe_{k-1} + Fe_k}{2}$$

$$I = 3.587$$

Diffusion term  $Dt$  ( $nm^2$ )

$$Dt_{BFe} := \frac{I}{2 \cdot m}$$

$$Dt_{BFe} = 107.497$$

Which is close to the value obtained by the Marquardt-Levenberg Eq;  $Dt = 106.8$

Comparison if  $m$  and  $I$  were calculated from the Semi-Infinite Solution which should give a value of  $Dt = 106.8$  ( $nm^2$ )

$$m_{SI} := CG_{Fe}(d_{Fe}) \quad m_{SI} = 0.018$$

$$I_{SI} := C_s Fe \cdot (100 - d_{Fe}) - \int_{d_{Fe}}^{100} C_{Fe}(x) dx \quad I_{SI} = 3.906$$

$$Dt_B := \frac{I_{SI}}{2 \cdot m_{SI}}$$

$$Dt_B = 106.8$$

Darken's equations- Kirkendall showed that when one element diffuses faster than another in a diffusion couple the, the apparent boundary between the couple also moves. Based on these principles Darken derived the following equations:

$$v = 1/C \cdot (D_1 \cdot dC_1/dx + D_2 \cdot dC_2/dx) ; \text{ where } v \text{ is the velocity of the Matano interface, } D \text{ is the}$$

the diffusion coeff. of the couple measured experimentally

$$D = C_2/C \cdot D_1 + C_1/C \cdot D_2 \quad D_1 \text{ and } D_2 \text{ are the actual diffusion coeffs of elements 1 \& 2,}$$

$C_1$  and  $C_2$  are the concentration of the elements at the Matano interface,  $C$  is the total molar concentration of elements 1 \& 2.

$$C = C_1 + C_2$$

$$C_T := C_{Fe}(d_{Fe}) + C_C(d_{Fe}) \quad C_T \text{ represents the total molar concentration of Fe and C.}$$

In the present case this is averaged between the concentrations at Matano interface for Fe, defined by  $d_{Fe}$ .

$$d_{Fe} = 32$$

The velocity for the Matano interface,  $v(\text{nm/s})$ :

$$v := .0167$$

Case 1:  $\lim D_C = 0$ . The minimum diffusion coefficient for Fe is obtained in the limit  $D_C = 0$ .

$$k := 0$$

$$D_{Fe} := \frac{v \cdot C_T}{C_{G_{Fe}}(d_{Fe}) + k \cdot C_C(d_{Fe})} \quad D_{Fe} = 0.582 \quad (\text{nm}^2/\text{s})$$

The time  $t$  required to obtain  $D_{Fe}$  in the limit:

$$t := \frac{D_{Fe}}{\frac{D_{Fe}}{C_T} \cdot (C_C(d_{Fe}) + k \cdot C_{Fe}(d_{Fe}))} \quad t = 386.772 \quad (\text{s})$$

Case 2:  $D_C/D_{Fe} = 0.1$

$$k := 0.1$$

$$D_{Fe} := \frac{v \cdot C_T}{CG_{Fe}(d_{Fe}) + k \cdot CG_C(d_{Fe})} \quad D_{Fe} = 0.63 \quad (nm^2/s)$$

The time  $t$  required to obtain  $Dt_{Fe}$ :

$$t := \frac{D_{Fe}}{\frac{D_{Fe}}{C_T} \cdot (C_C(d_{Fe}) + k \cdot C_{Fe}(d_{Fe}))} \quad t = 321.561 \quad (s)$$

Case 3:  $D_C/D_{Fe} = 0.25$

$$k := 0.25$$

$$D_{Fe} := \frac{v \cdot C_T}{CG_{Fe}(d_{Fe}) + k \cdot CG_C(d_{Fe})} \quad D_{Fe} = 0.72 \quad (nm^2/s)$$

The time  $t$  required to obtain  $Dt_{Fe}$ :

$$t := \frac{D_{Fe}}{\frac{D_{Fe}}{C_T} \cdot (C_C(d_{Fe}) + k \cdot C_{Fe}(d_{Fe}))} \quad t = 244.959 \quad (s)$$

Case 4:  $D_c/D_{Fe} = 0.5$

$$k := 0.5$$

$$D_{Fe} := \frac{v \cdot C_T}{CG_{Fe}(d_{Fe}) + k \cdot CG_C(d_{Fe})} \quad D_{Fe} = 0.943 \quad (nm^2/s)$$

The time  $t$  required to obtain  $Dt_{Fe}$ :

$$t := \frac{Dt_{Fe}}{\frac{D_{Fe}}{C_T} \cdot (C_C(d_{Fe}) + k \cdot C_{Fe}(d_{Fe}))} \quad t = 153.697 \quad (s)$$

Case 5:  $D_c/D_{Fe} = 0.75$

$$k := 0.75$$

$$D_{Fe} := \frac{v \cdot C_T}{CG_{Fe}(d_{Fe}) + k \cdot CG_C(d_{Fe})} \quad D_{Fe} = 1.365 \quad (nm^2/s)$$

The time  $t$  required to obtain  $Dt_{Fe}$ :

$$t := \frac{Dt_{Fe}}{\frac{D_{Fe}}{C_T} \cdot (C_C(d_{Fe}) + k \cdot C_{Fe}(d_{Fe}))} \quad t = 90.044 \quad (s)$$

Case 6:  $D_C/D_{Fe} = 0.9$

$$k := 0.9$$

$$D_{Fe} := \frac{v \cdot C_T}{CG_{Fe}(d_{Fe}) + k \cdot CG_C(d_{Fe})} \quad D_{Fe} = 1.869 \quad (nm^2/s)$$

The time  $t$  required to obtain  $Dt_{Fe}$ :

$$t := \frac{D_{Fe}}{C_T} \cdot \frac{Dt_{Fe}}{(C_C(d_{Fe}) + k \cdot C_{Fe}(d_{Fe}))} \quad t = 60.327 \quad (s)$$

Case 7:  $D_C/D_{Fe} = 1.0$

$$k := 1.0$$

$$D_{Fe} := \frac{v \cdot C_T}{CG_{Fe}(d_{Fe}) + k \cdot CG_C(d_{Fe})} \quad D_{Fe} = 2.477 \quad (nm^2/s)$$

The time  $t$  required to obtain  $Dt_{Fe}$ :

$$t := \frac{D_{Fe}}{C_T} \cdot \frac{Dt_{Fe}}{(C_C(d_{Fe}) + k \cdot C_{Fe}(d_{Fe}))} \quad t = 43.119 \quad (s)$$

Case 8:  $D_C/D_{Fe} = 1.30$

$$k := 1.3$$

$$D_{Fe} := \frac{v \cdot C_T}{CG_{Fe}(d_{Fe}) + k \cdot CG_C(d_{Fe})} \quad D_{Fe} = 106.138$$

The time  $t$  required to obtain  $Dt_{Fe}$ :

$$t := \frac{Dt_{Fe}}{\frac{D_{Fe}}{C_T} \cdot (C_C(d_{Fe}) + k \cdot C_{Fe}(d_{Fe}))} \quad t = 0.869$$

Check of Results:

The following calculates  $v$  and  $Dt$  based on values from the last case study.

$$D_C := k \cdot D_{Fe} \quad (nm^2/s)$$

$$CG_{Fe}(d_{Fe}) = 0.018 \quad (at\%)$$

$$CG_C(d_{Fe}) = -0.014 \quad (at\%)$$

$$t = 0.869 \quad (s)$$

$$C_T = 0.637$$

$$D_{Fe} = 106.138 \quad (nm^2/s)$$

$$D_C = 137.979 \quad (nm^2/s)$$

$$v := \frac{1}{C_T} \cdot [D_{Fe} \cdot (CG_{Fe}(d_{Fe})) + D_C \cdot (CG_C(d_{Fe}))]$$

$$v = 0.017$$

$$Dt_{Fe} := \left( \frac{C_C(d_{Fe})}{C_T} \cdot D_{Fe} + \frac{C_{Fe}(d_{Fe})}{C_T} \cdot D_C \right) \cdot t$$

$$Dt_{Fe} = 106.8 \quad (nm^2/s)$$

Which validates the values of the velocity and  $Dt_{Fe}$  used as input variables.



Flux for  $DC/DFe = 0.10$  ;  $t = 321s$ ;  $J_{Fe}$  = flux of Fe atoms;  $J_C$  = flux of C atoms;  $J_V$  = net flux of vacancies excluding the flux of other atoms, i.e., P,O,Cr etc..

$$B(x) := D_{Fe} \cdot CG_{Fe}(x) + D_C \cdot CG_C(x)$$

$$C_T(x) := C_{Fe}(x) + C_C(x)$$

$$J_{Fe}(x) := -D_{Fe} \cdot CG_{Fe}(x) + \frac{C_{Fe}(x)}{C_T(x)} \cdot B(x)$$

$$J_C(x) := -D_C \cdot CG_C(x) + \frac{C_C(x)}{C_T(x)} \cdot B(x)$$

$$J_V(x) := J_{Fe}(x) + J_C(x)$$

